New insights into the modulation of the mitochondrial large-conductance calcium-activated potassium channel: interaction with cytochrome *c* oxidase and carbon monoxide

by Daria Rotko

A thesis submitted for the degree of
Doctor of Philosophy in the discipline of Biological Sciences

Completed in the Laboratory of Intracellular Ion Channels of the Nencki Institute of Experimental Biology, Polish Academy of Sciences,

and in the Division of Neurochemistry, Institute of Experimental Epileptology and Cognition Research, Life & Brain Center, University of Bonn

Supervisors:

Supervisor: Prof. Dr. hab. Adam Szewczyk

Co-supervisor: Prof. Dr. Wolfram S. Kunz

Auxiliary supervisor: Dr. Bogusz Kulawiak

Warsaw, 2022

This study was supported by the European Union's Horizon 2020 research and innovation program under the Marie Skłodowska–Curie grant agreement No. 665735 (Bio4Med).

I would like to express my gratitude to the supervisors Prof. Adam Szewczyk, Prof. Wolfram Kunz, and Dr. Bogusz Kulawiak, for the guidance and support they have offered me at all stages of the preparation of this thesis. Thank you for your dedication, sharing your expert knowledge, and providing numerous opportunities for professional development.

I would also like to thank my colleagues from the Nencki Institute of Experimental Biology and from the University of Bonn for the friendly and collaborative working environment.

I would like to thank my family, my partner and friends for their unwavering support. Особлива подяка моїй мамі за всі твої зусилля та любов.

As I am writing this thesis, my homeland is being attacked by Russia in the unprovoked and atrociously brutal war that already resulted in the deaths of tens of thousands of innocent people and brought insurmountable suffering. I would like to express my deepest gratitude to Ukrainian army for defending everything I hold dear, and to everyone who is helping Ukraine in this fight.

TABLE OF CONTENTS

List of abbreviations 9

1. ABSTRACT 11

2. STRESZCZENIE (ABSTRACT IN POLISH) 12

3. INTRODUCTION 14

3.1. Biophysics of mitochondrial function 14

3.2. Organization of respiratory chain complexes 18

3.2.1. Cytochrome *c* oxidase structure and assembly 22

3.3. Ion channels of the inner mitochondrial membrane 26

3.4. Mitochondrial large-conductance calcium-regulated potassium channels (mitoBK) ... 30

3.4.1. Molecular identity of mitoBK channels 30

3.4.2. Biophysical properties of mitoBK channels 32

3.5. Functional interplay between the mitoBK channels and the respiratory chain 36

3.6. MitoBK channels in mitochondrial signaling 39

3.6.1. Mitochondrial retrograde signaling pathways 39

3.6.2. MitoBK channels in heme and carbon monoxide signaling 42

3.6.3. The role of mitoBK channels in cytoprotective signaling 43

4. AIMS OF THE STUDY 45

5. MATERIALS AND METHODS 47

5.1. Chemicals 47

5.2. Cellular models 49

5.3. Depletion of mtDNA in the astrocytoma cells 49

5.4. Induction of COX8A deficiency in HEK293T cells with CRISPR/Cas9 49

5.5. Nucleic acid isolation 50

5.6. Thermal cycling-based gene expression evaluation 52

5.7. Sanger sequencing 55

5.8. High-throughput whole-transcriptome sequencing 56
5.9. Isolation of mitochondria from cultured cells 56
5.10. Western blot assessment of the amount and composition of proteins and protein complexes 57
5.11. Confocal microscopy cell imaging 60
5.12. Patch-clamp on the ion channels of the inner mitochondrial membrane 61
5.13. Measurement of respiration of astrocytoma cells 62
5.14. Perfusion with CO and confirmation of the CO presence with myoglobin assay 62
5.15. Determination of mitochondrial enzymatic activities 63
5.16. Data analysis 63
6. RESULTS 65
6.1. Molecular identity of mitoBK channels in human astrocytoma and fibroblast cells 65
6.2. Single-channel electrophysiological properties of mitoBK channels in isolated mitochondria of astrocytoma cells 71
6.3. Analysis of interaction of mitoBK channel with the respiratory chain in the model of mtDNA-depleted astrocytoma cells 75
6.3.1. Generation of mtDNA-depleted astrocytoma cell line 75
6.3.1.1. Confocal microscopy imaging of the mitochondrial network of astrocytoma cells upon mtDNA depletion 76
6.3.1.2. Determination of cellular respiration of ddC-treated astrocytoma cells 77
6.3.1.3. Characterization of the expression of the mitochondrial genes in mtDNA depleted line with RNA sequencing 78
6.3.2. Analysis of complexes of mitoBK channels with the respiratory chain proteins in astrocytoma cells 82
6.3.2.1. Assessment of protein complexes of mitoBK channels with the respiratory chain in astrocytoma cells 82
6.3.2.2. Determination of mitoBK protein amount upon mtDNA depletion of astrocytoma cells 85

6.3.2.3. Transcriptome profiling in mtDNA-depleted astrocytoma cells with high-throughput RNA sequencing 87

6.4. Evaluation of the effects of COX8A deficiency on the respiratory chain complexes and mitoBK channels 94

6.4.1. Characterization of the respiratory chain in COX8A-deficient fibroblasts 94

6.4.1.1. Organization of the respiratory chain protein complexes upon COX8A deficiency in fibroblasts 94

6.4.1.2. Evaluation of the protein content of the residual complex IV subunits in COX8A-deficient fibroblasts 96

6.4.1.3. Analysis of the expression of protein subunits of complex IV and other respiratory chain complexes in COX8A-deficient fibroblasts 96

6.4.2. The effects of the induced COX8A deficiency on the respiratory chain in HEK293T cells 98

6.4.2.1. CRISPR/Cas9 induction of COX8A deficiency in HEK293T cells 98

6.4.2.2. The impact of COX8A deficiency on the organization of the respiratory chain complexes in HEK293T cells 100

6.4.2.3. Evaluation of the protein amount of the residual complex IV subunits upon COX8A deficiency in HEK293T cells 101

6.4.2.4. Analysis of the expression of protein subunits of complex IV and other respiratory chain complexes in COX8A-deficient HEK293T cells 102

6.4.3. Estimation of the impact of the COX8A deficiency on mitoBK channels in human fibroblasts 103

6.4.3.1. Assessment of the protein complexes of mitoBK with complex IV 104

6.4.3.2. Evaluation of mitoBK protein amount in fibroblasts with COX8A deficiency 105

6.4.3.3. Analysis of the expression of mitoBK subunits in fibroblasts with COX8A deficiency 106

6.4.3.4. Transcriptome profiling of the COX8A-deficient fibroblasts with high-throughput RNA sequencing 108

6.5. Patch-clamp study of the molecular mechanisms of carbon monoxide modulation of mitoBK channel activity 111

6.5.1. The effects of structurally different CO-releasing molecules on mitoBK channel activity 111

6.5.2. Evaluation of the CO gas modulation of mitoBK activity 115

6.5.3. Analysis of complex regulation of mitoBK channels by heme and CO gas 118

7. DISCUSSION 121

7.1. Signaling pathways activated upon mtDNA depletion in astrocytoma cells 121

7.2. Molecular and functional effects of the loss of cytochrome *c* oxidase subunit 8A 128

7.3. Interaction of the mitoBK channel with the cytochrome *c* oxidase 132

7.4. Mechanisms of modulation of mitoBK channels by the CO and heme signaling 135

8. CONCLUSIONS AND SUMMARY 139

9. LIST OF PUBLICATIONS 141

10. REFERENCES 143

List of abbreviations

ADP	Adenosine diphosphate
ANT	Adenine nucleotide transporter
ATP	Adenosine triphosphate
Bp	Base pair
BK	Large-conductance calcium-activated potassium channel
BN-PAGE	Blue native polyacrylamide gel electrophoresis
Cas	CRISPR-associated protein
cDNA	Complementary deoxyribonucleic acid
cGMP	Cyclic guanosine monophosphate
CO	Carbon monoxide
CORM	CO-releasing molecule
COX	Cytochrome *c* oxidase
CRISPR	Clustered Regularly Interspaced Short Palindromic Repeats
Cryo-EM	Cryogenic electron microscopy
CS	Citrate synthase
ddC	2',3'-dideoxycytidine
DMEM	Dulbecco's modified Eagle's medium
DMSO	Dimethyl sulfoxide
DNA	Deoxyribonucleic acid
eIF2α	Eukaryotic translation initiation factor 2 alpha
ER	Endoplasmatic reticulum
ETC	Electron transport chain
HBD	Heme binding domain
Hsp	Heat shock protein
IMM	Inner mitochondrial membrane
IMS	Intermembrane space
ISR	Integrated stress response
Kv	Voltage-gated potassium channel
MCU	Mitochondrial calcium uniporter

mitoBK	Mitochondrial large-conductance calcium-activated potassium channel
mitoKATP	Mitochondrial ATP-regulated potassium channel
mRNA	Messenger RNA
mtDNA	Mitochondrial deoxyribonucleic acid
MTS	Mitochondrial targeting sequence
mtUPR	Mitochondrial unfolded protein response
NADH	Reduced nicotinamide adenine dinucleotide
Nrf2	Nuclear factor E2-related factor 2
OD	Optical density
OMM	Outer mitochondrial membrane
OXPHOS	Oxidative phosphorylation
PAGE	Polyacrylamide gel electrophoresis
PCR	Polymerase chain reaction
POLG	Polymerase gamma
qRT-PCR	Real-time reverse transcription polymerase chain reaction
RC	Respiratory chain
RCK	Domains regulating calcium conductance
RNA	Ribonucleic acid
ROS	Reactive oxygen species
RT	Room temperature
RT-PCR	Reverse transcription polymerase chain reaction
SDS	Sodium dodecyl sulfate
sgRNA	Single guide RNA
TIM	Translocase of inner membrane
TM	Transmembrane domains
TOM	Translocase of outer membrane
UPR	Unfolded protein response
VDAC	Voltage-dependent anion channel
WT	Wild type

1. ABSTRACT

The defining property of mitochondria – generation of mitochondrial membrane potential – interlinks the metabolic and signaling functions of this organelle. Mitochondrial large-conductance calcium-activated potassium channels (mitoBK) execute its fine regulation by allowing the controlled influx of potassium ions into the mitochondrial matrix. This function endows them with unique properties, resulting in a cytoprotective phenomenon of mitoBK activation in ischemia-reperfusion injury. The functional and structural interaction of mitoBK channels with the electron transfer chain, and in particular, its terminal enzyme cytochrome *c* oxidase (COX), can be one of its molecular mechanisms.

To investigate the interaction between the COX and mitoBK channels, different COX-deficient cellular models were employed. Specifically, human astrocytoma cells were depleted of mitochondrial DNA (mtDNA) by the treatment with 2',3'-dideoxycytidine. The comparison of the protein complexes formed by the mitoBK and COX in the mtDNA-depleted and WT astrocytoma cells identified the interaction of the pore-forming mitoBK subunit with the COX-containing complexes and respirasomes. Furthermore, downregulation of mitoBK-α subunits on both protein and mRNA levels occurred upon mtDNA-induced COX deficiency. The analysis of the retrograde signaling pathways induced by the mtDNA depletion in the mtDNA-depleted astrocytoma cells showed activation of the integrated stress response signaling.

Human dermal fibroblasts with a mutation in the structural COX subunit – COX8A – were used as another cellular model with a deficiency in COX. The organization of the electron transport chain was characterized in the COX8A-deficient fibroblasts and HEK293T cells with CRISPR/Cas9 induced mutations in *COX8A* and ensuing COX deficiency, identifying that the residual COX was stabilized in the respirasomes. The decrease in the protein amount of mitoBK pore-forming subunit, as well as its protein complexes, was observed.

To follow the systemic implications of this coupling, the effect of a gaseous transmitter carbon monoxide (CO), putatively targeting both COX and mitoBK, was assessed in the patch-clamp studies. While direct application of CO-saturated solution has not exerted significant modulation of the mitoBK channel activity, patch perfusion with CO-releasing molecules induced pleiotropic effects. Perfusion with heme and hemin inhibited mitoBK channels. The subsequent application of CO-saturated solution released this inhibition, activating mitoBK channels in the presence of heme.

2. STRESZCZENIE (ABSTRACT IN POLISH)

Podstawowa właściwość mitochondriów – generowanie potencjału w poprzek wewnętrznej błony mitochondrialnej – łączy funkcje metaboliczne i sygnalizacyjne tej organelli. Mitochondrialne kanały potasowe o dużym przewodnictwie aktywowane jonami wapnia (mitoBK) dzięki precyzyjnej regulacji ich aktywności umożliwiają kontrolowany napływ jonów K+ do macierzy mitochondrialnej. Dzięki unikatowym mechanizmom regulacyjnym aktywacja kanału mitoBK indukuje mechanizmy cytoprotekcyjne w uszkodzeniu niedokrwienno-reperfuzyjnym. Funkcjonalne i strukturalne oddziaływanie kanałów mitoBK z łańcuchem transportu elektronów, a w szczególności z jego terminalnym enzymem oksydazą cytochromu *c* (COX), może być elementem mechanizmu cytoprotekcyjnego.

Do zbadania interakcji między kanałami mitoBK oraz COX wykorzystano różne modele komórkowe z obniżonym poziomem tego enzymu. W ludzkich komórkach gwiaździaka indukowano obniżenie liczby kopii mitochondrialnego DNA (mtDNA) przez traktowanie 2',3'-dideoksycytydyną. Porównanie kompleksów białkowych tworzonych przez mitoBK i COX w komórkach gwiaździaka z obniżoną iością mtDNA i w komórkach dzikiego typu wskazało na możliwe oddziaływanie podjednostki tworzącej por kanału z kompleksami i respirasomami zawierającymi COX. Ponadto, w przypadku niedoboru COX indukowanego obniżeniem ilości mtDNA wystąpił spadek poziomu podjednostki α kanału mitoBK. Efekt ten był widoczny zarówno na poziomie białka, jak i mRNA. Analiza szlaków sygnałowych indukowanych przez deplecję mtDNA w komórkach gwiaździaka pozbawionych mtDNA wykazała aktywację zintegrowanej sygnalizacji odpowiedzi na stres.

Ludzkie fibroblasty skórne z mutacją w podjednostce strukturalnej COX – COX8A – zostały wykorzystane jako kolejny model komórkowy z niedoborem COX. W fibroblastach z niedoborem COX8A i komórkach HEK293T z mutacjami wywołanymi CRISPR/Cas9 w genie kodującym COX8A scharakteryzowano organizację mitochondrialnego łańcucha oddechowego. Uzyskane wyniki wskazały, że kompleks IV w uzyskanych mutantach był obecny w respirasomach. Ponadto, zaobserwowano zmniejszenie ilości białka podjednostki tworzącej pory mitoBK oraz jej kompleksów białkowych.

Aby prześledzić ogólnokomórkowe implikacje sprzężenia między łańcuchem oddechowym, w tym COX, a kanałem mitoBK, przeprowadzono doświadczenia elektrofizjologiczne. W badaniach z wykorzystaniem techniki patch-clamp oceniono wpływ gazowego przekaźnika tlenku węgla (CO), przypuszczalnie oddziałującego zarówno z COX, jak i mitoBK. O ile

bezpośrednie zastosowanie roztworu nasyconego CO nie spowodowało znaczącej modulacji aktywności kanałów mitoBK, o tyle zastosowanie związków uwalniających CO wywoływało efekty plejotropowe. Zastosowanie hemu i heminy hamowało aktywność kanałów mitoBK. Wykazano, że zastosowanie roztworu nasyconego CO reaktywowało aktywność kanału zahamowanego cząsteczkami hemu.

3. INTRODUCTION

3.1. Biophysics of mitochondrial function

Mitochondria are organelles of endosymbiotic origin that are present in most eukaryotic cells. One to two billion years ago, a host related to the Asgard group of Archea acquired an α-proteobacterial endosymbiont, what is considered to be the key evolutionary event in the origin of mitochondria [1]. Subsequent consolidation of endosymbiosis has occurred through the integration of metabolic and signaling pathways between an endosymbiont and a host. Yet remarkably, some of the features of this primeval interaction persisted through millennia and can be traced in the modern morphology of mitochondria of its eukaryote clade.

Firstly, despite the incremental transfer of the majority of the genes from an α-proteobacterial endosymbiont to a proto-eukaryotic nucleus during symbiotic integration, modern mitochondria have retained their genome and translation machinery with certain properties characteristic of its α-proteobacterial ancestor. Mitochondrial DNA (mtDNA) in mammalian cells is circular, devoid of introns, and contains 37 genes encoding 22 tRNAs, 2 rRNAs, and 13 subunits of multiprotein oxidative phosphorylation (OXPHOS) complexes. Interestingly, there is a substantial diversity of mitochondrial genome between eukaryotic groups [2], and due to its rapid evolution rate, mitochondrial DNA (mtDNA) is considered to be one of the drivers of evolution [3].

Secondly, mitochondria possess a double membrane-bound structure with four functionally different compartments: the outer mitochondrial membrane (OMM) stemming from an endosymbiont-engulfing envelope, the intermembrane space (IMS), the inner mitochondrial membrane (IMM) originating from an α-proteobacterial membrane, and the mitochondrial matrix enclosed by IMM. In the process of endosymbiotic integration, structures similar to intracytoplasmic membranes of α-proteobacteria have likely evolved into morphologically distinct folds of IMM – the cristae, thus providing an additional level of compartmentalization [4]. Such a peculiar morphology has facilitated the evolution of highly efficient bioenergetic and metabolic OXPHOS processes in mitochondria (Figure 1).

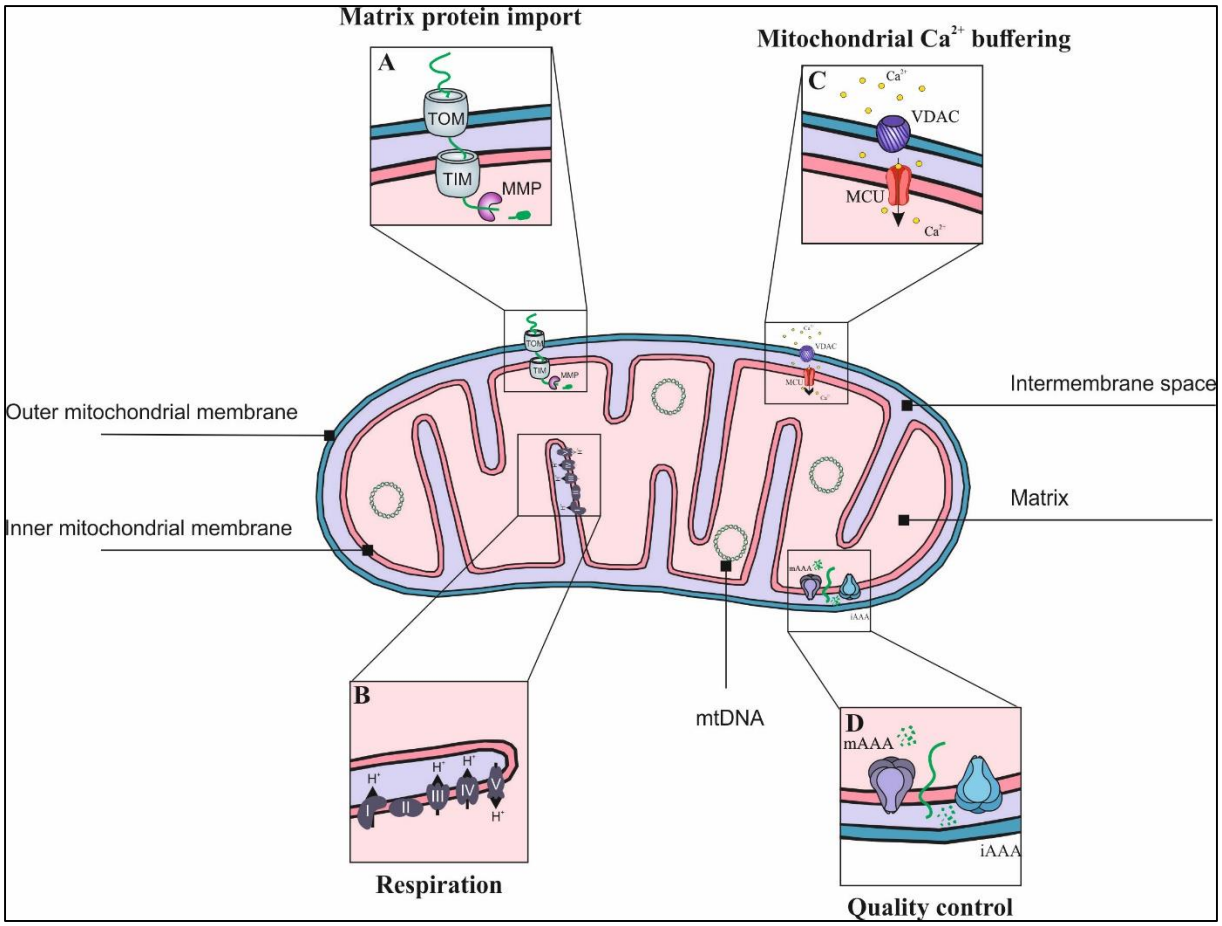

Figure 1. Mitochondrial physiology endows this organelle with various functions. Mitochondria are double-membrane organelles that possess mtDNA and contain four distinct compartments: outer mitochondrial membrane, intermembrane space, inner mitochondrial membrane, and matrix. Numerous processes occurring in mitochondria are associated with this structure, including mitochondrial protein import, respiration, calcium ion buffering, and quality control of mitochondrial proteome.

Russell's concept of the origin of life at alkaline hydrothermal vents dates the evolution of the first electron transport systems at the emergence of complex biological processes [5]. According to this hypothesis, alkaline vents there were, in essence, functioning like bioreactors: providing a compartmentalized surface with a constant supply of molecular hydrogen, carbon dioxide, and clay minerals, thus catalyzing the formation of the first biopolymers four billion years ago. Another peculiarity of the hydrothermal vents was their alkalization compared to the generally acidic environment of CO_2-rich oceans, estimated to differ by up to 4 pH units. Thus, the anticipated proton gradient of the positively charged environment versus the alkaline inner compartment could prompt the evolution of the first electron transport systems.

According to the chemiosmotic Mitchell theory, energy synthesis via OXPHOS requires the initial generation of a gradient of electrochemical potential. Following oxidation of respiratory substrates by the electron transport chain (ETC) complexes I and II harbored in the IMM, the entailed activity of the proton pumps of ETC complexes I, III, and IV generates the electrochemical H^+ gradient across the IMM ($\Delta\mu H^+$). $\Delta\mu H^+$ consists of the electric component, $\Delta\Psi_M$, and the proton concentration gradient, ΔpH:

$$\Delta\mu H^+ = -F\Delta\Psi_M + 2.3\Delta pH$$

where F is the Faraday constant. Mitochondrial $\Delta\mu H^+$ is next dissipated by the movement of protons through ATP-synthase residing across the IMM and is thereby harnessed as the driving force for ATP synthesis by this protein complex. ETC activity generates as byproduct reactive oxygen species (ROS): superoxide ($O_2^{\bullet-}$) and hydrogen peroxide (H_2O_2), which have a signaling role under controlled physiological conditions but are linked to pathology when overproduced [6].

Besides its role in oxidative phosphorylation, maintenance of mitochondrial membrane potential $\Delta\Psi_M$ is crucial for other processes of mitochondrial physiology. Due to the charge separation, the matrix side of IMM is highly negatively charged, and in the physiological conditions, $\Delta\Psi_M$ values are estimated to reach from -140 to -200 mV. Consequently, mitochondrial membrane potential acts as a driving force for the Ca^{2+} and Fe^{2+} uptake by the electrogenic transporters of IMM. Besides a buffering function, changes in Ca^{2+} concentration control mitochondrial substrate oxidation and respiration through regulation of mitochondrial dehydrogenases and complex IV of ETC. The uptake of Fe^{2+} is necessary for the synthesis of iron-sulfur clusters in mitochondria, which are the cofactors of numerous metalloproteins involved in electron transport and catalysis.

In the course of proto-mitochondrial genesis, crucial adaptive events involved the insertion of metabolite transporter proteins into the IMM. The modern mitochondrial carrier family comprising a plethora of solute transporters in the IMM is estimated to originate from a single adenine nucleotide transporter (ANT) [7]. The equimolar exchange of ADP from the cytosol for matrix ATP facilitated by ANT has a net positive (+1) charge and is driven by the $\Delta\Psi_M$.

The development of mitochondrial protein import machinery, which was likely initially allotted to facilitate the insertion of the protein transporters, became another key symbiotic event in mitochondrial evolution. According to the MitoCarta2.0 study, the current mitochondrial proteome in humans and mice is comprised of 1158 proteins, and only 13 of them are encoded

by mtDNA [8]. The rest of the mitochondrial proteins are encoded in the nucleus, and in order to reach the proper mitochondrial compartment, coordinated peptide targeting, recognition and translocation systems are necessary. In certain protein import pathways, the mitochondrial protein targeting by transporter proteins is electrogenic and requires $\Delta\Psi_M$ [9]. Specifically, it has been estimated that up to 70% of mitochondrial proteins possess an N-terminal mitochondrial targeting sequence (MTS) consisting of up to 55 amino acids that form an amphipathic α-helix with a net positive charge (from +3 to +6) [10]. The MTS is recognized by the translocase of outer membrane (TOM) proteins TOM20 and TOM22 and is next transported through the TOM complex. In the proteins destined for IMM, a peptide is thereupon electrophoretically pulled by the MTS through the translocase of inner membrane (TIM) proteins TIM22 or TIM23.

Therefore, the generation of membrane potential may be considered the defining biophysical property of mitochondria, which interlinks their metabolic and signaling functions. In order to maintain $\Delta\Psi_M$, the permeability of IMM to ions is strictly controlled. The plethora of mitochondrial proteins that regulate ion transport through IMM is comprised of mitochondrial metabolite and ion transporters, uncoupling proteins, and mitochondrial ion channels: K^+, Ca^{2+}, Mg^{2+}, and Cl^- channels. By enabling fine control over the mitochondrial $\Delta\Psi_M$, mitochondrial potassium channels act as important regulators of mitochondrial functions.

3.2. Organization of respiratory chain complexes

Oxidative phosphorylation is a metabolic pathway of aerobic generation of ATP that employs five protein complexes (in mammalian cells) embedded in the inner mitochondrial membrane. Four of these protein complexes are involved in the electron transport and are termed the respiratory chain (RC), or electron transport chain (ETC), consisting of:

- complex I (CI) - NADH: ubiquinone oxidoreductase,
- complex II (CII) - succinate: ubiquinone oxidoreductase,
- complex III (CIII) - cytochrome bc_1 complex,
- complex IV (CIV) - cytochrome *c* oxidase,
- two mobile electron carriers - coenzyme Q and cytochrome *c* [11].

The respiratory substrates - NADH or succinate - are supplied to the RC by mitochondrial substrate oxidizing activity, specifically the Krebs cycle. The RC enzymes subsequently catalyze a series of redox reactions that drive the transfer of electrons down the electrochemical gradient from CI or CII through CIII and terminate in the CIV, which reduces molecular oxygen to water. The ensued decline in the redox potentials of the CI, CIII, and CIV promotes the translocation of protons across the IMM. Complex V (CV) – ATP synthase – then harnesses the generated transmembrane proton gradient for chemiosmotic ATP synthesis.

In mammalian cells, OXPHOS is the only metabolic network that is comprised of the proteins encoded jointly by the nuclear and mitochondrial genomes. While the majority of these proteins are the products of the nuclear genome, the few mtDNA-encoded subunits of the electron chain CI, CIII, CIV, and ATP synthase CV are essential to the electron transport and OXPHOS. Since each RC protein complex contains highly redox-active cofactors within their structure, the assembly between the cofactors, nuclear- and mitochondrial-encoded subunits proceeds in a highly controlled manner involving specific assembly factors [12]. Regulation of the ETC biogenesis by the availability of the subunit-encoding transcripts and their products introduces another layer of complexity to this intricate process.

The organization of the OXPHOS complexes in the IMM has been a subject of extensive research. An early “fluid” model postulated that the RC complexes were residing in the IMM independently as separate entities and interacted by random collision evoked by their lateral diffusion in the IMM [13]. However, recent studies of structural and functional characteristics of the ETC have demonstrated that RC complexes can arrange into defined supramolecular

assemblies stabilized by the weak interactions that coexist with the individual complexes. The dynamic nature of the ETC organization is reflected by different stoichiometries of such RC protein supercomplexes: a dimer of complex III interacting with complex IV (III_2 + IV), complex I in association with a dimer of complex III (I + III_2), and a supercomplex termed respirasome that consists of complex I, a dimer of complex III and complex IV (I + III_2 + IV) [14,15]. A respirasome can be considered the minimal discreet entity that possesses the full functionality of ETC.

The molecular architecture of respirasome was solved in the recent cryogenic electron microscopy (cryo-EM) studies [11,16,17] (Figure 2). In mammalian mitochondria, supercomplexes are located on the "flat" sides of cristae, which can be topologically relevant in the events of cristae remodeling [18]. Although the interaction between complexes within the respirasome is nonrestrictive, their close positioning minimizes the distance required for the diffusion of mobile carriers [19]. Notably, the organization of this supramolecular complex is nonrandom: the membrane "leg" of complex I wraps around the dimer of complex III, while complex IV is positioned between them [11,16,17]. Most of the RC subunits involved in the stabilization of the supercomplexes are supernumerary – they are not essential for enzymatic activity and have been a later evolutionary addition to the catalytically active part [17].

While the RC complexes exist in both discrete and respirasome-bound forms, there is no absolute requirement for them to associate into supercomplexes for respiration to proceed [20]. However, the defined stoichiometries of supercomplexes conserved between different species indicate that such supramolecular entities confer certain evolutionary benefits to the ETC organization. Thus, several possible functions of the respiratory supercomplexes have been proposed [20,21].

The close spatial proximity of the ETC complexes might facilitate efficient electron transport. The IMM has one of the highest protein-to-lipid ratios among biological membranes, and the assembly of ETC complexes into higher-order structures could avoid unfavorable protein interactions in this environment [19]. Respirasomes may structurally mitigate ROS synthesis, in particular by complex I since the access of the molecular oxygen to the multiprotein-clad redox-active centers of the complex I would be physically hindered [22]. However, a hypothesis that respirasomes have a potential catalytic advantage through channeling a local pool of ubiquinone between the ETC complexes has been recently refuted by a study demonstrating that its availability to the competing enzymes isn't decreased [21,23].

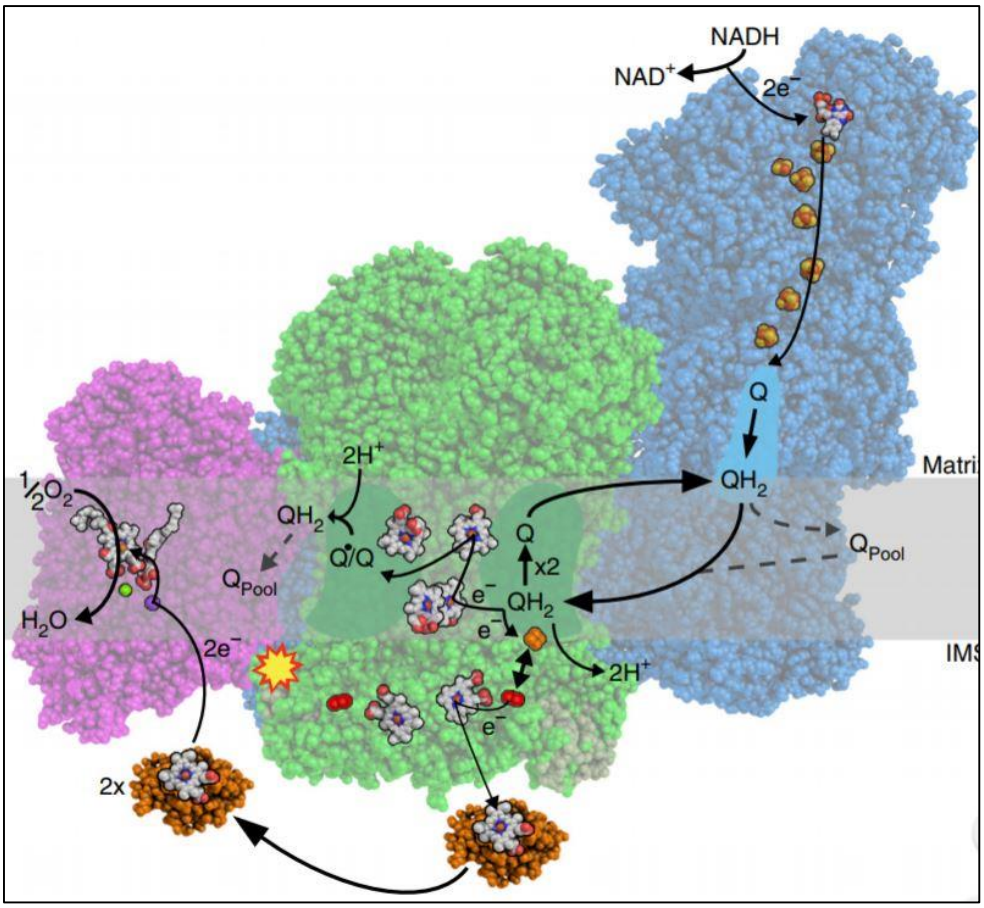

Figure 2. The electron transfer reactions through complexes I, III and IV are shown within the molecular architecture of the mammalian respirasome [24]**.** Following the oxidation of NADH, complex I (protein structure illustrated in blue) catalyzes the reduction of ubiquinone (Q) to ubiquinol (QH_2). QH_2 is then oxidized by complex III (in green), resulting in cytochrome *c* reduction (in orange). The terminal reduction of molecular oxygen to water occurs as a result of two successive cytochrome *c* oxidation reactions catalyzed by complex IV (in pink). Reprinted by permission from Springer Nature: Springer Nature, Nature Structural & Molecular Biology, reference [24], copyright 2017.

A particularly interesting potential role of respirasomes is providing a scaffold for individual RC complexes in the event of RC deficiencies and impaired nuclear-mitochondrial coordination of ETC biogenesis. In the studies of the RC organization with the complex I, III, and IV deficiencies, the architecture of respirasomes was shown to stabilize the individual protein complexes and provide compensatory effects [25–27].

Respirasomes can serve as a physical platform for signaling between complexes since the metabolic and oxidative state of the ETC can be reflected in the dynamic balance and ratio of supercomplexes to discrete RC complexes, as well as their composition. It may provide an

additional layer of physiological feedback on the state of individual complexes, rendering the respirasomes indicators of the ETC functional state.

3.2.1. Cytochrome *c* oxidase structure and assembly

Cytochrome *c* oxidase (COX) is the terminal enzyme (EC 1.9.3.1) of the ETC, which catalyzes the transfer of the electrons from cytochrome *c* to oxygen in the rate-limiting reaction of ETC – the reduction of molecular oxygen to water:

$$O_2 + 4e^- + 4H^+ \rightarrow 2H_2O$$

Oxidation of one O_2 molecule requires 4 sequential events of binding the electron donor – reduced cytochrome *c* – to COX. This reaction is also coupled to the transfer of protons contributing to the generation of a mitochondrial electrochemical gradient. During one cycle of activity of COX, eight protons are translocated from the matrix: four of them are used in the reduction reaction, and the remaining four are pumped out into the IMS.

In mammalian cells, the holoenzyme of COX is comprised of an apoenzyme containing 14 protein subunits and prosthetic groups involved in the redox center formation: two heme groups – heme *a* and heme a_3, and two copper ions – Cu_A and Cu_B. While heme *a* is fully ligated to four histidine residues, heme a_3 has one spare coordination position that can bind molecular oxygen or COX inhibitors such as carbon monoxide (CO), cyanide, and azide.

The catalytic core of COX is formed by the three highly hydrophobic transmembrane subunits that are encoded by the mitochondrial DNA: COX1 and COX2, which incorporate prosthetic groups, and COX3. A cytochrome *c* - docking pocket is located on the N-side of COX2 in proximity to the two copper ions of the Cu_A center. The electrons from cytochrome *c* are initially accepted by the Cu_A center and are transferred to the heme *a* bound to COX1. After the subsequent transfer of electrons to the binuclear Cu_B - heme a_3 center containing a bound and split O_2 molecule, the reduction of oxygen to water occurs. Interestingly, while COX directly interacts with molecular oxygen, it generates a relatively low amount of ROS: a fully functional COX is estimated to produce superoxide anion ($O_2^{\bullet -}$) in a mono-electronic reaction out of only 1-3% of oxygen [28].

The remaining eleven protein subunits of COX are encoded by the nuclear genome: COX4, COX5A, COX5B, COX6A, COX6B, COX6C, COX7A, COX7B, COX7C, COX8A, NDUFA4 (also known as COXFA4). The nuclear-encoded subunits do not directly participate in the catalytic reaction but are instead involved in the assembly, stabilization and regulation of COX.

Biogenesis of COX is a highly controlled process, which is regulated by more than thirty nuclear-encoded assembly factors that are involved in the membrane insertion of the proteins,

synthesis and delivery of prosthetic groups and cofactors [29]. The initial linear model of COX assembly postulated it as a stepwise process of incorporation of the individual protein subunits into the assembly intermediates [30]. However, an updated modular model was proposed recently, which described COX assembly as a modular process [31]. According to this model, the initial protein seed is formed around subunits COX4 and COX5A with an assembly factor HIGD1A, which is then joined by COX1 with accompanying chaperones forming the first COX module. Two additional protein modules assemble around the remaining catalytic core COX subunits, each containing supernumerary subunits with a set of assembly factors: a COX2 module containing subunits COX5B, COX6C, COX7B, COX7C, COX8, and a COX3 module containing subunits COX6A, COX6B, COX7A, with NDUFA4 being added last [32] (Figure 3).

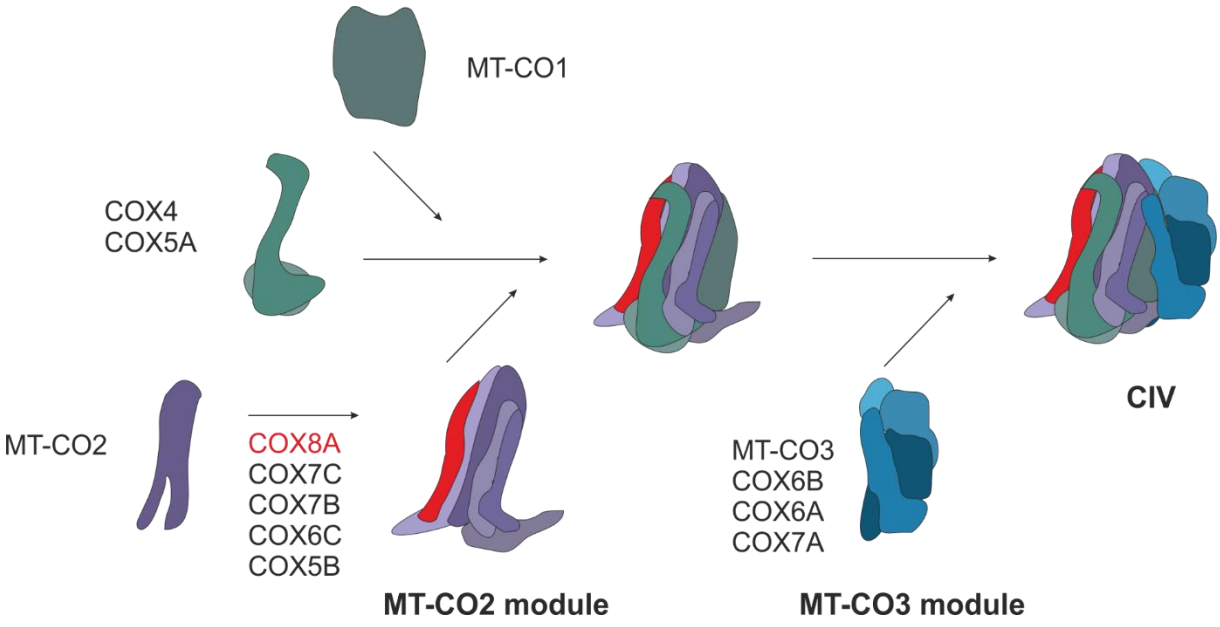

Figure 3. A schematic illustration of the assembly of COX structural subunits according to the modular assembly model. COX1 (MT-CO1) joins the protein seed formed by subunits COX4 and COX5A. Two other COX assembly modules are formed around the remaining catalytic core subunits: COX2 (MT-CO2) module and COX3 (MT-CO3) module. The schematic depiction of the COX subunits is based on the structural data deposited in the Protein Data Bank under entry 5Z62, as reported by Zong et al. (2018) [33].

COX can exist in two forms in the IMM as a functional enzyme: either discretely as a singular CIV or its homodimer (CIV_2), or as a part of the supercomplex with the dimer of complex III ($CIII_2$-CIV) or a respirasome containing complex I, complex III dimer and complex IV (CI-

$CIII_2$-CIV) [34]. The structural data obtained with cryo-EM show that COX is incorporated into the supercomplexes as a monomer [35]. However, whether COX is incorporated into the supercomplexes as a fully assembled enzyme or at its subassemblies stages is still an open question, with different studies supporting both pathways [29]. Certain supernumerary COX subunits are involved in the formation of the supercomplexes. Specifically, subunits COX8 and COX7C are directly interacting with complex I in the respirasomes. The subunit COX7A interacts with complex III subunits, and the subunit COX6A1 is also implicated in the stabilization of COX within this supercomplex [36]. An isoform of COX7A - COX7A2L, containing both complex I and complex III contact sites, has a key role in the stabilization of respirasomes.

Regulation of COX activity is a complex process that occurs on different levels. Firstly, a number of supernumerary subunits are expressed in a tissue-specific manner to optimize electron transfer in response to the different metabolic and environmental conditions [37]. Secondly, the expression of COX4 isoforms COX4-1 and COX4-2 is regulated by oxygen availability under transcriptional control through a hypoxia inducing factor 1 (HIF-1) [38]. Moreover, COX can modulate the activity of other ETC complexes in a respirasome under hypoxia: a transcriptional induction of NDUFA4L2 – a hypoxia-induced isoform of NDUFA4 – by HIF-1 decreased the activities of both complexes I and IV by a molecular mechanism that remains to be elucidated [39]. Thirdly, allosteric regulation of COX by the change in the ADP/ATP ratio controls a crucial step in the electron transfer activity: the binding affinity of cytochrome *c* to COX2 is decreased following the binding of ATP to the matrix-exposed domains of the COX [40]. Fourthly, various types of post-translational modifications of COX that exhibit a modulatory effect on its activity have been reported, including phosphorylation, methylation, acetylation, nitrosylation, and sulfoxidation [41].

While impairments in the mtDNA maintenance machinery can negatively affect OXPHOS, COX deficiencies sensu stricto caused by the defects in assembly and/or function of COX are classified as a distinct class of mitochondrial disorders. Genetic conditions of different severity leading to COX deficiencies have been reported, including mutations in COX assembly factors and structural subunits of mitochondrial as well as nuclear origin [35]. Moreover, patients with mutations in mtDNA-encoded subunits may have mitochondrial heteroplasmy in different tissues, which further complicates the clinical picture. Due to such heterogeneity, COX deficiency can have different clinical manifestations and lethality, although certain biochemical and physiological patterns are commonly observed. These may include myopathy and acidosis

in skeletal and cardiac muscle tissue, neurological disorders of the central nervous system such as Leigh syndrome, and multi-system disorders such as French-Canadian type Leigh syndrome, which affects the brain, skeletal muscle and liver [42–44].

3.3. Ion channels of the inner mitochondrial membrane

Due to the essential role of the mitochondrial membrane potential in mitochondrial function, tight regulation of ion permeability of the IMM is required for the maintenance of bioenergetics and mitochondrial signaling. Under physiological conditions, modulation of mitochondrial membrane potential is largely performed by six ions that cross the IMM: H^+, K^+, Ca^{2+}, Cl^-, Na^+, and Mg^{2+}. Ion fluxes are dependent on the mitochondrial membrane potential and gradients across the IMM, which are vastly different for each ion species (Table 1). Considering the scope of this work, the focus of this chapter will be limited to mitochondrial potassium ion homeostasis. For the discussion on the remaining ion fluxes in mitochondria, the reader can be directed to a comprehensive review [45].

Table 1. Concentrations of selected inorganic ions in different cellular compartments [46–48].

	Extracellular	Cytosolic	Matrix
K^+	4 mM	150 mM	150-180 mM
Ca^{2+}	1 – 2 mM	10^{-7} – 10^{-6} M	10^{-7} – 10^{-4} M
Na^+	140 mM	8 mM	6 mM

The OMM is highly permeant to K^+ due to a high density of voltage-dependent anion channels (VDAC) containing an approximately 1 nm large pore that can conduct both anions and cations within its β-barrel structure [49]. While the primary function of TOM40 is to facilitate mitochondrial peptide transport, its transmembrane pore has ion-conductive properties as well [50]. However, in the IMM the K^+ permeability is tightly regulated. The report on the activity of ATP-regulated K^+ channels in the IMM (mitoK_{ATP}) in 1991 was a pioneering work that has led to a burst of research in the field of the mitochondrial potassium channels [51]. Thirty years later, K^+ channels are recognized as the largest group of ion channels in mitochondria, with eight types of mitochondrial K^+ channels having been identified to date. It is important to consider that the K^+ channel density in the IMM is estimated to be low, and since their expression is tissue-specific, only certain mitochondrial potassium channel types are present in a mitochondrion of a given cell type.

The influx of potassium ions into the mitochondrial matrix after an opening of the K^+ channels follows the electrochemical K^+ gradient across the IMM. The 150 mM concentration of K^+ in

the mitochondrial matrix is close to the equilibrium with the K^+ concentration in cytosol and IMS. The K^+ traffic inside the matrix is driven primarily by the strong electric component of the electrochemical gradient – the negative mitochondrial membrane potential $\Delta\Psi_M$= -180 mV (on average), what sets mitochondrial K^+ channels apart from their plasma membrane counterparts. The influx of K^+ is accompanied by the entry of osmotically obligated water through aquaporins causing mitochondrial swelling. To maintain the potassium ion equilibrium, accumulated K^+ is then extruded from the matrix by the activity of the K^+/H^+ antiporter, which leads to H^+ reentry into the matrix and a decrease in mitochondrial volume. This process is termed a futile potassium cycle [52].

Unlike the plasma membrane channels, the opening of potassium channels in the IMM results in mild mitochondrial depolarization. Thus, activation of a large-conductance calcium-activated potassium channel that has the highest conductance among the mitochondrial K^+ channels – approximately 300 pS – is estimated to decrease the $\Delta\Psi_M$ by about 3 mV [53]. The potassium entry inside the mitochondrial matrix stimulates the activity of ETC, increasing proton pumping and respiration, and regulates matrix volume and generation of ROS [54,55].

Mitochondrial potassium channels are frequently referred to as the "mirror image" of the plasma membrane potassium channels since many of them are encoded by the same genes. The residence of the K^+ channels in the unique mitochondrial proteomic, lipid and signaling milieu, on the other hand, endows them with a special role in the mitochondrial signaling networks. Yet despite advances in the research field, the molecular identity of most mitochondrial channel isoforms remains unknown, and structural data are instead inferred from their plasma membrane counterparts with similar patterns of activity and responses to the channel modulators.

While K^+ channels are a structurally diverse protein family, they share a high degree of conservation in the transmembrane pore region, which is thought to have originated from a common evolutionary ancestor of both eukaryotic and prokaryotic K^+ channels, possibly of viral origin [56,57]. This structural module consists of two transmembrane domains (TM) and an α-helix containing the signature amino acid sequence of K^+ selectivity filter – TVGYG [58]. Gene duplication and fusions have resulted in greater diversity in the composition of mitochondrial and plasma membrane K^+ channels, as well as additional molecular mechanisms controlling their opening [56].

The voltage-gated group of mitochondrial potassium channels includes mitoKv1.3 of the Shaker family, mitoKv1.5 and mitoKv7.4 channels [59]. The functional form of the mitoKv

channels, based on the similarity of their recorded activity to the plasma membrane voltage-gated channels, is likely a tetramer of 6-TM subunits. Each of them contains a 4-TM voltage-sensing domain (VSD) with a positively charged S4 helix, which is attached to a core 2-TM pore domain. Membrane depolarization increases the activity of mitoKv channels.

MitoKv1.3 channels were identified in the IMM of neurons, macrophages, lymphocytes, and several cancer cell lines: Colo357 pancreatic ductal adenocarcinoma cells, PC-3 prostate cancer cells, B16F10 melanoma cells [60]. Pharmacological modulation of mitoKv1.3 has been investigated in the context of prospective antitumor therapy [61]. MitoKv1.3 channels are implicated in apoptotic pathway regulation, as the pro-apoptotic factor Bax interacts with mitoKv1.3 and inhibits these channels. Heterotetrameres consisting of mitoKv1.5 and mitoKv1.3 can be formed in the macrophages, where they are linked to the apoptotic signaling as well [62]. MitoKv7.4 channels were identified in the mitochondria of rat cardiac and neuronal cells, and their activation was shown to be cytoprotective in the ischemic heart injury [63].

Three types of mitochondrial K^+ channels are modulated by calcium ions, transducing signals about the changes in mitochondrial Ca^{2+} concentration to the $\Delta\Psi_M$: large-conductance K^+ channel, mitoBK, intermediate-conductance K^+ channel, mitoIK, and small-conductance K^+ channel, mitoSK. To provide an accurate feedback signal, Ca^{2+} activation thresholds and K^+ conductance values differ between these channels.

MitoBK channel is jointly regulated by the IMM voltage and Ca^{2+} binding. A minimal functional mitoBK channel consists of a tetramer of 7-TM pore-forming subunits, and the Ca^{2+} sensitivity of mitoBK is conferred by the Ca^{2+}-binding domains within a C-terminal region of their pore subunits. Unlike mitoBK, mitoIK and mitoSK are not voltage-gated, and their Ca^{2+} sensitivity is conferred by calmodulin associated with the calmodulin-binding domain at the C-terminus of their 6-TM subunits.

Two-pore-domain K^+ channels structurally form a dimer of subunits with a duplicated core 2-TM pore region. A mitochondrial form of the TWIK-Related Acid-Sensitive K^+ Channel 3 (mitoTASK-3) was identified in HaCaT keratinocytes and melanoma cells. MitoTASK-3 activity is controlled by the changes in pH, as it shifts from being active at pH 7.4 to inhibition upon acidification.

The identity of the mitoK_{ATP} channel has been disputed. While a body of research focused on the mitochondrial isoform of inward-rectifying of Kir1.1b as a potential candidate, a recent report linked mitoK_{ATP} to a 2-TM coiled-coil domain-containing protein 51C (CDC51) protein

[64], which is yet to be fully characterized. A model assuming the tetrameric organization of mitoK$_{ATP}$ containing a tetramer of pore-forming CCDC51 subunits, each associating with an ATP-binding subunit, has been proposed. Interestingly, another study has recently demonstrated that the ATP synthase complex can function as a K^+-conductive entity with same biophysical and pharmacological properties as mitoK$_{ATP}$ channels, thus proposing it as a new contender for its molecular identity [65].

The evidence of mitochondrial localization was reported for the sodium-activated potassium mitoK$_{Na}$1.2 in cardiomyocytes [66]. These channels are heterotetramers of pore-forming subunits containing 7-TM domains, an ATP-binding cassette, and a Na^+-binding region in the C-terminal part. The physiological significance of the Na^+ and Cl^--regulated activation of the mitoK$_{Na}$1.2 channels remains unknown. However, these channels are implicated in the modulation of mitochondrial metabolism, and their activation by volatile anesthetics confers cardioprotection in the ischemia-reperfusion injury.

3.4. Mitochondrial large-conductance calcium-regulated potassium channels (mitoBK)

3.4.1. Molecular identity of mitoBK channels

The functional mitoBK channel is formed by a tetramer of the pore-forming BK-α subunits, which can associate with the regulatory BK-β subunits. The α subunit of mitochondrial and plasma membrane BK channels is encoded by the *KCNMA1* gene. Interestingly, *KCNMA1* is rather conserved among eukaryotic species - a Clustal Omega alignment of the canonical amino acid sequences indexed for mammalian (human, mouse, rat, rhesus macaque, dog, pig), avian (chicken) and amphibian (African clawed frog) species displays ~74% amino acid similarity. In mammals, *KCNMA1* is widely expressed in both excitable and non-excitable cells. The presence of the mitoBK channel in particular was reported in mammalian endothelium [67], brain [68], heart [69], skeletal muscle [70], and fibroblasts [71]. Mitochondrial BK channel orthologues were also identified in potatoes [72] and a protozoon amoeboid [73].

According to the database GTEx (release V8), in human cells, *KCNMA1* is located on chromosome 10 in region 10q22.3 and contains 57 exons. Therefore, alternative splicing of *KCNMA1* transcripts is the major source of structural variability of the BK channels. As a case in point, 94 transcripts of the human *KCNMA1* were listed in the Ensembl database (release 106), and 66 of them were indexed as protein-forming. However, the high-resolution proteomic studies typically detect only the small peptide fraction of all determined alternative splice variants. Thus, whether all splice variants have functional significance or are translated at all is a matter of discussion [74]. In addition, hundreds of single nucleotide polymorphisms in the human BK-α subunit were reported, further contributing to the genetic heterogeneity of BK channels [75].

A splice variant of the BK-α subunit named VEDEC after the final amino acids of its distinct C-terminal 50 amino acid signature is sometimes suggested to be a mitochondria-specific isoform of BK channels. This observation holds true for the mitoBK channels of mice cardiomyocytes, where VEDEC was shown to be exclusively targeted to the mitochondria [76]. In HEK293T cells that were heterologously expressing a VEDEC isoform, the presence of BK channels was observed in mitochondria and endoplasmic reticulum [77]. On the contrary, a VEDEC isoform was specifically localized to the endoplasmic reticulum in COS7 cells [78]. Interestingly, another study did not detect the presence of VEDEC isoforms in human

astrocytoma cells with confirmed mitoBK channel activity [79]. In the N2a neurons, the VEDEC isoform of BK-α subunits was processed through the endoplasmic reticulum, and the *S*-acylation status of the partner BK-β4 subunit determined whether the VEDEC isoform was retained in the ER or was trafficked to the cell membrane surface [80].

The databases GTEx (release V8) and Ensembl (release 104) show that the canonical splice variant SAKCA of *KCNMA1* in human cells is composed of 28 exons and incorporates an exon #55 of *KCNMA1* as last at its 3'-terminus (Figure 4). Alternatively, the *KCNMA1* transcripts ending with an exon #57 produce splice variants VYR, VEDEC, or peptides containing a premature stop codon and subjected to nonsense-mediated decay. The databases GTEx (release V8) and Ensembl (release 104) listed 39 *KCNMA1* transcripts containing the exon #57. Mapping of these transcript models to the corresponding amino acid sequences obtained from the UNIPROT database (release 2022_01) identified 16 transcripts producing isoforms with a VEDEC terminal signature that differed in their exon composition and had a varying length of the encoded 3'-UTR. Therefore, the VEDEC isoform should be regarded as a group of transcripts with similarities in the C-terminus, and their structural heterogeneity may account for the reported different observations. By and large, while in certain cell types VEDEC is localized to mitochondria as mitoBK, a sole presence of this terminal amino acid signature within the BK-α subunit might be not sufficient for universal mitochondrial targeting, and other molecular mechanisms may be involved. Indeed, the codon bias introduced by the synonymous codons encoding the alternative splicing products with similar amino acid sequences was shown to direct the sorting of the potassium channels either to mitochondria or the secretory pathway[81].

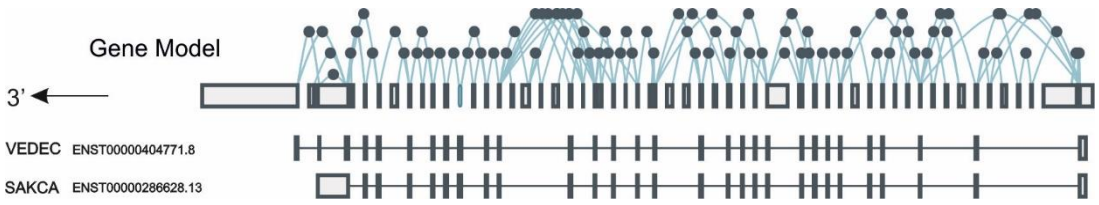

Figure 4. A gene model based of *KCNMA1* and exon expression in two transcripts: a canonical SAKCA isoform and one of the VEDEC isoforms. Considering that *KCNMA1* is located on the minus strand, the orientation of the gene model is indicated as 3' ← 5'. In the gene model, rectangular boxes or vertical lines depict all *KCNMA1* exons, and round dots depict exon-exon junctions. In the transcript models, only the *KCNMA1* exons comprising the spliced transcripts are shown. The data used for the construction of the gene and transcripts models shown above were obtained from the GTEx Portal (release V8).

There are indications that mitoBK-α follows a typical mitochondrial import pathway mediated by the TOM and TIM complexes, and it is likely translated in the cytosol before the protein import into mitochondria. Namely, in a proteomic screening of heterologously expressed mitoBK in HEK293T cells, the interaction of mitoBK channels with the components of TOM complex was shown: the receptor subunit TOM22 binding the peptides to be translocated, TOM70 recognizing and translocating peptides, and TOM40 forming a protein conductive pore [82]. The association of the mitoBK-α subunit with TOM22 did not require the presence of the C-terminal VEDEC amino acid signature, and a co-immunoprecipitation study indicated that mitoBK-α subunit interacted with TOM22 via its transmembrane domain. Components of the TIM complex for the import into the IMM, such as TIM23 and TIM16, were also identified in the mitoBK-α protein interactome.

3.4.2. Biophysical properties of mitoBK channels

While the structural information on mitoBK channels is not yet available on the atomistic level, high-resolution X-ray and cryo-EM structures of the BK-α subunit associated with the BK-β4 subunit were solved for the plasma membrane BK channels [83–85]. The key structural elements of mitoBK channels can be inferred from the data on their plasma membrane counterpart.

MitoBK channel has the largest conductance of all described mitochondrial channels. The unitary conductance for the mitoBK channel in mammalian cells, as recorded with patch-clamp in a symmetric 150/150 mM KCl solution containing 100 μM Ca^{2+}, ranges from 190 pS in mouse cardiac myocytes to 295 pS in a human glioma cell line (LN229) [86].

The conductive pore of BK channels is formed by a tetramer of BK-α subunits. Each of the BK-α subunits is composed of approximately 1200 amino acids and contains seven TM helices, six of which – S1-S6 – are conserved between the voltage-gated potassium channel family, and a remaining α-helix S0 is unique for BK channels (Figure 5). The 7-TM channel topology requires an opposite orientation of the N- and C-termini: the functional studies of mitoBK channel activity indicate that the N-terminal part of the channels is exposed to the IMS, while the C-terminal part is oriented towards the mitochondrial matrix.

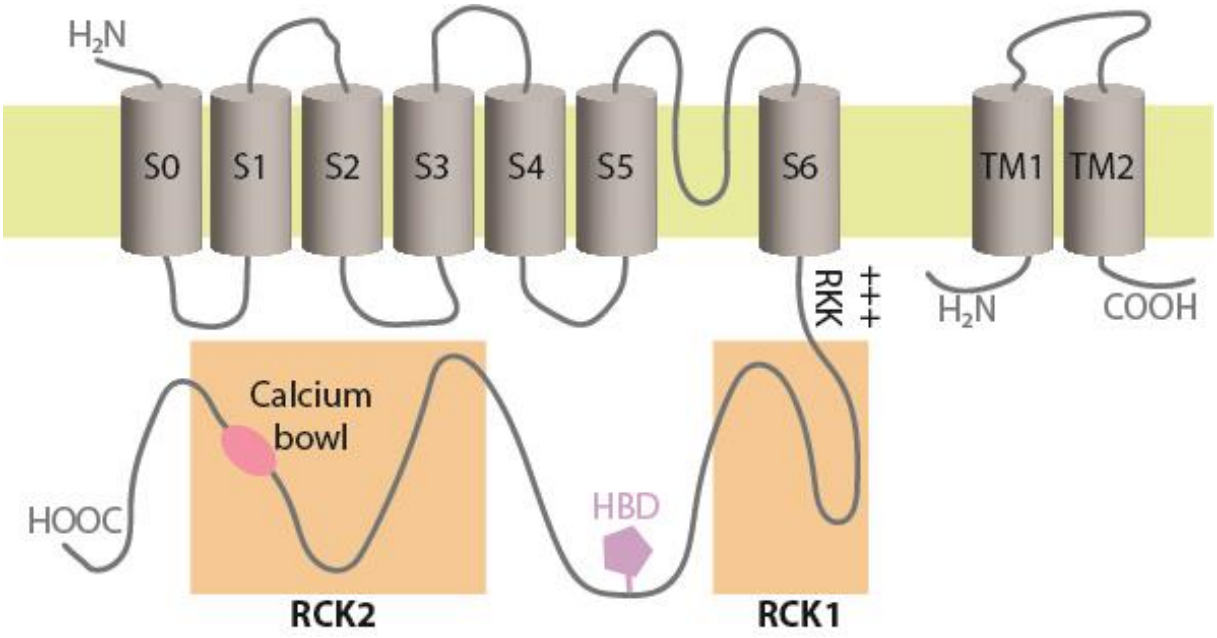

Figure 5. A schematic illustration of key structural elements of BK-α subunit (left) and BK-β subunits (right). BK-α subunits contain seven TM helices, with the TM helices S5 and S6 forming the channel pore. The C-terminal tail of the BK-α subunits contains several functional domains, including RCK1, RCK2, and heme-binding domain (HBD). The BK-β subunits contain two TM helices.

The channel pore is formed by the TM helices S5-S6 that resemble the core 2-TM pore region for K^+ channels containing the signature amino acid sequence of K^+ selectivity filter: TVGYG. The pore-forming domain is physically liked to a voltage-sensing domain (VSD) of BK channels, which is similar to the one found in K_v channels and is formed by four TM helices S1-S4 [87]. The regularly interspaced arginine residues within the VSD have a crucial role in voltage sensing, leading to conformational changes that activate BK channels at membrane depolarization [88]. Notably, while the opening of the plasma membrane BK channels contributes to the membrane repolarization, an influx of K^+ through mitoBK inside the matrix would further depolarize the IMM and, accordingly, lead to an increase of mitoBK current density.

While the C-terminal region of the BK-α subunit is its largest and the most structurally diverse part, it contains several functional domains that are conserved among most subunit isoforms. The two domains regulating calcium conductance 1 and 2 (RCK1, RCK2) of each of the four BK-α subunits associate into an octameric BK gating ring. Ca^{2+} binds to BK-α subunit in two sites: to a high-affinity calcium bowl formed by RCK2, and a site within RCK1 [88]. The conformational change in this region is transferred to the pore-gating domain directly through a C-linker region consisting of the 15 amino acids, and indirectly through non-covalent

interactions. The binding of Ca^{2+} to BK-α subunits increases the open probability of BK channels as a function of Ca^{2+} concentration [89].

Since the regulatory elements of the BK channels that confer its voltage and Ca^{2+}-sensitivity are located within different structural domains, activation of BK channels by Ca^{2+} can proceed independently without changes in the membrane potential values and vice versa. However, BK channel activation with a small probability occurs as an intrinsic event without Ca^{2+} binding or perturbation of the VSD, indicating that activation of these sensors is not strictly required for the channel pore opening [90].

A BK-α subunit can interact with one of the auxiliary β-subunits of four types – BK-β1, BK-β2, BK-β3, and BK-β4. Multiple domains of BK-α and BK-β subunits are involved in the assembly of the channel complex, including the transmembrane region and gating domain of BK-α, and intracellular regions as well as an extracellular linker of BK-β subunits [91]. The expression of BK-β subunits is tissue-specific [92]. Incorporation of BK-β subunits into the channel complex can impact mitoBK gating behavior, Ca^{2+} and voltage sensitivity, channel activation and deactivation kinetics, induce channel inactivation, or affect the modulation of the channel by endogenous and pharmacological compounds (Table 2).

In a set of tissues, BK channel complexes include auxiliary leucine-rich repeat containing (LRRC) BK-γ subunits [93,94]. The binding of regulatory subunits to the pore-forming complex occurs in a competitive manner: only one auxiliary subunit – BK-β or BK-γ –can associate with a single BK-α subunit. However, all identified BK-γ subunits belong to the extracellular superfamily of LRRC proteins and possess a cleavable N-terminal signal peptide that targets them by the secretory pathway to the plasma membrane [94]. Therefore, it appears unlikely that mitoBK channels contain auxiliary BK-γ subunits.

Table 2. Tissue expression and biophysical roles of auxiliary BK channel subunits (modified from [92–94])

Subunit	Gene	Tissue expression	Biophysical role
β1	*KCNMB1*	Smooth muscle, lungs, brain, kidneys.	Increases Ca^{2+} and voltage sensitivity. Slows down activation and deactivation kinetics. Confers channel modulation by 17-beta-estradiol .

β2	*KCNMB2*	Cardiovascular system, lungs, brain, testes, pancreas, adrenal glands.	Modulates Ca^{2+} sensitivity. Negative regulator that confers rapid channel inactivation.
β3	*KCNMB3*	Kidneys, pancreas, spleen, liver, lungs, brain.	Isoforms 2, 3 and 4 inactivate the channel current.
β4	*KCNMB4*	Central nervous system, kindeys.	Slows down activation kinetics. Decreases Ca^{2+} sensitivity. Shifts voltage activation to more negative potential values. Abolishes channel inhibition by charybdotoxin.
γ1	*LRRC26*	Trachea, prostate, thyroid gland, thymus, salivary gland, colon, aorta.	Large negative shift in voltage dependence of channel activation. Accelerates activation kinetics.
γ2	*LRRC52*	Testes, skeletal muscle, kidneys, placenta.	Shifts voltage dependence of channel activation to more negative values at increased Ca^{2+} concentration. Accelerates activation kinetics.
γ3	*LRRC55*	Brain, kidneys, liver, spleen, colon, testes.	Shifts the voltage dependence of BK channel activation to more negative values.
γ4	*LRRC38*	Brain, testes, skeletal muscle, spleen, thymus, adrenal gland.	Small negative shift in voltage dependence of channel activation.

Modulatory effects on mitoBK channels by the BK channel openers and blockers are well-characterized on a single-channel level. In particular, activation of mitoBK channels was shown following the application of benzimidazole derivatives such as NS1619 and NS004, and carboxylic indole derivatives such as CGS7184 [95,96]. The peptides of scorpion venoms charybdotoxin and iberiotoxin, as well as an indole derivative alkaloid paxilline, were found to inhibit mitoBK channel activity [96].

3.5. Functional interplay between the mitoBK channels and the respiratory chain

Mitochondrial ion fluxes and maintenance of mitochondrial ion gradients are essential for mitochondrial physiology. From the biophysical point of view, the respiratory chain complexes and mitoBK channels execute opposite regulation of the mitochondrial membrane potential: the activity of ETC generates it, while mitoBK opening dissipates it (Figure 6).

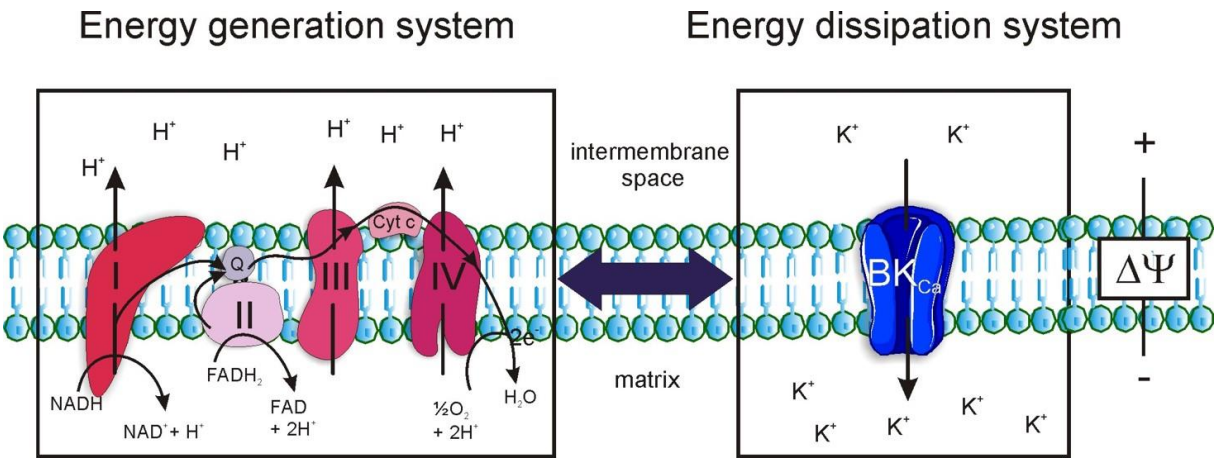

Figure 6. A schematic depiction of opposite regulation of mitochondrial membrane potential by the ETC and mitoBK channels. The activity of the ETC (left box) generates mitochondrial membrane potential, and the activity of mitoBK channels (right box) directly dissipates $\Delta\Psi_M$.

The key physiological functions of the mitoBK channels are mediated through their influence on the activity of ETC via the following molecular mechanisms that will be briefly reviewed below:

- change in the protonmotive force;
- modulation of ROS synthesis by the RC;
- Ca^{2+}-dependent regulation of ETC function;
- control over the local availability of substrates.

The activity of mitoBK channels controls protonmotive force in both direct and delayed manners. The influx of K^+ through mitoBK exerts mild depolarization and changes the electrical component of the driving force for ETC. A chemical gradient component of the protonmotive

force is regulated indirectly through efflux of excess of K^+ following the opening of mitoBK. The exchange of K^+ for H^+ by the H^+/ K^+ antiporter acidifies the mitochondrial matrix.

Certain observations indicate that a small controlled change in the protonmotive force can improve the metabolic efficiency of the ETC. Thus, treatment of guinea pig heart mitochondria with mitoBK channel opener NS11021 led to a small depolarization by 5-10 mV and mitochondrial swelling. At the same time, the efficiency of mitochondrial respiration was enhanced: stage 4 respiration decreased, whereas stage 3 remained unaltered [97]. While benzimidazole derivatives like NS11021 may have unspecific effects on other mitochondrial proteins, this observation was made using a low dose of NS11021 (50 nM) and the effects were sensitive to inhibition of channels with paxilline and charybdotoxin.

Hyperpolarization of mitochondria is associated with increased ROS synthesis by the ETC. On the contrary, diminished ROS synthesis due to temporary mild depolarization of mitochondria is known to be beneficiary for mitochondrial function under physiological conditions, such as during mild depolarization that occurs at the M-phase of cell cycle progression and leads to a decreased generation of ROS by the complex III [98]. Studies with the mitoBK channel openers confirmed a similar effect on the ROS synthesis by the RC enzymes. The mild mitochondrial depolarization due to the BK channel opening was reported to reduce the ROS generation by complex I of the rat brain mitochondria [99]. In another study, genetically induced overactivation of BK channels was used as an approach to eliminate potential non-specific effects of the pharmacological mitoBK modulators: a model of mice with a gain-of-function BK_{R207Q} mutation of BK channels was developed [100]. Similar to the observations in the WT mice, the BK_{R207Q} channel was targeted exclusively to the mitochondria of cardiomyocytes. An overactivation of mitoBK channels conferred a cardioprotective effect in an ischemia/reperfusion injury via mild uncoupling and attenuation of ROS synthesis by ETC complexes I and III.

Therefore, by improving the efficiency of the ETC, mitoBK channels can modulate ROS generation. The physiological relevance of this aspect of the interaction of mitoBK and ETC is highlighted by the feedback loop mechanisms regulating the activity of mitoBK channels by hypoxia and ROS species.

An indirect effect of activation of mitoBK channels is mediated by their role in the regulation of Ca^{2+} homeostasis and signaling. Decreased mitoBK channel activity, as reported due to pharmacological inhibition of mitoBK channels by paxilline and genetic deficiency in *KCNMB1*, impairs mitochondrial Ca^{2+} retention capacity in rodent cardiomyocytes [101]. Through

changes in the mitochondrial Ca^{2+} retention capacity, mitoBK activity indirectly affects the activity of Ca^{2+}-regulated enzymes, including complex IV of ETC [102,103].

Another mechanism of a delayed modulation of ETC activity by mitoBK channels can be executed through control over the availability of respiratory substrates and metabolites. An entry of osmotically obligated water following the influx of K^+ locally dilutes the electrolytes in the matrix. The physiological relevance of this phenomenon remains to be elucidated.

Considering the complex implications of the functionally related activities of mitoBK channels and the ETC complexes, their potential physical interaction would be an intriguing possibility. Indeed, the growing body of research indicates that the mitoBK channel can functionally interact with the respiratory chain and thereby regulate the mitoBK channel function.

In a patch-clamp study of the functional interaction between mitoBK channels and ETC complexes in astrocytoma mitochondria, it was shown that mitoBK channel activity was inhibited after the addition of the respiratory substrates [104] . Structural interaction between cytochrome *c* oxidase and the mitoBK-β4 subunit was shown in the same study, which mediated the functional coupling. Colocalization and interaction of an auxiliary BK-β1 subunit with COX1 were also confirmed in rat cardiomyocytes [105]. Interaction of mitoBK-α with the subunits of the respiratory chain complexes I, III and IV was detected among other mitochondrial protein partners in a proteomic study [106].

However, the involvement of the BK-α subunit in the interaction between the respiratory chain complexes and mitoBK channels is still unclear. The question of the effect of the deficiency of the ETC on mitoBK channels remains open as well.

3.6. MitoBK channels in mitochondrial signaling

3.6.1. Mitochondrial retrograde signaling pathways

Co-evolution of the proto-nuclear and proto-mitochondrial genomes has led to the development of the anterograde and retrograde signaling pathways, which relay the signals about the altered functional and metabolic state of these organelles and coordinate their response to the environmental changes. The triggers of mitochondrial retrograde signaling comprise various mitochondrial stressors, such as a decrease in the mtDNA copy number, changes in mitochondrial functions caused by mutations in both mitochondrial and nuclear genomes, impairment of protein import, and aberrant ROS signaling [107]. Transmission of signals from mitochondria to the nucleus causes alteration in the cellular gene expression profile, which may serve for cellular adaptation and survival in physiological and pathological conditions. Due to their significance, the mitochondrial retrograde signaling pathways have been identified throughout eukaryotic species - from yeast to mammals [108].

While mtDNA encodes only ~1% of the mitochondrial proteome, the encoded proteins are crucial to the OXPHOS. Accumulation of isolated subunits, highly reactive assembly intermediates, or misassembled ETC complexes poses a threat to the proper functioning of mitochondria. Therefore, coordination of the expression of mtDNA with the expression of the nuclear genes encoding other ETC proteins, as well as the molecular machinery for mtDNA maintenance and expression, is required. In addition, disruptions in the mitochondrial protein import, impaired peptide folding or assembly of multiprotein complexes can become challenging for the maintenance of proteostasis [109]. An excessive generation of ROS as a by-product of the activity of the respiratory chain can pose additional challenges to mitochondrial function.

To coordinate the expression of mitochondrial proteins between the nucleus and mitochondria, and to communicate changes in the mitochondrial functional state, two major retrograde signaling mechanisms have evolved, the signaling of which can occasionally converge [110,111].

One of the pathways relaying the signal of mitochondrial stress to the nucleus and triggering a global transcriptional response is the mitochondrial branch of integrated stress response signaling (ISR) [112]. ISR is a signaling pathway that is initiated in response to various forms of cellular stress and leads to a global reduction in protein synthesis with selective overexpression of stress-responsive genes. The broad range of stress conditions, including severe mitochondrial

depolarization, is detected by four types of protein kinases, the activities of which converge on phosphorylation of the eukaryotic translation initiation factor 2 alpha (eIF2α) [113]:

- Perk - sensing ER stress;
- Gcn2 – sensing amino acid deficiency, activated by uncharged rRNAs;
- Prk – sensing double-stranded RNAs originating from viral infections, also can transduce the signal from mitochondrial unfolded protein response (mtUPR);
- HRI – sensing heme deficiency.

A recently described mammalian pathway characterized the central role of the OMA-DELE1-HRI relay in the integrated stress response signaling originating from mitochondria [114]. Phosphorylated eIF2α translationally induces expression of the central transcriptional regulator of ISR - ATF4. A canonical target of ATF4 induced in the early stages of mtUPR is the transcription factor Chop (encoded by *DDIT3*) [115]. Through a transcriptional control with the other downstream targets of ATF4, including transcriptional regulators ATF3, CHAC1, PCK2, and PPP1R15A, Chop globally decreases cytosolic translation [116].

Correct folding of peptides and assembly of multiprotein complexes, along with clearance of the misfolded proteins, is crucial for mitochondrial protein homeostasis. To prevent misfolding and protein aggregation in mitochondria, a sufficient amount of chaperons must be available for the newly translated peptides [117]. In particular, the genetic defects in the structure of ETC subunits or deficiencies in the molecular machinery for the maintenance of mitochondrial genome can lead to proteotoxic stress and disruption of mitochondrial homeostasis. Detection of the unfolded protein stress in mitochondria initiates a retrograde mitochondrial unfolded protein response (mtUPR) pathway to the nucleus. MtUPR leads to the increase of expression of nuclear-encoded mitochondrial chaperones to increase mitochondrial protein-folding capacity, and transcriptional upregulation of mitochondria-specific quality control proteases to mitigate proteotoxic damage [118]. In particular, the transcription factor ATF5 is involved mitochondria-specific mtUPR signaling, which sets it apart from the ER-specific UPR pathway [119].

The transcription factors DNA damage-inducible transcript 3 protein and CCAAT/enhancer-binding protein-β regulate the expression of several mitochondrial proteases that are involved in mtUPR, such as the mtUPR marker LONP and other AAA-proteases ClpXP, CLPP, and LonP1, located within the mitochondrial matrix and primarily degrading misfolded soluble proteins [120]. Other mitochondrial quality control proteases, such as Paraplegin (encoded by *SPG7*) and YME1L, are anchored within the IMM, and their primary role involves cleavage of

misfolded or misassembled subunits of the ETC. The upregulated transcription of mitochondrial chaperons to increase mitochondrial protein folding capacity primarily affects Hsp70 (encoded by *HSPA9*), Hsp60 (*HSPD1*) and Hsp10 (*HSPE1*) [121].

Interestingly, activation of mtUPR can lead to a selective decrease in the expression of mtDNA and nuclear-encoded OXPHOS genes to unburden the overwhelmed mitochondrial proteostasis maintenance systems. Disruptions in mtUPR are reported to have a pathophysiological role in cancer and neurodegenerative diseases such as Alzheimer's disease, Parkinson's disease, and amyotrophic lateral sclerosis [118,122].

The signaling networks conducting the mitochondrial quality control survey multiple mitochondrial parameters, including the changes in mitochondrial membrane potential. A loss of mitochondrial potential is a crucial event in triggering PINK1-Parkin mitophagy, as electrophoretic import of the PINK1 into the depolarized mitochondria through the TOM/TIM complexes is abolished. Accumulation of PINK1 on the surface of OMM leads to mitofusin 2–mediated recruitment of Parkin and its ubiquitination of peptide chains of OMM proteins, which are then recognized by the autophagosome [123].

While the vast majority of work in the area of retrograde signaling research addressed the molecular mechanisms mediating signal transduction and its impact on mitochondrial metabolic pathways, there is limited research investigating the broader role of retrograde signaling on the regulation of ion fluxes in mitochondria. To date, no study has looked specifically into the role of potassium channels in the retrograde signaling mechanisms triggered by mitochondrial disorders.

3.6.2. MitoBK channels in heme and carbon monoxide signaling

Due to the role of mitoBK in the regulation of mitochondrial functions, the research of molecular mechanisms of endogenous modulation of mitoBK channels has gained considerable interest. Multimodal ways of functional mitoBK channel regulation have been reported with various classes of biologically active molecules involved, such as hydrogen sulfide, cGMP (through the action of protein kinase G), flavonoids [124–126]. However, considering the limitations of this work, this chapter will focus on a more detailed overview of the putative role of mitoBK in the mitochondrial heme signaling pathways.

Heme is a well-known regulator of the activity of plasma membrane BK channels: BK channels possess the heme-binding motif within their C-terminal part and were shown to be inhibited by heme [127,128]. Interestingly, the binding of an oxidized form of heme – hemin – was reported to decrease the channel activity of mitoBK channels as well, suggesting that they also likely possess a heme-binding structural motif [129]. Therefore, a potential inhibition of mitoBK channels by heme can be a part of a cytotoxic phenomenon in the pathological conditions characterized by an excessive intracellular amount of heme, such as during stroke, when neurons and astrocytes can accumulate up to millimolar levels of heme.

Free heme can be eliminated in the heme degradation pathway involving heme oxygenase, which produces carbon monoxide (CO) as a byproduct [130]. Since the chemical reactivity of CO is low, its primary intracellular targets are confined to metalloproteins containing transition metals - in particular, hemoproteins. Their oxidation status is relevant as another layer of regulation of CO signaling since CO only binds to the ferrous (Fe^{2+}) heme [130].

CO has gained growing attention as a signaling molecule in recent years. Currently, the role of CO as a gaseous transmitter that controls a wide range of physiological processes is well established [131–133]. The putative benefits of therapeutic CO application, however, are negated by its systemic toxicity due to its interaction with hemoglobin that produces carboxyhemoglobin. Therefore, CO-releasing molecules (CORMs) have been developed to bypass these concerns and allow for the safe and regulated release of CO [134]. The currently available forms of CORMs come in different chemical classes of compounds and have been extensively applied as a tool for the controlled CO release in the research of CO signaling pathways [135,136]. Thus, in situ activation of the mitoBK channel in astrocytoma mitochondria by a direct application of CORM-401 was shown [137]. Yet, a growing number of reports are addressing the unspecific effects of CORMs [138–140].

Mitochondria are a major organelle target for CO signaling because they harbor proteins for heme synthesis and contain a variety of hemoproteins [141]. In particular, cytochrome *c* oxidase can be inhibited by CO in physiological concentrations, leading to the stalling of complex III in a reduced state and producing ROS that can initiate oxidative signaling pathways. By binding mitochondrially produced heme, mitoBK channels can be an interesting target for CO action.

3.6.3. The role of mitoBK channels in cytoprotective signaling

The signature biophysical characteristics of mitoBK channels, such as large conductance and joint gating regulation by voltage and calcium ions, endow them with multiple physiological functions. Over the years, a large amount of research has been devoted to molecular mechanisms of a cytoprotective role of mitoBK channels in pathological conditions.

In aging cells due to the accumulation of mtDNA mutation and action of ROS, mitochondria experience significant functional impairments. They are reflected in the change of mitochondrial dynamics, glucose metabolism, as well as impairment of the OXPHOS, ROS signaling, and Ca^{2+} overload [142,143]. In the cells where oxidative phosphorylation is a major source of ATP synthesis, such as neurons, mitochondrial impairments associated with aging can lead to neurodegenerative diseases. Thus, an increased interest has emerged in the implication of mitoBK in mitochondrial signaling in cardio- and neurodegenerative diseases in recent years [144].

Alongside mitoK_{ATP} channels, mitoBK channels have been widely studied in the context of their role in the preconditioning phenomenon against ischemic injury. In the preconditioning studies using BK channel openers such as NS11021 and NS1619, prior activation of the BK channels has decreased the deteriorative effect of ischemia on the heart function and reduced the infarct size. The preconditioning effect was abolished by inhibition of the channels with a BK inhibitor paxilline. Since only mitoBK channels are expressed by the cardiomyocytes, the role of mitochondrial channels was directly implicated in this effect. The molecular mechanisms mediating a cytoprotective effect of the mitoBK channel opening involved modulation of reactive oxygen species generation and signaling, and modulation of mitochondrial calcium uptake.

In cardiomyocytes, mitoBK channels exerted a cytoprotective effect against ischemia-reperfusion injury, which was mediated through ROS signaling [145]. Activation of mitoBK

channels by CGS7184 in isolated brain mitochondria led to decreased ROS synthesis by complex I [99].

The immediate protein environment of BK channels in cellular compartments determines their role in the Ca^{2+} signaling pathways. Interaction with calcium channels with different regulating mechanisms determines whether plasma membrane BK channels act as negative feedback regulators for Ca^{2+} influx, as in the case when they form protein complexes with Ca_V channels in excitable cells, or positive feedback regulators when BK channels interact with the TRP channels and P2X purinoreceptors in non-excitable cells. In mitochondria, however, the opening of mitoBK channels in response to an increase in the Ca^{2+} levels and a rapid influx of potassium ions leads to local depolarization of IMM and decreases the driving force for Ca^{2+} entry, thus primarily serving as a negative feedback regulator. As a case in point, deposition of amyloid beta characteristic for Alzheimer's disease was shown to inhibit mitoBK channels, what leads to an increase in Ca^{2+} concentration in mitochondria [86,146]. In the study of the effects of mitoBK channels on the mitochondrial Ca^{2+}-retention capacity, Ca^{2+}-activated mPTP opening was stimulated after inhibition of mitoBK channels with iberiotoxin [147].

The systemic consequences of genetic knockout models are too complex to be attributed solely to the plasma membrane or mitochondrial forms of BK channels. Evidence of the *KCNMA1* knockout mouse model demonstrated that in mammals the lack of BK channels is not fatal. However, *KCNMA1* deficient mice displayed impairment in learning, and detrimental effects on the central nervous system were strongly pronounced [148]. Mutations in *KCNMA1* have been linked to epilepsy disorders, which are often accompanied by paroxysmal dyskinesia and developmental delays [149]. Both loss-of-function and gain-of-function BK mutations were described in epilepsy, often affecting the C-terminal channel part.

A presence of the mitoBK channel was identified in mitochondria of *Drosophila melanogaster*. Mutation in the BK channel affected mitochondrial morphology and led to an increase in ROS generation, which was associated with reduced lifespan [150]. Cytoprotective activation of mitoBK channels can be an effector of signaling pathways. In a study of a cGMP-mediated signaling pathway, activation of mitoBK channel by protein kinase G was shown, and it had a cytoprotective effect in the coronary arteries [151].

Therefore, ample evidence supports that activation of mitoBK channels can be cytoprotective due to its modulatory effects on the OXPHOS, ROS synthesis, and mitochondrial signaling.

4. AIMS OF THE STUDY

The general aim of this study was to investigate the interaction of the mitoBK channel with the cytochrome *c* oxidase (COX) and to gain insight into the systemic modulation of the mitoBK channel by the carbon monoxide (CO).

The specific aims of this study included:

1. Confirmation of the expression of mitoBK-α subunit in the studied cell models: human astrocytoma cells, human dermal fibroblasts.

2. Pharmacological induction of mtDNA depletion in the astrocytoma cells to obtain the cellular system void of functional respiratory chain (RC). Confirmation of the abolishment of respiration by these cells.

3. Characterization of steady-state protein complexes formed by the mitoBK channels with the COX in the WT cells and the cells devoid of mtDNA.

4. Evaluation of the steady-state mitoBK-α subunit protein and transcript amount in these cell lines.

5. Study of the transcriptome to analyze gene signaling pathways activated in the mtDNA-depleted cells.

6. Modeling of the genetic deficiency in COX8A in the HEK293T cells with a CRISPR/Cas9 gene-editing system. Identification of mutant clonal cell lines by screening.

7. Characterization of the RC protein complexes formed by the human dermal fibroblasts of the patient with a genetic deficiency in COX8A.

8. Characterization of the RC protein complexes formed by the HEK293T cells with an induced deficiency in COX8A.

9. Characterization of steady-state protein complexes formed by the mitoBK channels with the RC complexes in COX8A-deficient fibroblasts.

10. Evaluation of the steady-state mitoBK-α subunit protein and transcript amount in COX8A-deficient fibroblasts.

11. Study of the transcriptome of COX8A-deficient fibroblasts and HEK293T to analyze gene signaling pathways activated upon COX8A deficiency.

12. Electrophysiological study to analyze the effects of three structurally different CORMs on mitoBK channel activity in the astrocytoma mitochondria.

13. Electrophysiological evaluation of the effects of hemin, heme, and CO on mitoBK channel activity in the astrocytoma mitochondria.

5. MATERIALS AND METHODS

5.1. Chemicals

The chemicals used in this work are indicated in the Table 3.

Table 3. Chemicals and suppliers.

Chemical	Manufacturer
2',3'-dideoxycytidine (ddC)	Sigma-Aldrich
4-(2-hydroxyethyl)-1-piperazineethanesulfonic acid (HEPES)	Sigma-Aldrich
5,5′-Dithiobis(2-nitrobenzoic acid) (DTNB)	Sigma-Aldrich
6-aminohexanoic acid (ε-aminocaproic acid)	Serva Electrophoresis
Acrylamide	Sigma-Aldrich
Acrylamide/Bis solution, 37.5:1	BIO-RAD
Agarose	Sigma-Aldrich
Amersham™ ECL Prime Western Blotting Detection Reagent	GE Healthcare
Ammonium persulfate (APS)	Carl Roth
Bis(2-hydroxyethyl)amino-tris(hydroxymethyl)methane (Bis-Tris)	Carl Roth
Bovine serum albumin	Sigma-Aldrich
Calcium chloride ($CaCl_2$)	Sigma-Aldrich
Carbon monoxide gas (CO)	Multax s.c.
Carbonyl cyanide 3-chlorophenylhydrazone (CCCP)	Sigma-Aldrich
CGS7184	Novartis Pharma
Chloroform	Sigma-Aldrich
Coenzyme Q_1 (CoQ_1)	Sigma-Aldrich
cOmplete, Mini Protease Inhibitor Cocktail	Roche
Coomassie Brilliant Blue G	BIO-RAD
Coomassie Brilliant Blue R-250 staining solution	BIO-RAD
CORM-2 (tricarbonyldichlororuthenium(II) dimer)	Sigma-Aldrich
CORM-401 (tetracarbonyl[N-(dithiocarboxy-kS, kS′)-N-methylglycine]manganite)	Sigma-Aldrich
CORM-A1 (sodium boranocarbonate)	Sigma-Aldrich
Cytochrome *c* from bovine heart	Sigma-Aldrich
Digitonin	Serva Electrophoresis
Dimethyl sulfoxide (DMSO)	Sigma-Aldrich

Dulbecco's modified Eagle's medium	Thermo Fisher Scientific; Ludwik Hirszfeld Institute of Immunology and Experimental Therapy
ECL Prime	GE Healthcare
Ethanol	Sigma-Aldrich
Ethidium bromide	Sigma-Aldrich
Ethylenedinitrilotetraacetic acid (EDTA)	Sigma-Aldrich
Fetal bovine serum	Gibco
GeneJuice transfection reagent	Sigma-Aldrich
Glycerol	Sigma-Aldrich
Glycine	Serva Electrophoresis
Hemin	Sigma-Aldrich
HMW Native Marker Kit	GE Healthcare
Hydrochloric acid (HCl)	Sigma-Aldrich
Lauryl maltoside	Abcam
L-Glutamine	Gibco
Methanol	Sigma-Aldrich
Midori Green	Nippon Genetics
Myoglobin from equine heart	Sigma-Aldrich
Normal donkey serum	Abcam
Oxaloacetatic acid	Sigma-Aldrich
PageRuler pre-stained protein ladder	Thermo-Fisher
PageRuler™ Prestained Protein Ladder	Thermo-Fisher
Paraformaldehyde (PFA)	Sigma-Aldrich
Paxilline	Sigma-Aldrich
Penicillin-streptomycin	Invitrogen, Sigma-Aldrich
Phenylmethylsulfonyl fluoride (PMSF)	Sigma-Aldrich
Phosphate buffer saline (PBS)	Invitrogen
Potassium chloride (KCl)	Sigma-Aldrich
Potassium cyanide (KCN)	Sigma-Aldrich
Potassium hydroxide (KOH)	Sigma-Aldrich
Protein marker IV (pre-stained), peqGOLD	Avantor
PVDF (polyvinylidene difluoride) membranes	Carl Roth
Saponin	Sigma-Aldrich
Sodium chloride (NaCl)	Sigma-Aldrich
Sodium dithionite	Merck
Sodium dodecyl sulphate (SDS)	Sigma-Aldrich
Sucrose	Sigma-Aldrich
SuperSignal West Pico Chemiluminescent substrate	Thermo Fisher Scientific
Tetramethylethylendiamin (TEMED)	Sigma-Aldrich
The Pierce BCA protein assay kit	Thermo-Fisher
Tris-acetate-EDTA (TAE)	Thermo Fisher Scientific

Trizma (Tris)	Sigma-Aldrich
TRIzol Reagent	Invitrogen
Tween 20	BIO-RAD
Uridine	Sigma-Aldrich
VECTASHIELD Mounting Medium with DAPI	Vector laboratories
β-mercaptoethanol	Sigma-Aldrich
β-Nicotinamide adenine dinucleotide (NADH)	Sigma-Aldrich

5.2. Cellular models

The experiments were performed on U-87 MG human astrocytoma cells, human dermal fibroblasts, and HEK293T cells. The genetic data for human dermal fibroblasts of a patient with Leigh syndrome and epilepsy harboring a homozygous splice site mutation in *COX8A* has been previously published [152]. Fibroblasts of an age-matched donor were used as control cells.

The cells were maintained in a humidified incubation environment at 37°C containing 5% CO_2. The cell growth medium was composed of Dulbecco's modified Eagle's medium supplemented with 10% fetal bovine serum, 2 mM L-glutamine, 100 U/ml penicillin, and 100 µg/ml streptomycin. The cells were fed every third day and reseeded upon reaching 80% confluence.

5.3. Depletion of mtDNA in the astrocytoma cells

U-87 MG astrocytoma cells were treated with the nucleoside analog 2',3'-dideoxycytidine (ddC), which was shown to inhibit the DNA-polymerase gamma [153]. DdC was supplemented to the standard cell culture medium at all times, and the cell culture medium was replaced every third day. While the addition of ddC to the medium to the final concentration of 20 µM was tolerable by the cells, an increase to 50 µM or higher values has led to a complete stunt in the cell growth and a sharp increase in the cell death. Therefore, the final concentration of 20 µM of ddC has been used in all experiments for mtDNA depletion. Uridine was also supplemented at the concentration of 50 µg/ml.

5.4. Induction of COX8A deficiency in HEK293T cells with CRISPR/Cas9

CRISPR/Cas9 constructs containing single guide RNA (sgRNA) targeting exon 1 of *COX8A* were used for gene editing of the HEK293T cells. The choice of the sgRNA sequence for

CRISPR/Cas9 constructs was facilitated by the Broad Institute's and Synthego sgRNA designer programs (Figure 7).

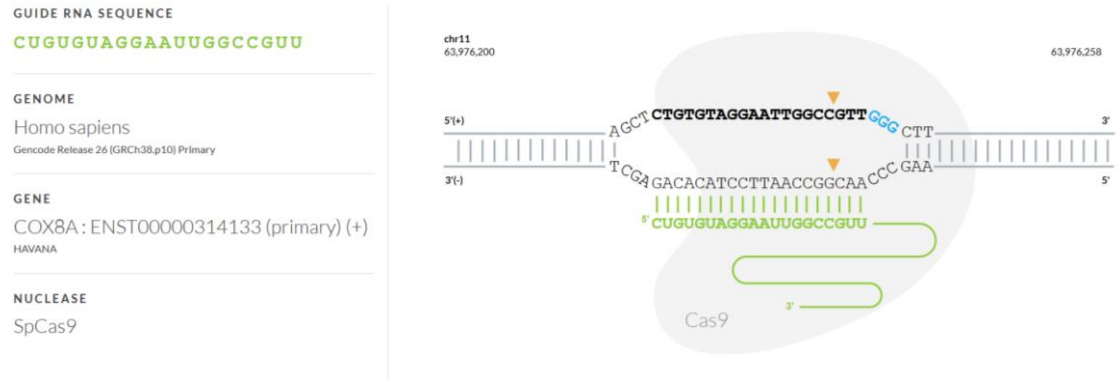

Figure 7. Illustration of the principle of the operation of the designed CRISPR/Cas9 construct targeting *COX8A* using the Synthego sgRNA designer program.

Cloning of the dsDNA oligonucleotides encoding gRNA was performed into pSpCas9(BB)-2A-GFP (Addgene) as described elsewhere [154]. GeneJuice transfection reagent (Sigma-Aldrich) was used to transfect HEK293T cells with the CRISPR/Cas9 construct-containing plasmid according to the manufacturer's instructions. To isolate single-cell clones, the viable cells were counted, the cell suspension was diluted for the expected single cell per well density, and seeded onto 96-well plates 24 hours after transfection. After the establishment of stable clonal colonies, the cells were split and a fraction of them was collected for DNA isolation by a commercially available kit (The QIAamp DNA Mini Kit, Qiagen) for screening by Sanger sequencing.

5.5. Nucleic acid isolation

5.5.1. RNA isolation

Two methodologically different approaches were used for the RNA isolation, depending on its downstream application. For the expected applications as a template in RT-PCR and qRT-PCR, total RNA was extracted from cells with a commercially available spin column-based kit using a method according to the manufacturer's instructions (RNeasy Mini Kit, Qiagen). After spectroscopic evaluation of the purity and yield of collected RNA, the samples were immediately utilized for downstream applications.

For the expected application as a template for the creation of cDNA libraries in the transcriptome 3'-RNA sequencing study, an additional step was introduced in RNA isolation to

improve the purity and stability of yielded RNA. Specifically, prior to the isolation of the silica-membrane column of the commercial kit, RNA was extracted with the standard phenol/chloroform method. Incubating the cell pellet in TRIzol Reagent (Invitrogen) produced cellular lysate, which was subsequently subjected to the mechanical lysis in commercially available QIAshredder tubes (Qiagen). While the manufacturer of TRIzol Reagent does not disclose its protected formula, phenol and guanidine isothiocyanate are contained in the formulation of this product. Therefore, to facilitate dissociation of the nucleoprotein complexes by guanidine isothiocyanate at this stage, the collected cellular lysate was incubated at the RT for 5 min. Afterward, chloroform was added to the lysate, incubated for 15 min at the RT, and centrifuged for 15 min at 12000 g at 4°C. Phase separation recovered three phases from the sample: the top RNA-containing aqueous phase, the DNA-containing interphase, and the bottom protein and lipid-containing organic phase. The RNA-containing aqueous phase was collected, mixed with 70% ethanol, and transferred onto silica-membrane columns of the RNeasy Mini Kit. The subsequent steps of RNA isolation were conducted in a regular manner according to the manufacturer's instructions.

5.5.2. DNA isolation

The cultivated cells were mechanically scraped off in the cold PBS, and the cell pellets were recovered by centrifugation at 800 g for 10 minutes. The silica membrane-based spin column kit (QIAamp DNA Mini Kit, Qiagen) was then used to extract total genomic DNA according to the manufacturer's protocol. The DNA samples were eluted in water and stored at -20°C until they were utilized for the downstream application.

5.5.3. Spectrophotometric nucleic acid quantification

The purity and yield of isolated RNA or DNA in the samples were estimated spectrophotometrically with Cary 60 UV-VIS spectrophotometer (Agilent Technologies) or Nanodrop 2000 (Thermo Scientific).

The Lambert-Beer law was applied for the estimation of concentration of isolated DNA or RNA:

$$A = \varepsilon c l \,,$$

where A is the absorbance, ε is the attenuation coefficient (the standard coefficients are 0.020 $\mu g \cdot mL^{-1} \cdot cm^{-1}$ for dsDNA, 0.025 $\mu g \cdot mL^{-1} \cdot cm^{-1}$ for RNA), c is the concentration of the attenuating compound, l is the optical path length.

The absorbance values were measured at the following wavelengths: λ = 230 nm, λ = 260 nm, λ = 280 nm. For RNA probes, the absorbance ratio $A_{260/A280}$ was within the range of 1.8 – 2.0, what denotes that the DNase treatment step in a commercial kit procedure purified the samples from DNA. The absorbance ratio $A_{260/A230}$ was 2.0 or higher, indicating no contamination of the eluate by phenol and proteins.

5.6. Thermal cycling-based gene expression evaluation

5.6.1. Reverse transcription of total RNA

Reverse transcription of RNA for the downstream PCR applications was performed directly after RNA isolation and quantification with an iScript Select cDNA Synthesis Kit (Bio-Rad) as described below, using a random primer set provided in the kit:

Reagents	**Volume per 1 reaction**
Template RNA	Corresponding to 1 µg
5x iScript reaction mix	4 µl
Random primers	2 µl
Reverse transcriptase	1 µl
Water	Variable
Total volume	20 µl

The reaction mixes were placed into a thermocycler (Bio-Rad) with a following programmed temperature protocol:

5 min at 25°C

30 min at 42°C

5 min at 85°C

hold on 12°C.

5.6.2. Polymerase chain reaction (PCR)

The primers for PCR were designed with the Primer-BLAST software (National Library of Medicine, USA) (Table 4). The annealing temperatures for each primer pair were selected through optimization of the predicted temperature in the prior gradient PCR.

Table 4. Primer sequences and annealing temperatures

Gene	Primer sequence	Designed product size, bp	Annealing temperature, °C
KCNMA1 (for RT-PCR)	F: CCA TCC ACA GCA AAC CGG CCA R: TGA GTA AGT AGA CAC ATT CCC	312	60.0
KCNMB1	F: CCA GAA CCA GCA GGT ACT CA R: CCA GGT CTG TGT CAC TCC AA	160	61.0
KCNMB2	F: CAC TGA AGG CAG GAG AGG AC R: GTC CAC ACG CTC TGC ATG TA	150	58.4
KCNMB2 (nested outer primers)	F: CAG TGG CCG GAC CTC TTC R: GGA ACA GCA CGT TGG AAC TG	578	60.2
KCNMB3	F: ATC ATG GAC GAC TGG CTG GA R: GTC TGT AAC ATC ACG CTT GGG A	171	61.6
KCNMB4	F: AGG TGA AGG TGC ACT CGA AC R: GTG GCT TAC GAG TAC ACG CA	205	58.8
GAPDH	F: CAA GGT CAT CCA TGA CAA CTT TG R: GTC CAC CAC CCT GTT GCT GTA G	495	58.0

For the qualitative detection of gene expression, cDNA was amplified using the JumpStart REDTaq Ready Mix (Sigma-Aldrich) according the reaction mix scheme shown below:

Reagents	Volume per 1 reaction
Template cDNA	1 µl
Jumpstart REDTaq Ready mix	12.5 µl
Forward primer	1 µl
Reverse primer	1 µl
Water	7 µl
DMSO	0.5

5.6.3. Agarose gel electrophoresis

1.5% agarose gel was prepared in Tris-acetate-EDTA (TAE) buffer. 10 µl Midori Green DNA dye was added to 120 ml of liquid agarose mixture. The reaction products in the REDTaq mix were directly loaded into a solidified agarose gel and run at a constant voltage of 130 mV for the duration of time necessary for proper separation (about 60 minutes). For the product size identification, a reference 100 bp DNA ladder (NEB) was loaded into the gel alongside the samples. DNA visualization was performed with the UV-illuminator GelDocTM XR at excitatory wavelengths between 254 and 365 nm.

5.6.4. Quantitative real-time PCR (qRT-PCR)

To quantify expression of *KCNMA1*, qRT-PCR was performed with Sybr Select Master Mix (Thermo Fisher), with the sequences of the primers used for the qRT-PCR and the composition of the reaction mix as specified below:

Reagents	**Volume per 1 reaction**
Template cDNA	1 µl
Sybr Select Master Mix	10 µl
Forward primer	1 µl
Reverse primer	1 µl
Water	7 µl
Total volume	20 µl

Gene	**Primer sequence**	**Designed product size, bp**	**Annealing temperature, °C**
KCNMA1 (for qRT-PCR)	F: GAG CAT CTC TCA GCC GGT AA R: CCG CAG ACA CTG GCC AAT AG	166	61.0
GAPDH (for qRT-PCR)	F: TCA GAC ACC ATG GGG AAG GT R: GAA TCA TAT TGG AAC ATG TAA	107	61.0

The reaction mixes were placed into the thermal cycler (Bio-Rad) with a following programmed temperature protocol:

5 min at 95°C,

for 45 cycles:

30 sec at 95°C

1 min at 61°C;

hold on 12°C.

5.7. Sanger sequencing

For amplification of the *COX8A* genomic DNA fragment for downstream Sanger sequencing, PCR was performed with JumpStart Accutaq polymerase (Sigma-Aldrich) according to the protocol described below. The primers for sequencing were designed to be at located least 150 bp away from the gRNA match site with *COX8A* that constituted a potential Cas9 cutting site. All the products of PCR were stored at +4°C.

Reagent	Volume
AccuTaq LA 10 x Buffer	5 µL
dNTP mix	2.5 µL
Template DNA	X µL (total 400 ng)
Forward primer (10 µM)	2 µL
Reverse primer (10 µM)	2 µL
Water, PCR Reagent	(14 – X) µL
Long and Accurate PCR Enzyme (1 unit/µL)	2.5 µL
Total volume	50 µL

Gene	Primer sequence	Designed product size, bp	Annealing temperature, °C
COX8A	F: GCC ATT TGG GCT TCC TGA CCT T R: CAG GCA TCC CCC AGT GAA C	491	62

The following thermocycler (Bio-Rad) program was used for amplification of the genomic fragment of interest:

90 sec at 98 °C,

for 30 cycles:

denaturation 15 sec at 95 °C

annealing 2 min at 62 °C;

10 min at 72°C.

The products of amplification were purified from the residual primers and nucleotides with the ExoSAP-IT PCR (Thermo Scientific) product cleanup reagent (Thermo Scientific) according to the manufacturer's instruction. After spectrophotometric estimation of the concentration of the final DNA and its dilution in water, the samples were sent for Sanger sequencing by the commercial company (Eurofins).

5.8. High-throughput whole-transcriptome sequencing

5.8.1. Library preparation and sequencing

To evaluate the expression levels of mitochondria- and nuclear-encoded mitochondrial proteins, isolated total RNA was analyzed by 3'-RNA sequencing. RNA integrity number of the total RNA was controlled using the Agilent TapeStation and was higher than 7 in all samples. The complementary DNA (cDNA) library was prepared from total RNA using the QuantSeq 3'-mRNA-Seq Library Prep Kit (Illumina), producing the cDNA library that was enriched in the sequences in the immediate proximity to the 3'-end of the transcribed polyadenylated RNA. The sequencing was performed on a HiSeq 2500 sequencing platform (Illumina) in the high output mode.

5.8.2. RNAseq data processing

The FASTQ sequencing output files were mapped to the Homo sapiens genome assembly GRCh38 (hg38) obtained from the Genome Reference Consortium using the UCSC gene annotation file. The RNA STAR aligner was used on the Galaxy platform in the two-pass mode following the software instruction manual. The mapped reads were quantified using the featureCounts algorithm. Normalization of the read counts and statistical evaluation of differential gene expression was performed by the R/Bioconductor DESeq2 software package.

5.9. Isolation of mitochondria from cultured cells

Standard solation of mitochondria was performed as previously described [104]. Briefly, the cells were harvested and pelleted at 800 g. The cell pellet was resuspended in ice-cold solution A (250 mM sucrose, 5 mM HEPES, pH = 7.2) and homogenized in a glass potter. The homogenate

was centrifuged at 780 g for 10 min at 4°C. The supernatant was collected and centrifuged in the ice-cold solution A at 9200 g for 10 min at 4°C. The pellet was washed and resuspended in the ice-cold solution A and centrifuged at 9200 g for 10 min at 4°C. The pellet containing mitochondria was resuspended in the ice-cold solution B (150 mM KCl, 10 mM HEPES, pH = 7.2) and kept on ice.

In case the mitochondrial preparations were to be used for the protein analysis, the protease inhibitor cocktail was added to solutions A and B (Complete Mini, Roche). However, it was avoided in the mitochondrial preparations for the patch-clamp analysis in order to minimize pharmacological interactions with the ion channels and their protein partners.

Isolation of mitochondria with the magnetic beads-based method, the suitability of which was evaluated for the assessment of protein complexes of mitoBK channels with the respiratory chain in astrocytoma cells, was performed with a commercially available mitochondrial isolation kit according to the manufacturer's instructions (Miltenyi Biotech).

5.10. Western blot assessment of the amount and composition of proteins and protein complexes

5.10.1. Determination of protein concentration

Following each mitochondrial isolation for the Western blot experiments, an aliquot of the isolated sample was reserved for quantification of protein content. The Pierce BCA protein assay kit (Thermo Scientific) was selected for estimation of the protein concentration since this method is not sensitive to a wide range of detergents. For accurate quantification of the mitochondrial membrane proteins, the content of mitochondrial aliquots was solubilized with 5% SDS (v/v). The measurements were performed according to the manufacturer's instructions. Following incubation of the samples, protein concentration was inferred from the absorbance of the Cu^{+}-bicinchoninic acid complex at 562 nm. The supplied bovine serum albumin was used to prepare a standard curve, and the sample protein concentration was interpolated on it using GraphPad Prism 8.

5.10.2. SDS-PAGE protein electrophoresis

For SDS-PAGE, aliquots of mitochondrial preparation were solubilized by incubation in 4X Laemmli sample buffer (Bio-Rad) containing 1% β-mercaptoethanol at 60°C for 15 min. The samples were then loaded alongside a PageRuler pre-stained protein ladder (Thermo Scientific) into the 12.5% SDS polyacrylamide gel and separated by electrophoresis.

5.10.3. Blue-native PAGE protein electrophoresis

For BN-PAGE, mitochondrial aliquots were solubilized in a digitonin-containing solution (10% v/v glycerol, 1% v/v digitonin, 50 mM NaCl, 20 mM Tris-HCl, 0.1 mM EDTA, 1 mM PMSF, pH=7.4). The samples were incubated on ice for 15 min. The solubilized mitochondria were centrifuged for 10 min at 9200 g at 4°C, and the supernatant was collected. The loading dye (1.5 M aminocaproic acid, 50 mM Bis-Tris-HCl, 5% Coomassie brilliant blue, pH=7.0) was added to the supernatant to a final concentration of 1/3 of the total probe volume. The probe containing 100 µg protein per lane was next loaded into a 4-10% gradient blue native polyacrylamide gel and mitochondrial protein complexes were separated by electrophoresis at 4°C.

5.10.4. Immunostaining and protein detection

Following BN-PAGE or SDS-PAGE, the gels were electroblotted onto polyvinylidene fluoride (PVDF) membranes. The PVDF membranes were immunoprobed with the primary antibodies raised against proteins of interest as described in Table 5.

The antibody detection was performed with appropriate secondary antibodies conjugated to horseradish peroxidase raised against the organism hosting the primary antibody: anti-mouse (GE Healthcare NA931V) or anti-rabbit (GE Healthcare NA9340V). The signal was visualized with chemiluminescent detection reagents according to the manufacturer's instructions.

Table 5. Characteristics of primary antibodies used in the Western blot studies.

Name of the target	Company/code	Clonality	Host organism	Dilution	Incubation time
BK channel subunits					
BK-α	Neuromab 022, clone L6/60	M	Mouse	1:200	overnight
BK-β3	Neuromab N40B/18, clone N40B/18	M	Mouse	1:200	overnight
BK-β4	Alomone APC 061	P	Rabbit	1:200	overnight
Complex IV of respiratory chain					
COX5A	Thermofischer PA5-27432	P	rabbit	1:1000	overnight
COX1	Invitrogen 1D6E1A8	M	Mouse	1:1000	overnight
COX4	Cell signaling 4844s	P	rabbit	1:1000	overnight
COX2	Invitrogen 12C4F12	M	Mouse	1:1000	overnight
Complex I of respiratory chain					
NDUFA9	Abcam ab14713	M	Mouse	1:1000	overnight
Complex II of respiratory chain					
SDHA	Abcam ab137040	M	Rabbit	1:1000	overnight
Complex III of respiratory chain					

CORE2	Abcam ab14745	M	mouse	1:1000	overnight
ATP-synthase					
ATP-synthase subunit c	Abcam ab181243	M	Rabbit	1:1000	overnight
Transporters and other proteins					
TOM-20	Santa-Cruz 17764	M	Mouse	1:500	overnight
VDAC	Abcam ab15895	P	Rabbit	1:1000	overnight
MCU	Sigma HPA016480	P	Rabbit	1:200	overnight
HSP75	Abcam ab182775	P	Rabbit	1:1000	overnight

5.11. Confocal microscopy cell imaging

5.11.1. Immunocytochemical staining

The cells were seeded onto a glass coverslip in a standard growth medium and grown as a monolayer in its exponential growth phase. To prepare the sample for immunocytochemical staining, a residual amount of cell growth medium was removed by triple delicate washing of the cells for 5 min in 0.5 ml PBS. Next, the cells were fixed in ice-cold 4% paraformaldehyde (PFA) solution in PBS for 30 min. PFA was removed from the cells by triple washing for 5 min with 0.5 ml PBS. The free aldehyde groups introduced after the PFA fixation were quenched by incubating the sample in 50 mM ammonium chloride solution in PBS for 15 min, followed by the wash in PBS. Next, the cells were permeabilized and blocked by incubation in the blocking buffer containing 0.075% saponin, 1% SDS, and 5% normal donkey serum for 30 min at the room temperature. The cells were then incubated overnight at 4°C with a blocking buffer containing primary anti-VDAC antibodies (1:500). Following a wash in PBS, the cells were incubated in the blocking buffer containing goat anti-rabbit Alexa Fluor 633-conjugated secondary antibodies (1:500, Thermo Scientific) for 1 h at room temperature. After the final PBS washes, the samples were mounted in a Vectashield DAPI-containing medium and directly used for visualization.

5.11.2. Sample visualization

The microscopical examination of immunostained cells was performed with the confocal microscope Olympus FluoView 1200 (Olympus, Spain). The laser system settings were selected taking into account the spectral properties of fluorophores: a diode laser emitting at 635 nm for excitation of Alexa Fluor 633, and a diode laser emitting at 405 nm for excitation of DAPI. The signal detection parameters were adjusted to capture the emission peak of Alexa Fluor 633 at 650 nm and the emission peak of DAPI at 470 nm. Analysis of microscopy images was performed with ImageJ version 1.51k (National Institutes of Health, USA).

5.12. Patch-clamp on the ion channels of the inner mitochondrial membrane

Patch-clamp experiments on the ion channels of the inner mitochondrial membrane were performed as previously described [67,71,155]. Briefly, a fraction of the isolated mitochondria was subjected to osmotic shock by being placed into a hypotonic solution (5 mM HEPES and 100 µM $CaCl_2$, pH = 7.2) for about 1 min. To restore the tonicity of the bath chamber solution to isotonic conditions (150 mM KCl, 10 mM HEPES, and 100 µM $CaCl_2$, pH=7.2), hypertonic solution (750 mM KCl, 30 mM HEPES, and 100 µM $CaCl_2$, pH=7.2) was added dropwise to the mitoplast suspension previously obtained. Floating mitoplasts were visually identified using an inverted microscope and selected by attaching a borosilicate glass patch-clamp pipette. The pipette was filled with an isotonic solution (150 mM KCl, 10 mM HEPES, and 100 µM $CaCl_2$, pH= 7.2).

The patch-clamp recordings were made in inside-out mode, in which the matrix-facing the IMM side was exposed to the perfusion solution. The exchange of the experimental solution was made by positioning the patch pipette into the glass tube openings of a “sewer pipe” perfusion system (made in-house with a peristaltic pump and tubing from Ismatec, Germany). The channel modulators were diluted, as indicated, either in the isotonic solution containing 100 µM free Ca^{2+} or in the solution containing 1 µM free Ca^{2+} (10 mM HEPES, 1 mM EGTA, and 0.752 mM $CaCl_2$, pH=7.2).

The patch-clamp experiments were carried out in the voltage-clamp mode by the patch-clamp amplifier Axopatch 200B (Molecular Devices Corporation). The borosilicate glass pipettes were pulled using a PC-10 puller (Narishige) and had a resistance of 15-20 MΩ. The currents were low-pass filtered at 1 kHz and sampled at a frequency of 100 kHz. The experiments were

recorded in single-channel mode. The probability of a channel opening (NP_o) was estimated using the single-channel search mode of the Clampfit 10.2 Software (Molecular Devices Corporation). Statistical analysis was performed with Student's t-tests, and p-values below 0.05 were considered significant.

5.13. Measurement of respiration of astrocytoma cells

Cellular respiration was measured polarographically with a Clark-type oxygen electrode system (Oxygraph-2k, Oroboros). U-87 MG cells were harvested by trypsinization, counted, and centrifuged at 800 g for 10 min. The cell pellet was then resuspended in respiration medium (DMEM supplemented with 1 % penicillin/streptomycin and 1 % glutamine) and the cellular oxygen consumption rate was measured imminently after stabilization of the baseline parameters. Afterward, the mitochondria of the suspended cells were uncoupled by incremental addition of 1 µM CCCP to the recording chamber. The oxygen consumption rate was normalized to the number of cells in the experimental chamber and presented as O_2/min/10^6 cells. Data acquisition and processing were performed with the DatLab software (Oroboros).

5.14. Perfusion with CO and confirmation of the CO presence with myoglobin assay

Solutions with CO gas were perfused on the day of the experiment by bubbling the solutions with CO gas for 30 min and stored in the gastight sealed vials [156]. Hemin was reduced to heme with dithiothreitol and sodium dithionite as previously described [157].

The saturation of solutions with carbon monoxide was evaluated with a hemoglobin assay on a UV/Vis spectrophotometer (Cary). Myoglobin was dissolved in the experimental buffers supplemented with an excess of a reducing agent sodium dithionite. The solution was then layered over with light mineral oil. The binding of CO to myoglobin changes its typical absorption spectrum by decreasing the values of the peak at $\lambda = 557$ nm and the appearance of the peaks characteristic for carboxymyoglobin at $\lambda = 540$ nm and $\lambda = 577$ nm. The amount of carboxymyoglobin can be evaluated by application of the Lambert – Beer law as described above, using the following attenuation coefficient values: for deoxymyoglobin $\varepsilon_{560nm} = 13.8$ l·mmol^{-1}·cm^{-1}, for carboxymyoglobin $\varepsilon_{540nm} = 15.4$ l·mmol^{-1}·cm^{-1}.

5.15. Determination of mitochondrial enzymatic activities

The samples containing isolated mitochondria were homogenized with a homogenizer in PBS and centrifuged at 16000 g for 15 min at 4°C. The supernatant enriched in the mitochondrial matrix enzymes was collected and used for the measurement of citrate synthase activity. The pellets containing mitochondrial membranes were re-suspended in PBS and used for the determination of the activity of the respiratory complexes I and IV. All measurements were performed spectrophotometrically using a dual-wavelength spectrophotometer (Aminco DW 2000, SLM Instruments, Rochester, NY, USA) at 30°C.

The activity of complex I was measured at the wavelength pair of 340 nm/380 nm, $\varepsilon_{red\text{-}ox}$ = 5.5 mM^{-1} cm^{-1}. The total NADH oxidation rate was estimated by the addition of the mitochondrial probe to the reaction mix consisting of 50 mM KCl, 1 mM EDTA, 1 mM KCN, 100 µM CoQ_1, 150 µM NADH, 10 mM Tris-HCl at pH 7.4). After 2 min of recording, the rate of the rotenone-insensitive NADH oxidation was determined by the addition of 20 µM rotenone to the reaction mix. The rotenone-sensitive NADH:CoQ oxidoreductase activity was evaluated by the subtraction of the rotenone-insensitive NADH oxidation rate from the total NADH oxidation rate.

The activity of complex IV was determined at the wavelength pair of 510 nm/535 nm, $\varepsilon_{red\text{-}ox}$ = 5.9 mM^{-1} cm^{-1}. The change in the heme porphyrin-associated β-band of the cytochrome *c* absorption spectrum was monitored. The mitochondrial probe was added to the reaction mix containing 100 mM potassium phosphate buffer (pH 7.4), 0.02% laurylmaltoside, and 200 µM reduced bovine heart cytochrome *c*.

The activity of citrate synthase was evaluated by a standard method [158]. Briefly, the generation of CoA-SH in the reaction catalyzed by citrate synthase in the presence of oxaloacetate and acetyl-CoA, and its subsequent reduction of 5',5'-dithiobis-(2-nitrobenzoic acid) (DTNB) was measured spectrophotometrically at 412 nm.

5.16. Data analysis

The software used to analyze the data is specified above for each respective method. For other applications, Microsoft Office Professional 2016 and GraphPad Prism 8 were used for

calculation, and CorelDraw 2018 for image processing and depicting artistic illustrations. Unless otherwise noted, n = 3. Statistical analysis was performed with Student's t-tests, and *p*-values below 0.05 were considered significant. The data are presented as the mean ± standard deviation (S.D.).

6. RESULTS

6.1. Molecular identity of mitoBK channels in human astrocytoma and fibroblast cells

The initial step in addressing the research questions studied in this work was to confirm the presence of the mitoBK channel in the studied cellular systems and to characterize its steady-state properties. Identification of mitoBK channels can be performed using different methodological approaches. Taking into consideration the conceptual framework of this study, the presence of mitoBK channels in the chosen research models was validated by the following means:

- on the genetic level: confirmation of the expression of transcripts encoding known mitoBK channel subunits with RT-PCR and RNA sequencing;
- on the protein level: confirmation of the presence of mitoBK protein subunits in the mitochondrial fraction with SDS-PAGE followed by immunoblotting;
- on the functional level: characterization of the single-channel mitoBK activity by patch-clamp.

To obtain a snapshot of the expression of all genes reported for BK channels in the plasma membrane and IMM, the transcriptome of selected cell lines was profiled using the RNA sequencing approach (Figure 8). For this purpose, total RNA was isolated from astrocytoma and dermal fibroblast cell lines. Since the integrity of the RNA template is of paramount importance for the preparation of the cDNA libraries for high throughput sequencing, additional measures were undertaken during the RNA isolation procedure to prevent RNA degradation at any moment of sample handling, as described in chapter 5.4. As a result, the sufficiently high RNA integrity number of the samples, computed using the characteristics of the RNA electropherogram, confirmed the stability of the obtained RNA. Spectrophotometric analysis of the obtained RNA samples confirmed their purity from contamination by DNA based on the $A_{260/280}$ ratio, and from contamination by phenol and proteins based on the $A_{260/230}$ ratio.

The cDNA sequencing libraries were prepared using the 3'-method, thus primarily using mRNA out of the total isolated RNA as a template for reverse transcription. An important advantage of this method is a lack of the transcript length bias – an overrepresentation of the longer transcripts in the assigned coverage of reads that is derived by the standard cDNA

sequencing library preparation, where the mRNA template is fragmented before reverse transcription. The high-throughput sequencing was performed by HiSeq2500 (Illumina) as described in chapter 5.7 and produced at least 6.5 million 50-bp sequencing reads for each RNA sample. The obtained data were analyzed using a common RNA sequencing data analysis workflow as described in chapter 5.7.2. Following alignment of the sequencing reads to the human genome, quantification, and normalization of data, at least 9394 transcripts with ≥ 10 assigned read counts were identified in any given sample.

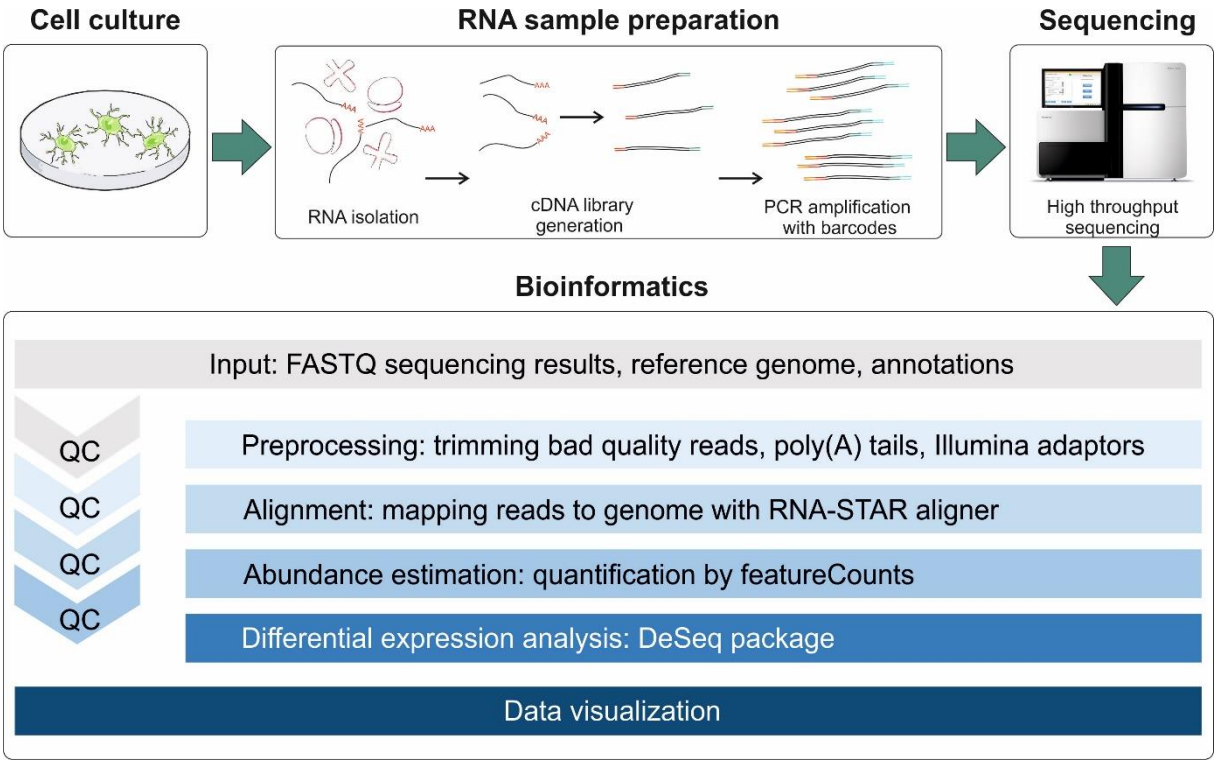

Figure 8. The typical workflow of a transcriptome analysis with RNA sequencing.

The expression of the genes encoding BK-α and BK-β4 subunits was confirmed in both human dermal fibroblasts and astrocytoma cell lines (Table 6). The presence of a few counts of transcripts of BK-β3 subunits was noted occasionally in some samples of these cell lines. A notable divergence from the previously reported data was the complete lack of detectable transcripts associated with the BK-β2 subunit in dermal fibroblasts. As expected, no transcripts encoding BK-β1 or any of the four BK-γ subunit types were identified in the transcriptomes of studied cell lines.

Table 6. Evaluation of expression of the genes encoding BK channel subunits by the RNA sequencing. The gene expression values are shown as average normalized transcript counts (n = 3). Transcript counts can appear as non-integer numbers due to the data normalization.

Gene	Associated BK protein subunit	Transcript counts in astrocytoma	Transcript counts in fibroblasts
KCNMA1	BK-α	374,39	30,39
KCNMB1	BK-β1	0	0
KCNMB2	BK-β2	0	0
KCNMB3	BK-β3	0,25	0,92
KCNMB4	BK-β4	10,67	13,32
LRRC26	BK-γ1	0	0
LRRC52	BK-γ2	0	0
LRRC55	BK-γ3	0	0
LRRC38	BK-γ4	0	0

In a study of weakly expressed genes, RNA sequencing may have certain limitations, as the very low read count values are sometimes associated with noise and can be filtered out during data normalization. Therefore, to validate the data obtained with RNA sequencing, the expression of genes encoding mitoBK subunits was studied with a qualitative RT-PCR. The isolated RNA was transcribed to cDNA using a commercially available kit under typical thermocycling conditions as described in chapter 5.5. The primer annealing temperature was optimized prior to the assay to obtain a specific and high yield of the intended product. The cDNA amplicon was then used as a template in the RT-PCR as described in chapter 5.5.

Since the standard RT-PCR setup of the initial screening has also failed to detect the expression of BK-β2 subunits previously reported for fibroblasts, the RT-PCR for detection of *KCNMB2* was designed in the "nested" configuration using two sets of primers: an outer set producing a larger product, and an inner set. Thus, weakly expressed or alternatively spliced transcripts could be detected.

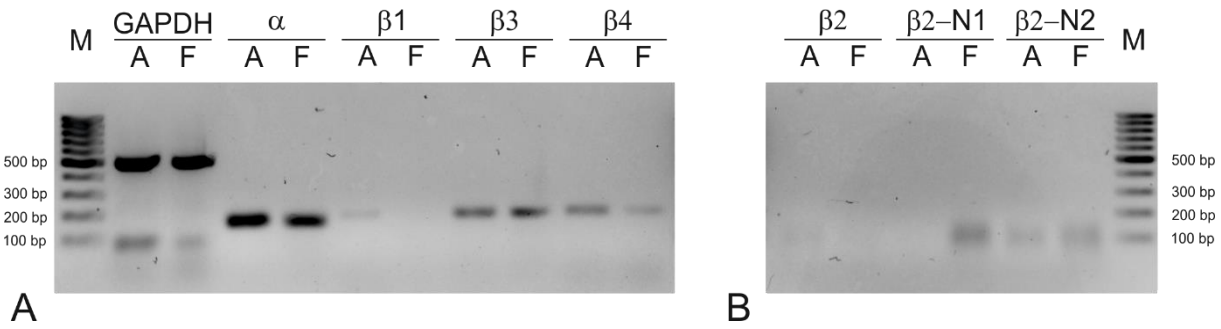

Figure 9. Analysis of the expression of BK-α and BK-β subunits in U-87 MG astrocytoma cells and human dermal fibroblasts with RT-PCR. A. Amplification products of *GAPDH*, *KCNMA1* (α), *KCNMB1* (β1), *KCNMB3* (β3), *KCNMB4* (β4) from cDNA of astrocytoma cells (A) or fibroblasts (F); (M) marker 100 bp DNA ladder. B. Amplification products of *KCNMB2* in a standard PCR configuration (β2), the first round of nested PCR configuration with outer primers (β2-N1), and the second round of nested PCR configuration with inner primers (β2-N2). The designed PCR product sizes are specified in chapter 5.6.

The RT-PCR reaction has detected the expression of *KCNMA1* in both cell types (Figure 9). The observed bands were singular, corresponding to the predicted PCR product size, and their signal was sharp and strong. The analysis of expression of auxiliary BK-β subunits in astrocytoma cells confirmed expression of *KCNMB3* and *KCNMB4*, and a faint band demonstrating few transcripts of *KCNMB1* was present. In fibroblasts, the expression of *KCNMB3* and *KCNMB4* was confirmed. However, the designed product of *KCNMB2* of appropriate size was not produced by RT-PCR reactions in regular or nested configurations in either cell type (the blurred bands sized about 100 bp do not correspond to the intended product size and are likely an unspecific byproduct of the PCR). Thus, the data obtained with the RNA sequencing study were in alignment with the findings of RT-PCR.

Next, to identify whether a fraction of BK channel proteins is targeted to mitochondria, their presence in the mitochondrial isolation of astrocytoma, control and COX8A-deficient fibroblasts was evaluated by a Western blot analysis (Figure 10). Mitochondrial isolation was performed according to the protocol described in chapter 5.8. Proteins were separated in SDS-PAGE gels under reducing conditions and subsequently blotted onto the PVDF membrane as described in chapter 5.9. The membrane was then subsequently treated in three solutions, with alternating washing steps in between, according to the procedure covered in detail in chapter 5.9. Briefly, a blocking solution was applied firstly to minimize noise and non-specific antibody binding; next, a solution containing primary antibodies raised against proteins of interest; finally, a solution containing appropriate secondary horseradish peroxidase (HRP)-conjugated antibodies raised against the host species of the primary antibodies. To visualize the signal, a

reagent containing chemiluminescent HRP substrate was applied to the membrane, and the blot signal was captured using either analog (X-ray film) or digital (camera-based charge-coupled device) technologies.

Western blot analysis identified the presence of the pore-forming BK-α subunit, as well as the auxiliary BK-β3 and BK-β4 subunits in the mitochondrial fraction of astrocytoma cells and human dermal fibroblasts (Figure 10). In Western blot analysis, the monoclonal antibody raised against the cytoplasmic domain of the BK-α subunit has detected two bands: a predicted band migrating at approximately 130 kDa, and a band migrating below 55 kDa. Interestingly, while most *KCNMA1* protein-coding transcripts encode 100-130 kDa sized peptides, a splice variant KCNMA1-226 listed in the Ensembl database encodes a smaller 52 kDa peptide that can be recognized by this antibody and contains three transmembrane domains. However, because the composition of this protein band has yet to be validated, further immunoblotting studies concentrated on observation of the bands that match the canonical full-sized BK-α protein.

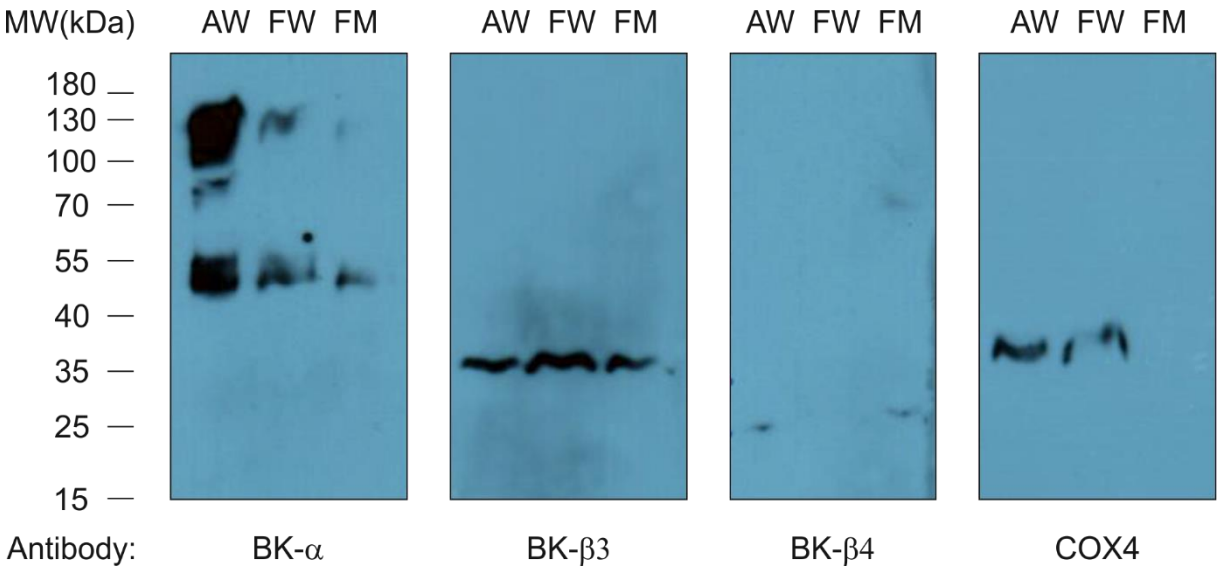

Figure 10. SDS-PAGE and Western blot analysis of expression of mitoBK protein subunits in a mitochondrial fraction in U-87 MG astrocytoma cells and human dermal fibroblasts. Each lane contains 50 μg of protein of mitochondrial preparation of astrocytoma cells (AW), control fibroblasts (FW), or fibroblasts with a mutation in *COX8A* (FM).

Thus, the analysis of gene expression in the astrocytoma cell line and dermal fibroblasts confirmed the expression of pore-forming BK-α subunits, as well as a small amount of auxiliary BK-β3 and BK-β4 subunits. Furthermore, immunochemical analysis has shown that a fraction

of translated BK channel proteins is targeted to the mitochondria of these cells. Notably, the protein amount of the mitoBK-α subunits was higher in the mitochondria of the astrocytoma cells than in the dermal fibroblasts, corresponding to the higher expression of *KCNMA1* in this cell type. Therefore, the presence of mitoBK channels in the studied cellular models was validated.

6.2. Single-channel electrophysiological properties of mitoBK channels in isolated mitochondria of astrocytoma cells

After the molecular presence of mitoBK channels in the studied models was confirmed, its electrical activity was examined by patch clamping the IMM. This method is regarded as a "golden standard" for studying single-molecule biophysical properties of ion channels. Since it allows for precise control over the solute environment of a patch of membrane containing ion channels, it is a perfect tool for characterizing their functional modulation by various compounds.

Mitochondria isolated from human astrocytoma U-87 MG cells were used as a study model in the patch-clamp experiments. The primary reason for using this cellular model is that the mitoBK channels are more abundant in the IMM of astrocytoma cells than in the fibroblasts, which increases the chances of finding this channel in a given patch of membrane. Furthermore, mitochondrial isolation from astrocytoma is relatively efficient, and a gigaseal between the IMM and the patch pipette glass can be successfully formed in a reasonable number of trials.

The procedure of mitochondrial patch-clamp is well-established, and its schematic depiction is shown in Figure 11. The access to the IMM is achieved by disruption of the OMM by swelling through a sequential treatment of an aliquot of isolated mitochondria in hypotonic and hypertonic solutions as described in chapter 5.11. This procedure leaves a characteristic "cap"- a remnant of the OMM attached to the mitoplast. The presence of these "caps", as well as the size and transparency of the created vesicles, were the criteria for distinguishing mitoplasts from cellular debris. The purity of the mitochondrial fraction selected by this approach has been previously confirmed by a variety of techniques, including single-mitoplast PCR, which confirms the presence of mitochondrial DNA within the patched vesicles [71,159].

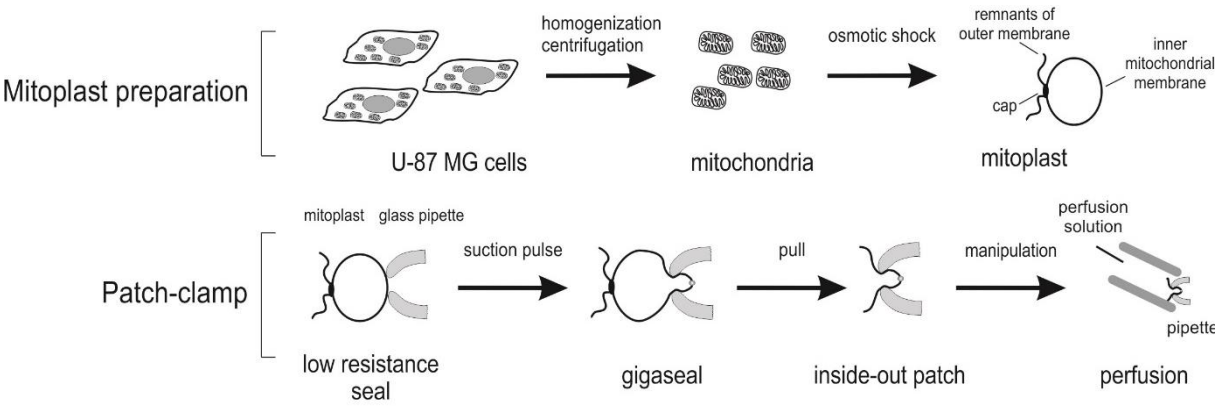

Figure 11. A schematic depiction of patch-clamp of inner mitochondrial membrane.

Patch-clamp experiments confirmed the mitoBK activity by its distinct biophysical characteristics: dual regulation by voltage and Ca^{2+}, conductance, current-voltage relationship, and a distinct pattern of BK channel kinetics (Figure 12). The typical mitoBK channel conductance, calculated as a slope of the I/V curve, was 289 ± 8 pS.

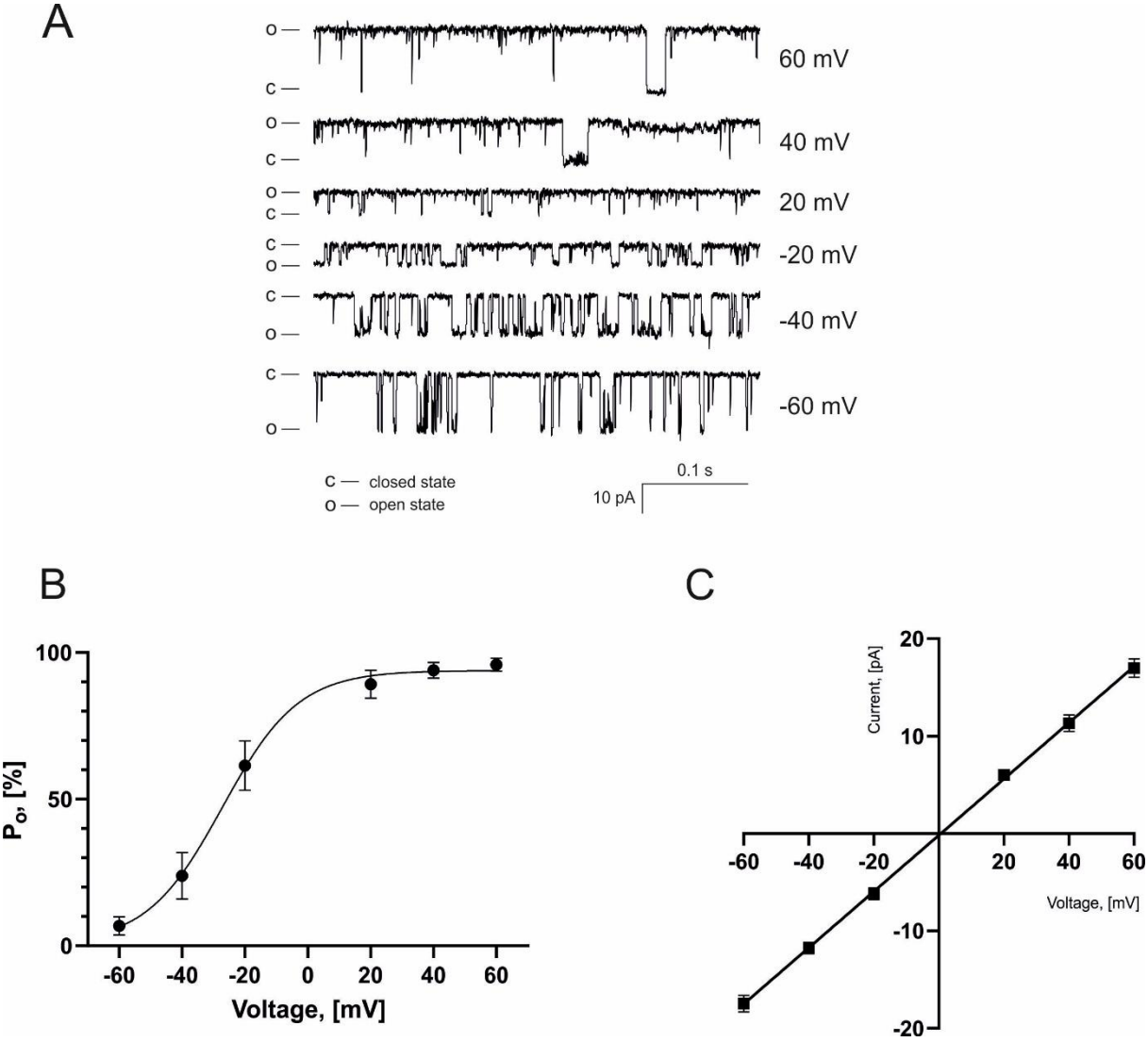

Figure 12. Biophysical properties of mitoBK channel of astrocytoma mitochondria in the symmetrical 150/150 mM KCl isotonic solution containing 100 µM Ca^{2+}. (A) A typical recoding of single-channel mitoBK channel activity is shown. (B) Voltage dependence of mitoBK open probability (Po). (C) Current-voltage relationship of mitoBK channels.

Since the patches of the IMM were prepared in the inside-out patch-clamp configuration, the matrix side of the IMM was exposed to the perfusion bath containing experimental solutions. The C-terminal part of the channel, which contains the Ca^{2+} binding regions, was facing the

matrix compartment of mitochondria, as evidenced by the decrease of mitoBK channel activity in response to a change in Ca^{2+} concentration in the perfusion bath (Figure 13A). Regulation of channel activity by the established mitoBK channel modulators further validated their identity. Thus, the application of a mitoBK opener CGS7184 activated the channels, while the application of a mitoBK blocker paxilline inhibited channel activity (Figure 13B).

In conclusion, the initial assessment has confirmed the functional activity of the mitoBK channel in the IMM of the astrocytoma cells. The channels had the characteristic biophysical activity profile and dual regulation by voltage and calcium ions. The activity of mitoBK channels was modulated by paxilline and CGS7184 in the perfusion solutions.

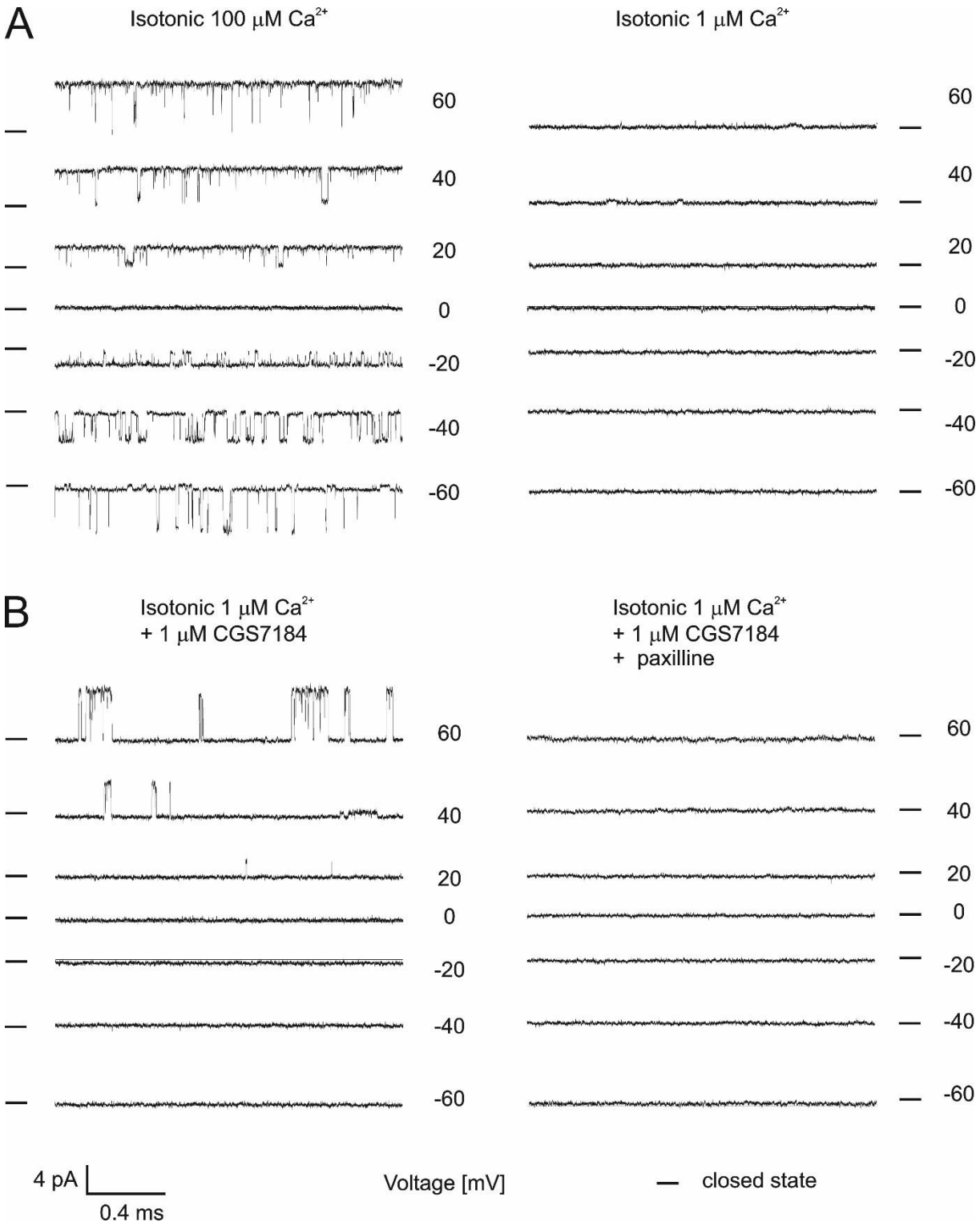

Figure 13. Modulation of mitoBK channel activity. (A) Ca^{2+}-dependent regulation of mitoBK channel activity. (B) Pharmacological modulation of mitoBK channel activity by 1 μM mitoBK activator CGS7184 and 1 μM inhibitor paxilline. In a representative recording in a patch-clamp experiment, the perfusion solutions are applied to the matrix side of the IMM patch.

6.3. Analysis of interaction of mitoBK channel with the respiratory chain in the model of mtDNA-depleted astrocytoma cells

One of the questions addressed in this study was how the mitoBK channel interacts with the respiratory chain proteins in the IMM. A cellular model line bereft of mtDNA would be a particularly valuable research tool in this investigation. Firstly, it would yield insight into whether mitochondrial retrograde signaling pathways triggered by mtDNA depletion impact the BK channels in mitochondria and cell membrane. Secondly, mtDNA-encoded OXPHOS subunits are essential for the electron flow through the ETC, and in their absence, the fully functional ETC complexes I, III, and IV cannot be assembled. Thus, by depleting mtDNA, a useful cellular model can be established for the study of the multiprotein complexes formed between the mitoBK channels and the respiratory chain proteins.

6.3.1. Generation of mtDNA-depleted astrocytoma cell line

To accomplish the generation of the mtDNA-void cells, human astrocytoma U-87 MG cell line was chosen as a study model, considering its metabolic profile with a proclivity to aerobic glycolysis. Namely, to provide metabolic support to neurons, normal astrocytes have a high capacity for surplus glycolytic lactate synthesis, alongside the active respiratory generation of ATP (a Pasteur effect) [160]. Malignantly transformed astrocytes, such as U-87 MG astrocytoma tumor cells, additionally favor aerobic glycolytic pathways under normoxic conditions (a Warburg effect). As a consequence, this cell type was anticipated to have a higher probability of surviving the mtDNA loss, what might have turned fatal for other cell types.

Treatment with a non-hydrolyzable nucleoside analog 2′,3′-dideoxycytidine (ddC), which is characterized as a high-affinity inhibitor of the mitochondrial DNA polymerase-γ (POLG), was selected as a method to induce mtDNA deficiency in astrocytoma cells [161]. The cell culture medium was supplemented with uridine as a precursor for pyrimidine salvage synthesis. Thus, although *in vitro* treatment with 20 µM ddC impaired the growth rate of U-87 MG cells, their viability was maintained. However, it is worth noting that an attempt of increasing the concentration of ddC in the growth medium to 50 µM had a sharply negative effect on the cell survival, likely due to the low-affinity binding of ddC to the nuclear DNA polymerases.

6.3.1.1. Confocal microscopy imaging of the mitochondrial network of astrocytoma cells upon mtDNA depletion

To visualize the effect of the ddC treatment on the morphology of U-87 MG cells and their mitochondrial network, confocal microscopy imaging was employed. The cells were fixed in a PFA solution, permeabilized in a saponin-containing solution, and immunostained with a primary antibody raised against VDAC, and Alexa Fluor 633-conjugated secondary antibody. The protocol of sample preparation and immunostaining is described in detail in chapter 5.10.

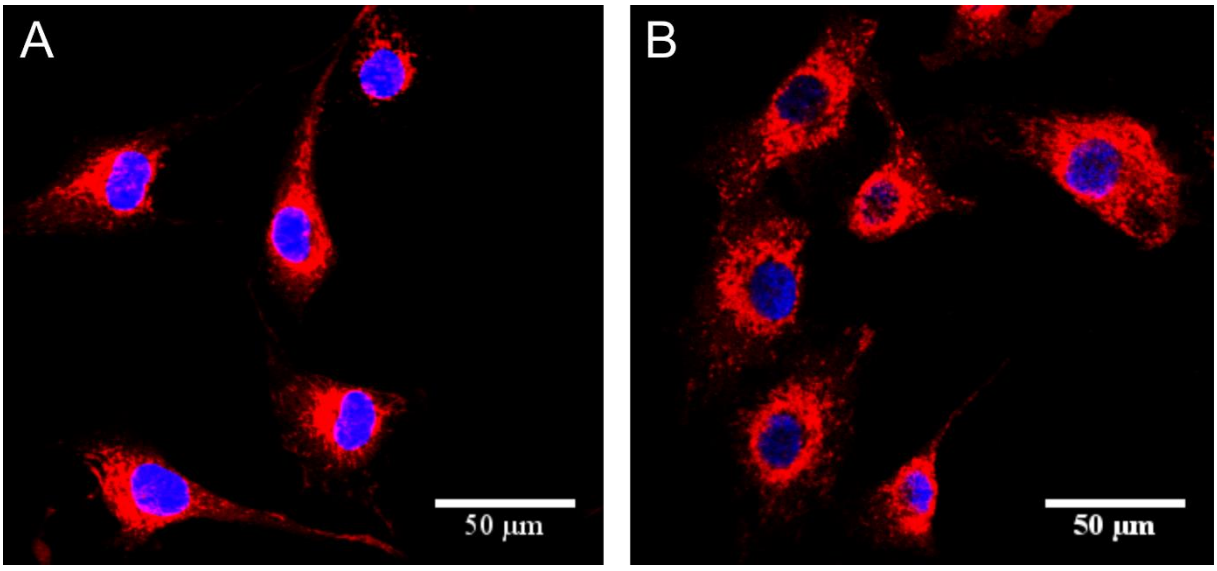

Figure 14. Mitochondrial network in the astrocytoma WT (A) and ddC-treated cells (B) visualized by confocal microscopy. Nuclei were visualized with DAPI (blue), and mitochondria were visualized with VDAC (red).

After three weeks of treatment with 20 µM ddC, a pronounced change in the size and shape of the cells was observed (Figure 14). In comparison to the characteristic polygonal appearance of U-87 MG cells, the ddC-treated cells had a larger surface and a more rounded and irregular morphology. Immunofluorescence staining using antibodies against VDAC revealed that mtDNA-depleted cells retain mitochondrial structures, however, the mitochondrial network appears to be more fragmented.

6.3.1.2. Determination of cellular respiration of ddC-treated astrocytoma cells

To determine whether the depletion of mtDNA has been achieved, several tests were performed in this study:

- on the functional level: respiration of cells was evaluated by oxygraphy;
- on the genetic level: the transcriptome profile of ddC-treated cells was studied with a focus on mtDNA-encoded genes;
- on the protein level: Western blot analysis was performed to identify the absence of mtDNA-encoded ETC subunits.

The progress of mtDNA depletion can be followed indirectly through the functional bioenergetics analysis. Since the key components of the OXPHOS complexes I, III, IV and V are compromised in mtDNA-depleted cells, the oxygen consumption rate by their mitochondria is significantly decreased. Thus, to identify the depletion of mtDNA in U-87 MG astrocytoma cells, cellular respiration was measured with the Oroboros oxygraph, as described in chapter 5.12.

The basal respiration was studied in the cell culture medium containing glucose, pyruvate, and glutamine as metabolic energy substrates. After reaching stable basal respiration, sequential 1 μM additions of protonophore CCCP were used to induce uncoupling. In the WT astrocytoma cells, the additions of CCCP led to an increase in cellular respiration in a dose-dependent manner (Figure 15). In the astrocytoma cells treated with ddC for 3 weeks, a small level of basal oxygen consumption was observed, possibly due to the activity of non-mitochondrial oxygenases. However, the additions of CCCP did not display any significant effect on the oxygen consumption rates in the ddC-treated cells, what indicated that respiration was virtually abolished and mtDNA depletion occurred.

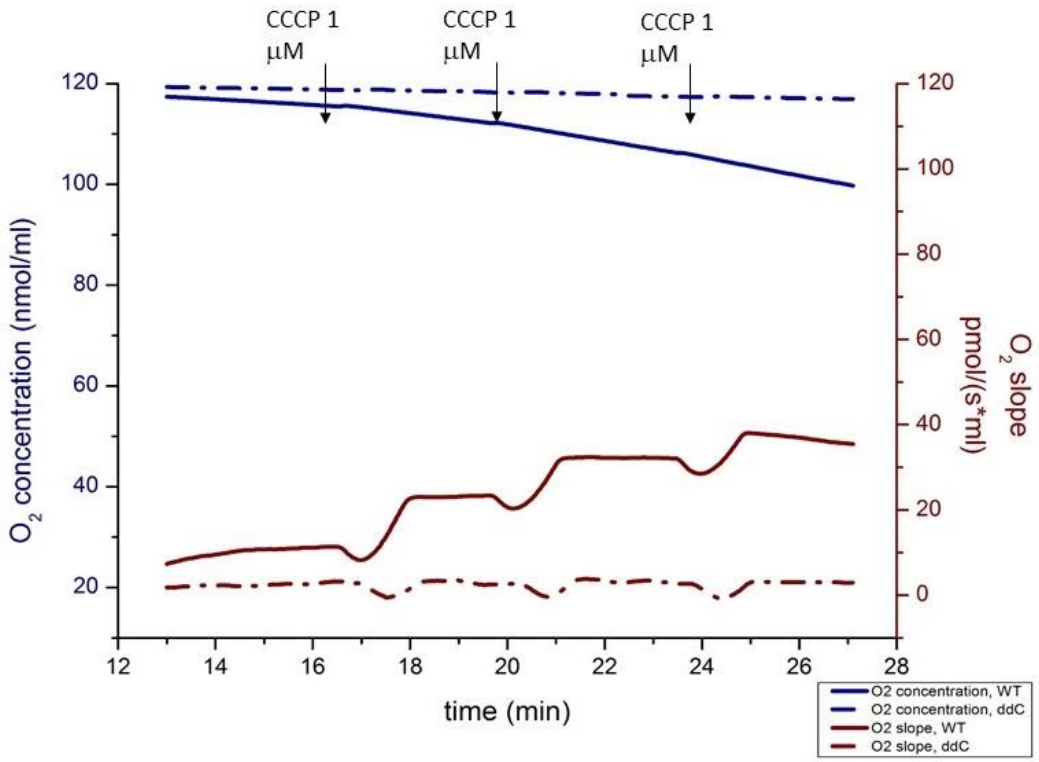

Figure 15. Treatment of U-87 MG astrocytoma cells with ddC abolishes cellular respiration. Oxygraphic evaluation of cellular respiration of one million U-87 MG astrocytoma cells: WT (solid lines) and upon treatment with ddC (dash-dotted lines); in blue, O_2 concentration in nmol/ml; in brown, O_2 slope in pmol/(s*ml). Arrows indicate the addition of 1 µM CCCP to the oxygraph chamber.

6.3.1.3. Characterization of the expression of the mitochondrial genes in mtDNA depleted line with RNA sequencing

To confirm depletion of mtDNA, the change in the expression of mtDNA-encoded genes in the WT and ddC-treated astrocytoma cells was evaluated by RNA sequencing data.

Several statistical tools are available for the analysis of the differential gene expression of the RNA sequencing data, with R/Bioconductor DESeq2 and EdgeR being among the most widely used ones [162]. The normalization methods in both tools are based on the null hypothesis that no differential expression occurs for most genes. The statistical model of EdgeR calculates a general dispersion parameter using the Cox-Reid profile likelihood and then evaluates per-gene dispersion using the Bayesian model [163]. DESeq2 employs a slightly different approach, where individual values of gene dispersion are first estimated before fitting them to a model. Although the results obtained by these two statistical strategies are usually well-aligned, the normalization method of DESeq2 is more robust to the low expressed genes, since to increase the statistical

power of EdgeR analysis, it is commonly practiced to apply filtering for the genes with the low expression values that are considered to have low biological relevance.

A first look at the results of the differential gene expression analysis performed with both EdgeR and DESeq2 shows that about 7% of differentially expressed transcripts were found by the EdgeR algorithm, and about 5% were identified as such by DESeq2 (Table 7).

Table 7. Estimation of the number of differentially expressed genes in the U-87 MG astrocytoma ddC-treated cells versus astrocytoma WT cells using EdgeR or DESeq2.

Statistical tool used for analysis	Upregulated transcripts	Not differentially expressed	Downregulated transcripts
EdgeR	422	12885	476
DESeq2	413	15788	422

Notably, both approaches produce the mean-difference (MD) plots of the differential gene expression in the ddC-treated U-87 MG astrocytoma cells, which in the bottom right section reveal a cluster of the highly expressed genes that are strongly downregulated (Figure 16). These genes denote the decreased transcription of mitochondrial genes following the mtDNA depletion.

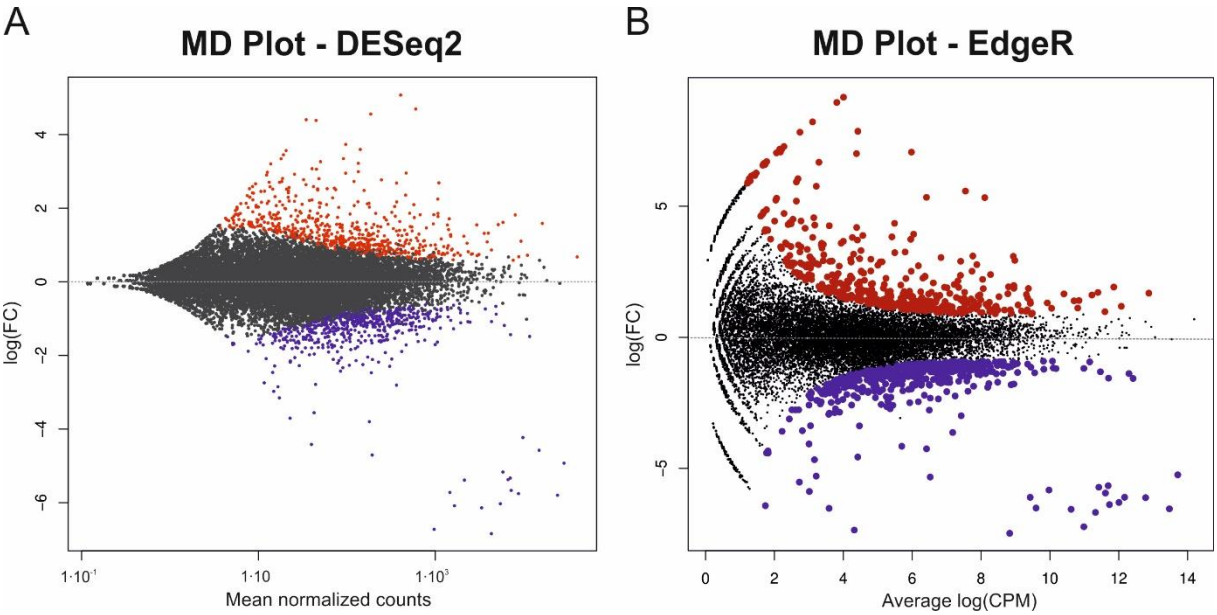

Figure 16. The MD plots of differential gene expression in the ddC-treated U-87 MG astrocytoma cells. (A) The analysis performed with DESeq2 includes all genes with non-zero mapped read counts. (B) Using EdgeR analysis, the total gene transcript reads are filtered to exclude genes with low expression (defined as ≤ 0.5 counts per million in at least two samples). For both methods, the false discovery rate is defined as < 0.05. Each identified sequence is denoted as a dot, the upregulated transcripts are shown in red, and the downregulated ones are in blue. Log(FC), the binary logarithm of fold change; $\log_2$(CPM), the binary logarithm of counts per million.

While the key findings were confirmed with both methods, the rest of this work will refer only to the results of the differential gene expression analysis conducted with DESeq2.

The read counts of the transcripts of 13 mitochondrial protein-encoding genes were identified among the most downregulated genes in the ddC-treated U-87 MG astrocytoma cells (Figure 17). The evaluated *p*-values of the differentially expressed mitochondrial-encoded genes were distributed in the range between $p = 2 \cdot 10^{-13}$ and $p = 2 \cdot 10^{-155}$, and $\log_2$(FC) values – in the range between $\log_2$(FC) = - 4.22 and $\log_2$(FC) = - 6.83 (for *COX2* and *ND1*, respectively).

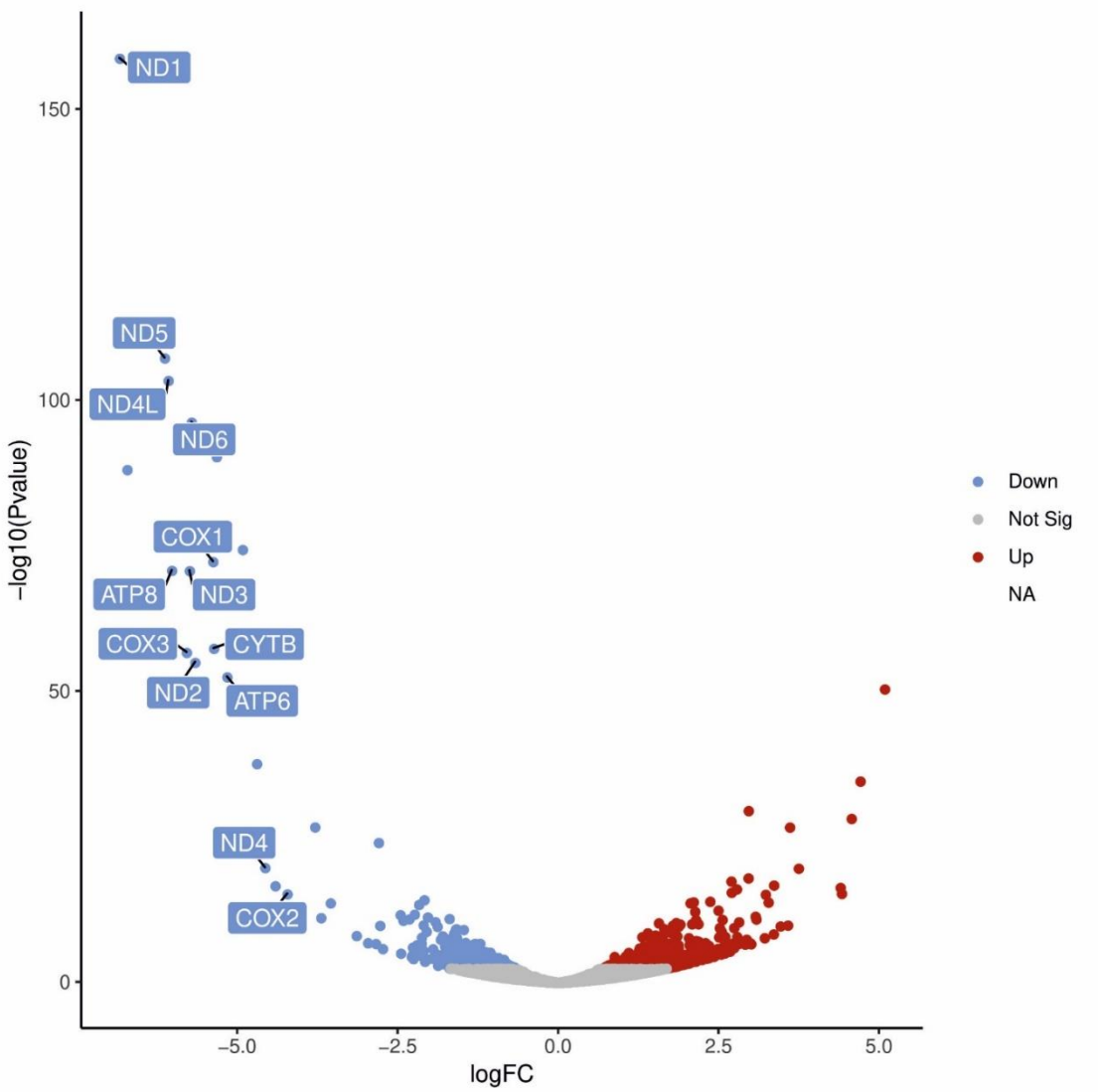

Figure 17. Expression of mtDNA-encoded genes is significantly downregulated in the ddC-treated U-87 MG astrocytoma cells. The volcano plot graphically identifies differential expression of genes: the value of $-\log_{10}$(p-value) is plotted on the y-axis against the $\log_2$(fold change) on the x-axis. The change in value for each assigned gene sequence is depicted by one point. The upregulated transcripts are labeled in red, downregulated – in blue, and the transcripts without a statistically significant change in expression ($p > 0.05$) – in grey.

Therefore, differential gene expression analysis confirmed mtDNA depletion on the level of the decrease in mtDNA expression in the ddC-treated astrocytoma cells.

6.3.2. Analysis of complexes of mitoBK channels with the respiratory chain proteins in astrocytoma cells

The previous studies have shown functional interaction of the mitoBK channels with the electron transport chain. The physical interaction of the mitoBK-β4 subunit with the cytochrome *c* oxidase was implicated in this phenomenon [104]. However, relatively little is understood about the interaction of the pore-forming subunit mitoBK-α with the COX within the respiratory chain supercomplexes.

A number of recent studies examined the molecular mechanisms of mitochondrial retrograde signaling. Yet, no attempts have been made to investigate the potential involvement of the potassium channels, and in particular, of the mitochondrial potassium channels as regulators of ion fluxes in this organelle.

To address these gaps in the research, the interaction of the mitoBK-α pore-forming subunit with the ETC was investigated, taking advantage of the developed mtDNA-depleted U-87 MG astrocytoma cell model.

6.3.2.1. Assessment of protein complexes of mitoBK channels with the respiratory chain in astrocytoma cells

Identification and characterization of multiprotein complexes are immensely important in gaining a greater understanding of protein-protein interaction networks. By allowing the separation of protein complexes under non-denaturing conditions, blue-native PAGE (BN-PAGE) became a versatile tool to study membrane multiprotein complexes in their native conformation in different systems. This method was used for the evaluation of the steady-state protein complexes between mitoBK channels and the ETC complexes in the mitochondrial isolation from human astrocytoma U-87 MG cell line.

In the initial assay, two approaches for mitochondrial preparation were evaluated for the downstream application in the separation of mitochondrial proteins: a standard differential centrifugation-based mitochondrial isolation method was compared to the column-based magnetic labeling method with anti-TOM22 beads, as described in chapter 5.8. The mitochondrial sample preparation was performed as reviewed in chapter 5.9. Due to its preservation of the native stoichiometry of the respiratory chain SC, a non-ionic mild detergent

digitonin was selected for solubilization of the membrane protein complexes. The protein of mitochondrial samples obtained using these two isolation approaches from the astrocytoma cells were separated by the BN-PAGE and identified by subsequent Western blotting (Figure 18).

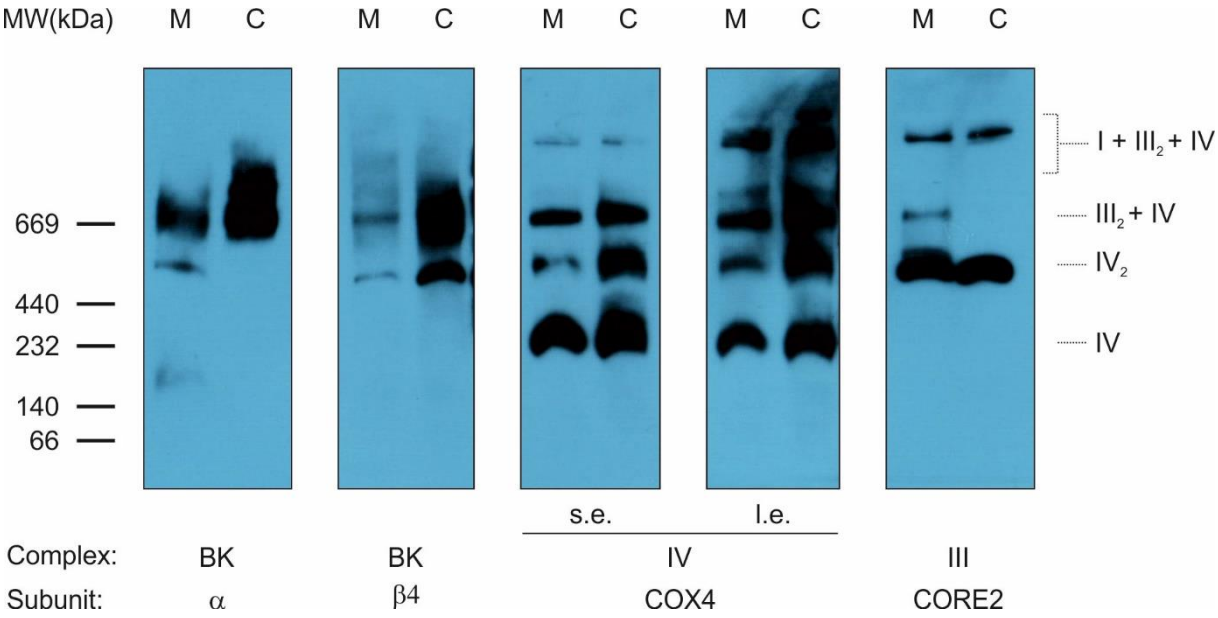

Figure 18. Comparison of the protein complexes of human astrocytoma U-87 MG mitochondria obtained with the different mitochondrial isolation methods. The mitochondrial preparations (100 µg protein/lane) of the astrocytoma WT cells were solubilized with 1% digitonin and resolved by BN-PAGE followed by Western blotting. M – magnetic beads-based isolation, C – "classical" differential centrifugation-based method. On the right, the protein complexes formed with COX: IV – COX monomer, IV_2 – COX dimer, III_2 + IV – dimer of complex III and COX, I + III_2 + IV – the respirasome.

The strong signals of mitoBK-α and mitoBK-β4 channel subunits were found in mitochondrial preparations from the astrocytoma WT cells obtained by both methods. A band migrating at the molecular weight, which corresponded to the tetramer of mitoBK-α subunits associated with mitoBK-β4, was detected in both preparations. However, the mitochondrial isolation obtained with the magnetic beads-based method had two more apparent signals of the mitoBK-α subunit: migrating at the MW about 440 kDa, and at the size slightly larger than a mitoBK-α monomer – about 130 kDa. Both signals of complexes formed by the mitoBK-α subunit corresponded to the signals detected by an antibody against the mitoBK-β4 subunit.

Unfortunately, it became apparent that the magnetic beads-based mitochondrial isolation had several crucial drawbacks, which made this method unsuitable for further BN-PAGE studies.

Firstly, the column separation was performed at room temperature, what could affect the stability of the protein complexes. Secondly, the obtained mitochondrial solution contained residual magnetic beads, which interfered with the colorimetric methods of protein quantification and led to an incorrect estimation of the protein amount. A treatment with protease to remove the beads would risk damaging the protein complexes in the sample. Therefore, further studies were limited to using the "classical" isolation method based on the differential centrifugation.

To address one of the research questions posed in this work, the interaction of the mitoBK channel subunits with the ETC proteins was evaluated in two models: mitochondria isolated from the WT astrocytoma, and mitochondria of mtDNA-depleted astrocytoma cells lacking crucial subunits of respiratory chain complexes. The protein complexes formed by the mitoBK-α, mitoBK-β4, and COX4 were resolved with BN-PAGE and immunoblotted (Figure 19).

In the mitochondrial preparation of the WT cells, the mitoBK-α signal was distributed between three protein complexes. Firstly, due to the high protein amount per lane, it was possible to visualize the co-migration of the high molecular weight complexes of mitoBK-α subunit with the COX as a part of respirasomes, which were migrating above 1 MDa. Yet, this protein complex was the least abundant form among the three mitoBK-α-containing fractions. The largest amount of BK-α was present in a protein complex co-migrating with the BK-β4 subunit at the molecular weight corresponding to the fully assembled channel (consisting of a tetramer of mitoBK-α subunits associated 1:1 with mitoBK-β4 subunits - about 580 kDa) and higher. The smeared appearance of this band on the Western blot was also persistent after solubilization of mitochondrial preparation with another detergent - n-Dodecyl β-D-maltoside (not shown). Considering that the mitoBK channel was reported to interact with multiple mitochondrial proteins [82], this signal can actually contain several populations of the channels with different protein partners. The third fraction of mitoBK in the WT cells was co-migrating with the BK-β4 subunit above 440 kDa below the expected size of the fully assembled mitoBK channel, and co-localized with a COX dimer.

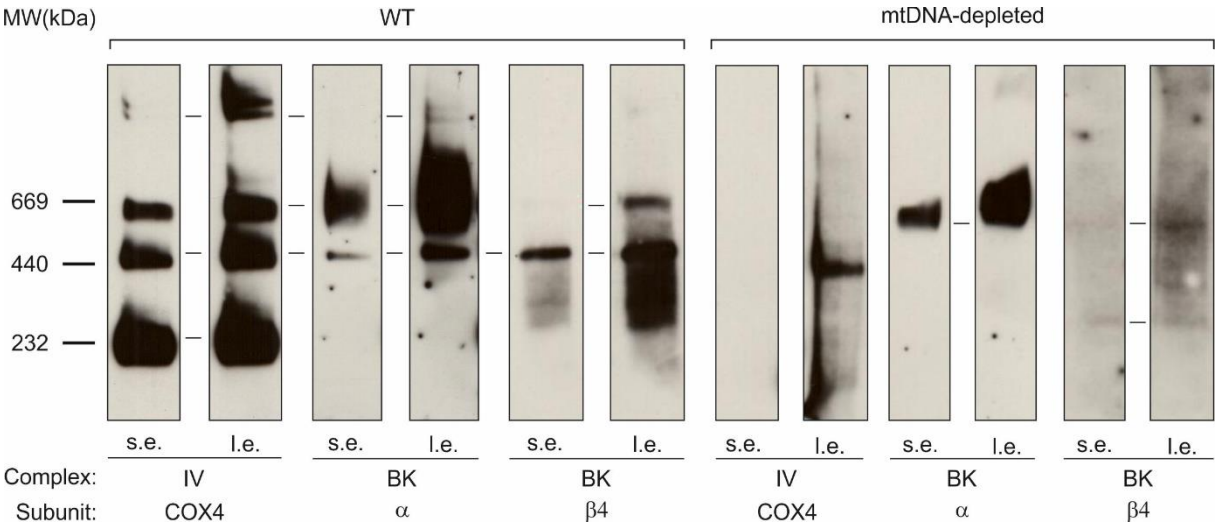

Figure 19. MitoBK channel interacts with COX and is a part of the RC supercomplexes. The mitochondrial preparations (150 µg protein/lane) of the astrocytoma WT and mtDNA-depleted cells were solubilized with 1% digitonin and resolved by BN-PAGE followed by Western blotting. S.e. – short exposure, l.e. – long exposure.

As predicted, the mtDNA-depleted cells were deficient in COX complexes, and the residual COX4 signal was contained in one protein complex not characteristic of any typical COX assemblies in the WT mitochondria. Notably, the comparative analysis showed that mtDNA depletion affects both the abundance and the composition of the protein complexes formed by the mitoBK-α and mitoBK-β4. Specifically, only a protein complex of the size corresponding to the tetramer of BK-α subunits associated with the BK-β subunits was visualized. The amount of this protein complex was markedly lower than in the WT cells. The other two complexes of the mitoBK-α subunit co-migrating with the COX dimer and COX in the respirasomes were absent. Therefore, these results indicate that the pore-forming mitoBK-α subunit interacts with the COX and can be a part of the respiratory chain supercomplexes in astrocytoma mitochondria.

6.3.2.2. Determination of mitoBK protein amount upon mtDNA depletion of astrocytoma cells

Several potential reasons could underlie the observed decrease in the mitoBK-α protein amount in the mitochondrial preparation of ddC-treated cells. Since there are indications that mitoBK-α follows the mitochondrial import pathway through TOM/TIM complexes, the observed decreased protein amount could be induced by the impairments in the mitochondrial transport of nuclear-encoded proteins.

Thus, the levels of complexes formed by other nuclear-encoded proteins in the IMM were visualized in the WT and ddC-treated cells by BN-PAGE/Western blotting (Figure 20).

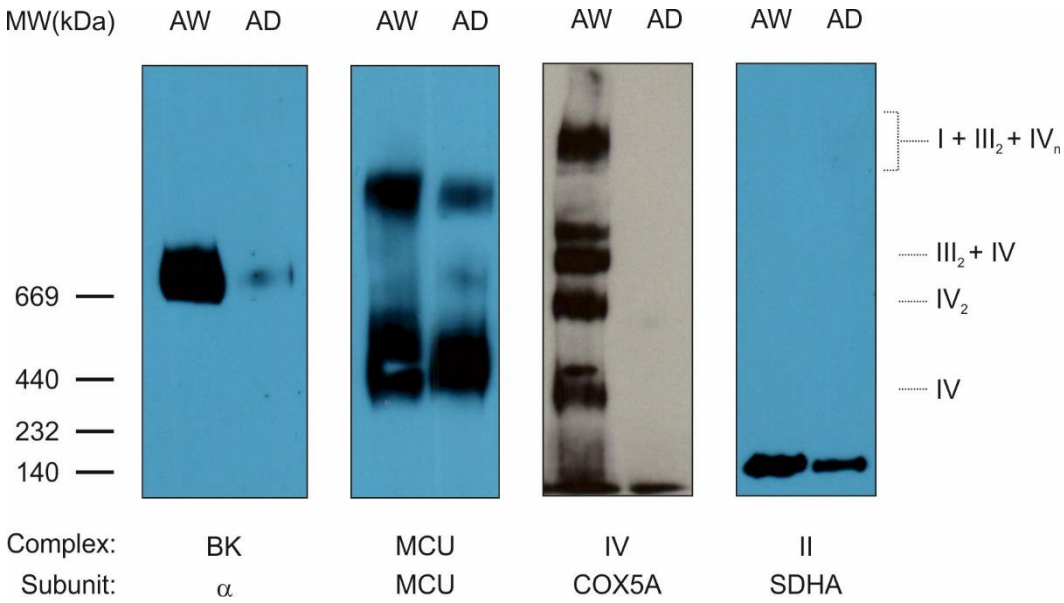

Figure 20. Downregulation of the evaluated IMM protein complexes is observed in the ddC-treated cells. The mitochondrial preparations (100 µg protein/lane) of the astrocytoma WT (AW) and mtDNA-depleted cells (AD) were solubilized with 1% digitonin and resolved by BN-PAGE followed by Western blotting.

The amounts of all evaluated IMM proteins were decreased in the mtDNA-depleted cells, which may indicate the impaired protein import due to the loss of the membrane potential generated by ETC complexes. Nevertheless, the magnitude of the downregulation was different for each of the tested proteins. The decrease in the total abundance of the mitoBK-α signal was more strongly pronounced than a decrease in another ion channel of the IMM – the mitochondrial calcium uniporter (MCU). Similarly, the total amount of the protein complexes containing subunit SDHA of the complex II was decreased to a smaller extent than the complexes with subunit COX5A of complex IV, which were likely misassembled and subjected to the degradation due to the lack of the essential mtDNA-encoded components.

While BN-PAGE is a sensitive method for the study of protein-protein interactions, the SDS-PAGE is more suitable for the comparative analysis of the total protein levels by enhancing epitope availability to the antibodies and decreasing the interference of lipids. Thus, to verify the decrease in the protein amount of the mitoBK-α subunit, the SDS-PAGE/Western blotting was performed (Figure 21).

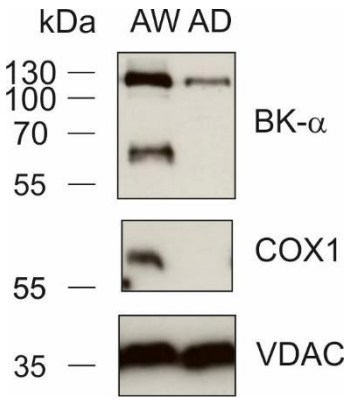

Figure 21. The total BK-α amount in the mitochondria of the mtDNA-depleted astrocytoma cells is decreased. SDS-PAGE followed by immunoblotting of the mitochondrial preparation of the astrocytoma WT (AW) and mtDNA-depleted cells (AD).

The results of the study confirmed the decrease in the total amount of the mitoBK-α protein in the mitochondria of the mtDNA-treated astrocytoma cells.

6.3.2.3. Transcriptome profiling in mtDNA-depleted astrocytoma cells with high-throughput RNA sequencing

Another molecular mechanism underlying an observed downregulation in the mitoBK-α protein amount after the mtDNA depletion can be a decrease in the *KCNMA1* transcription. To investigate whether the decrease in the amount of the mitoBK-α protein occurs on the level of gene expression, the transcriptome profiling of the astrocytoma WT and mtDNA-depleted cells was performed with RNA sequencing.

RNA sequencing detected the expression of three genes encoding BK channel subunits in the ddC-treated cells: *KCNMA1*, *KCNMB3*, and *KCNMB4* (Figure 22). The expression of the *KCNMA1* encoding mitoBK-α subunit was decreased and considered statistically significant: $\log_2(FC) = -1{,}30$; $p < 2 \cdot 10^{-4}$. The mean amount of normalized *KCNMB4* read counts appeared higher in the ddC-treated cells, but was not considered statistically significant: $\log_2(FC) = 1{,}10$; $p = 0.15$. The expression of *KCNMB3* was identified in 2 samples of ddC-treated cells compared to 1 sample of the WT cells and was not evaluated.

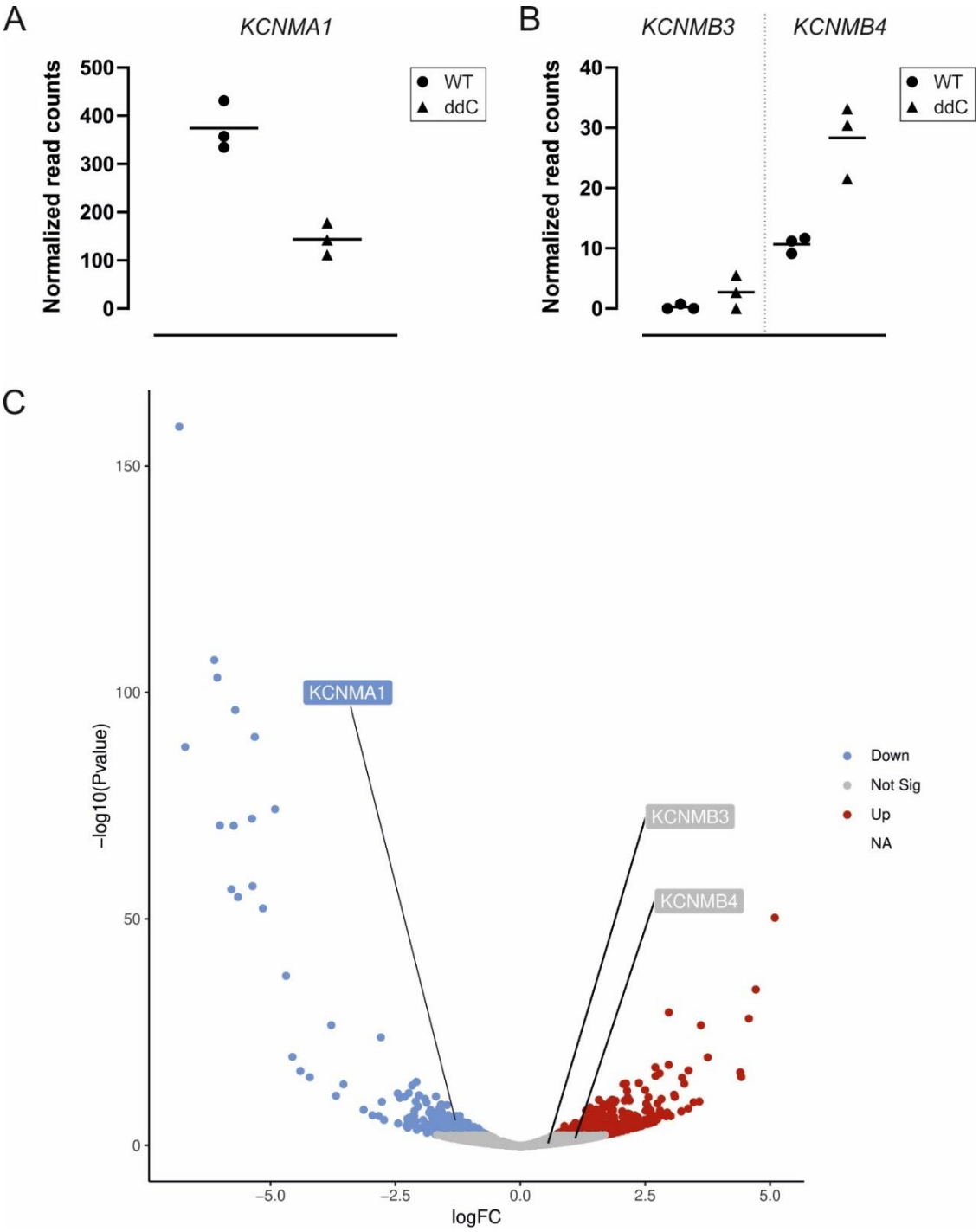

Figure 22. Expression of *KCNMA1* is significantly downregulated in the ddC-treated U-87 MG astrocytoma cells. The volcano plot graphically identifies differential expression of genes: the value of $-\log_{10}$(p-value) is plotted on the y-axis against the $\log_2$(fold change) on the x-axis. The change in value for each assigned gene sequence is depicted by one point. The upregulated transcripts are labeled in red, downregulated – in blue, and the transcripts without a statistically significant change in expression ($p > 0.05$) – in grey.

To validate the results of *KCNMA1* decrease obtained with RNA sequencing, a real-time reverse-transcription polymerase chain reaction (qRT-PCR) was performed as described in chapter 5.5. The decrease in the expression of *KCNMA1* was confirmed in a qRT-PCR assay with *GAPDH* as a reference gene (Figure 23).

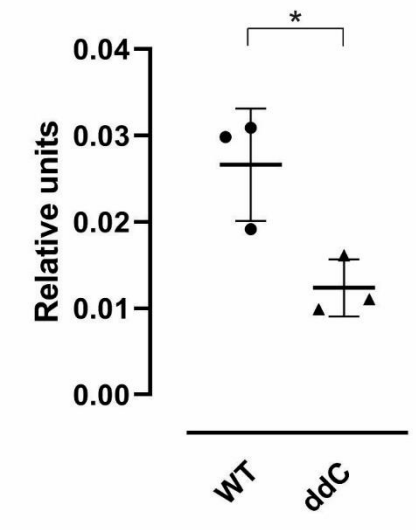

Figure 23. A decrease in *KCNMA1* expression in ddC-treated astrocytoma cells is confirmed by qRT-PCR. The expression level of *KCNMA1* in relation to *GAPDH* is shown in astrocytoma cells (n = 3). (*) $p < 0.05$

Next, to determine whether the decrease in *KCNMA1* expression could be a part of the systemic downregulation of gene expression by transcriptional factors, the activation of mitochondrial retrograde signaling pathways, and expression of the downstream target genes of known or suggested regulators of *KCNMA1* transcription were characterized by RNA sequencing.

Mitochondrial deficiency can trigger several signaling pathways to evoke a transcriptional response from the nucleus. The key mitochondrial retrograde signaling pathways are the mitochondrial integrated stress response (ISR) and the mitochondrial unfolded protein response (mtUPR). To identify the signaling pathways invoked by the mtDNA depletion in the astrocytoma cells, the expression of the master transcriptional controllers in the ISR and mtUPR and their primary targets were evaluated.

The regulatory response of the ISR pathway induces a global translational downregulation and a selective upregulation of transcription favoring the stress response genes. The stress-detecting

signaling pathways triggering the ISR converge at the phosphorylation of eIF2α that promotes translation of the master transcriptional regulator of the ISR - activating transcription factor 4 (ATF4) - and its translocation to the nucleus. To analyze whether the ISR is activated in response to the mtDNA depletion, the expression of *ATF4* and its primary downstream targets - *DDIT3, ATF3, CHAC1, PCK2, PPP1R15A* – was evaluated with RNA sequencing (Figure 24A). The expression of these genes was markedly upregulated – correspondingly, $\log_2$(FC): 1.84, 1.92, 2.19, 4.57, 2.26, 1.28; p-values: $1 \cdot 10^{-8}$, $2 \cdot 10^{-3}$, $8 \cdot 10^{-4}$, $4 \cdot 10^{-26}$, $1 \cdot 10^{-7}$, $6 \cdot 10^{-3}$. Therefore, the depletion of the mtDNA by ddC treatment activated mitochondrial signaling pathways triggering the ISR.

Impaired mitochondrial protein import and accumulation of orphaned ETC protein subunits can induce proteotoxic stress that activates mitochondrial unfolded protein response (mtUPR). To increase protein quality control and promote protein degradation, the regulatory mechanisms of mtUPR increase the transcription of mitochondrial proteases such as Lonp1, ClpP, paraplegin, Clpx, and Yme1l1 [164]. Additionally, the expression of mitochondrial chaperones Hsp70, Hsp60 and Hsp10 is upregulated in mtUPR to prevent protein aggregation and facilitate protein folding and assembly into the multiprotein complexes. To identify whether these processes were initiated following mtDNA depletion, differential expression analysis of genes encoding mitochondrial proteases (*LONP1, CLPP, SPG7, CLPX, YME1L*) or chaperones (*HSPA2, HSPD1, HSPE1*) was performed. Interestingly, no signs of the transcriptional upregulation typical for mtUPR were observed (Figure 24B). Thus, the ISR is the main retrograde signaling pathway initiated by the mtDNA depletion in astrocytoma cells.

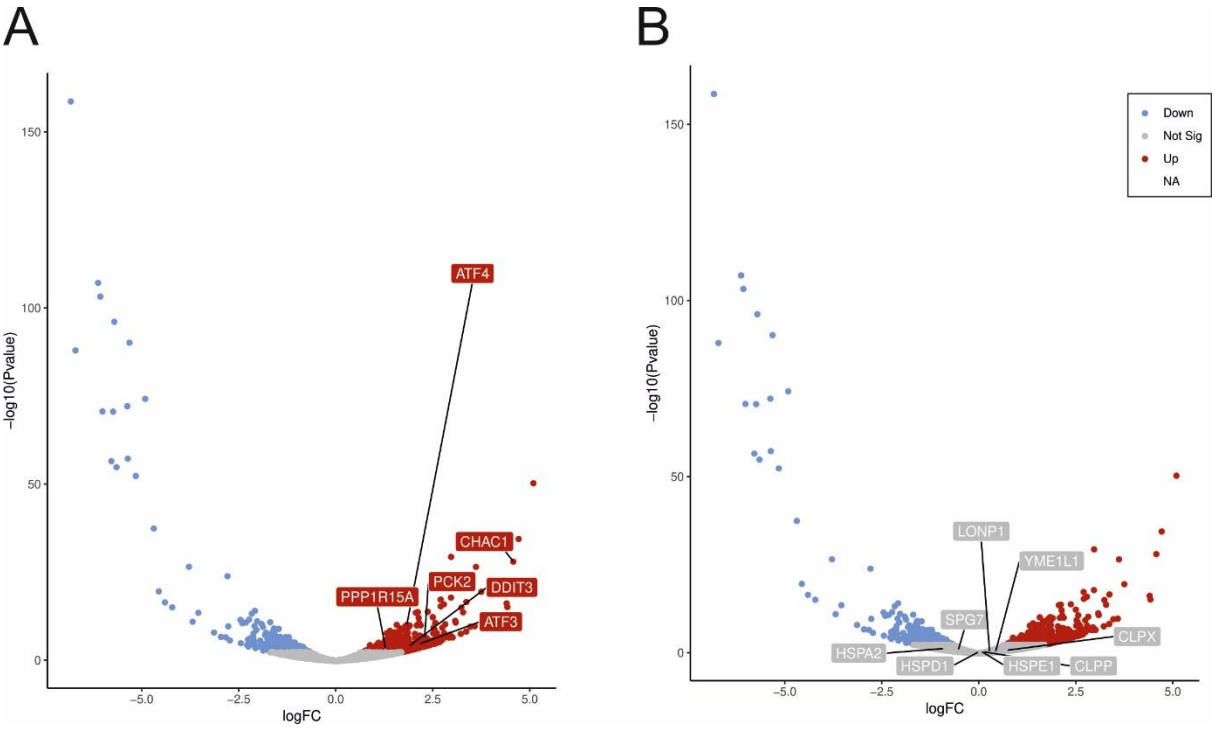

Figure 24. The integrated stress response pathway is activated in the mtDNA-depleted astrocytoma cells. The volcano plots of differential expression analysis with a focus on the following genes: (A) transcriptional regulators of the ISR and their primary downstream targets; (B) genes mediating the mtUPR. The value of $-\log_{10}$(p-value) is plotted on the y-axis against the $\log_2$(fold change) on the x-axis. Each identified gene is depicted as a dot, the upregulated genes are shown in red, the downregulated ones – in blue, and the genes without a statistically significant change in expression ($p > 0.05$) – in grey.

The expression of nuclear factor E2-related factor 2 (Nrf2) is one of the signaling branches downstream of ATF4. A functional network of the Nrf2-coregulated genes involves key mediators of cytoprotective antioxidant signaling. Specifically, Nrf2 regulates the expression of the genes encoding the components of the glutathione antioxidant system, such as glutamate-cysteine ligase subunits (*GCLC*, *GCLM*); thioredoxin-based enzyme system, such as thioredoxin (*TXN*), thioredoxin reductase 1 (*TXNRD1*) and sulfiredoxin (*SRXN1*); an enzyme involved in heme catabolism - heme oxygenase 1 (*HMOX1*) [165]. Interestingly, the expression of *KCNMA1* is a known target of transcriptional regulation by Nrf2 in the coronary smooth muscle cells. To identify whether KCNMA1 is co-regulated with these downstream effectors of Nrf2, differential expression analysis with a focus on the genes involved in a functional antioxidant system was performed. In mtDNA-depleted cells, the expression of most of the analyzed genes under the transcriptional regulation of Nrf2 was markedly upregulated, indicating that Nrf2 is activated in response to oxidative stress (Figure 25A). However, since in

the arterial smooth muscle cells Nrf2 positively regulates the expression of *KCNMA1*, other molecular mechanisms are likely involved in the downregulation of *KCNMA1* expression in the mtDNA-depleted astrocytoma cells.

Low availability of NAD^+ is a hallmark of mitochondrial dysfunction, and through the NAD+-containing transcription factors it affects expression of their gene targets, such as sirtuin-1 (Sirt1). Through the interaction with the peroxisome proliferator-activated receptor gamma coactivator-1α (PGC1α), Sirt1 controls mitochondrial biogenesis. The Sirt1/PGC1α-mediated impairment in the oxidative metabolism and decrease in the expression of genes regulating calcium homeostasis was described in the SCA7 mice model [166,167]. *KCNMA1* is positively regulated by PGC-1α due to the presence of PPAR response elements (PPRE) in the promotor region, and it was reported as one of the downregulated genes under the Sirt1/PGC1α control that were involved in calcium signaling [167]. mtDNA depletion could potentially disrupt the supply of NAD^+ due to the lack of complex I activity. Thus, the expression of SIRT1 and the primary downstream targets of Sirt1/PGC1α-dependent regulation, such as *NRF1*, *TFAM*, *FOXO1*, and *ESRRA*, was evaluated in the ddC-treated astrocytoma cells (Figure 25B). However, no significant change was observed in the differential expression analysis of these genes. This result can indicate that the NAD^+ pool was not affected in the mtDNA-depleted cells, likely due to its regeneration in the glycolytic reduction of pyruvate.

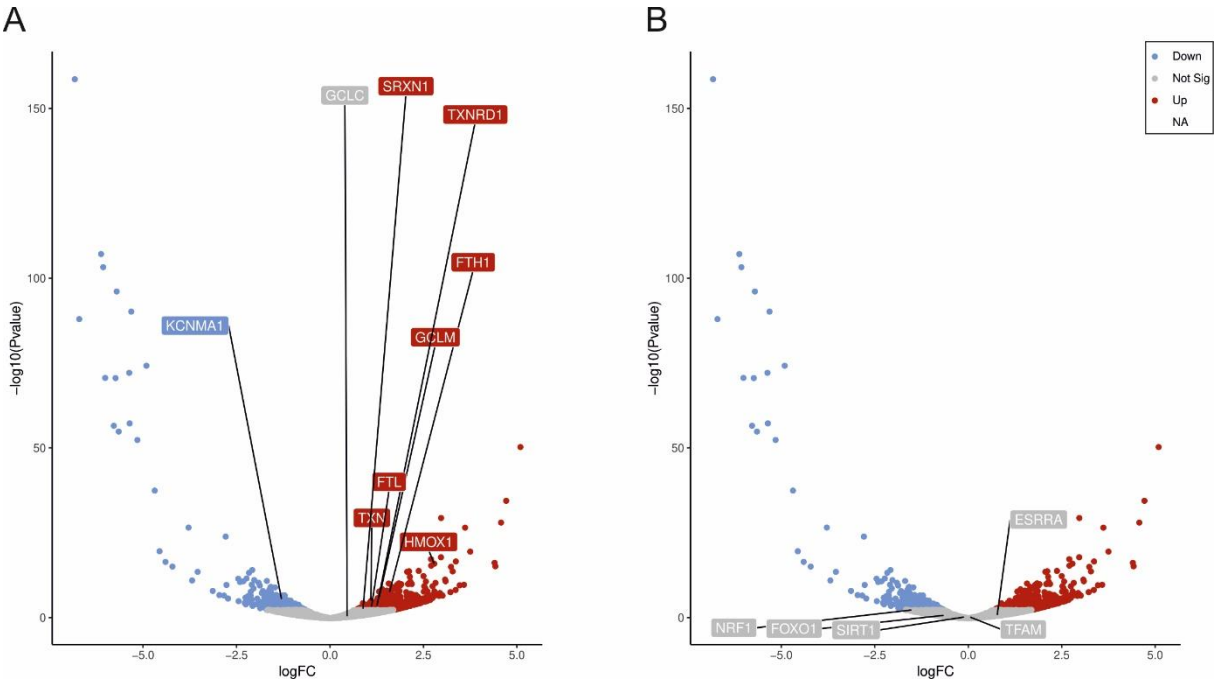

Figure 25. Expression of genes under the control of Nrf2 is upregulated in the mtDNA-depleted astrocytoma cells. The volcano plots of differential expression analysis with a focus on the following genes: (A) antioxidant enzymatic functional network under the common transcriptional control by Nrf2; (B) primary downstream targets of Sirt1/PGC1α transcriptional co-activation. The value of $-\log_{10}$(p-value) is plotted on the y-axis against the $\log_2$(fold change) on the x-axis. Each identified gene is depicted as a dot, the upregulated genes are shown in red, the downregulated ones – in blue, and the genes without a statistically significant change in expression ($p > 0.05$) – in grey.

To summarize, differential expression analysis in the mtDNA-depleted astrocytoma cells has identified the following features of their transcriptome profile:

- the expression of the gene encoding mitoBK-α was downregulated;
- the depletion of mtDNA initiated the integrated stress signaling pathway;
- a lack of evidence indicating mitochondrial unfolded protein response signaling was observed;
- the transcriptional upregulation of antioxidant enzymatic functional network under the common transcriptional control by Nrf2 occurred;
- no change in the expression of the primary downstream targets of Sirt1/PGC1α transcriptional co-activation was identified.

6.4. Evaluation of the effects of COX8A deficiency on the respiratory chain complexes and mitoBK channels

The results of the study of the interaction of the mitoBK channel with the ETC complexes in the cellular model lacking mtDNA revealed that the mitoBK channel interacts with the complex IV through its α and β4 subunits and that the genetically induced downregulation of the channel amount occurs. To further investigate how a deficiency in the partner ETC protein complex affects the mitoBK channel, a different approach based on the model with an isolated deficiency in COX was employed. Namely, human dermal fibroblasts derived from a patient with a mutation in a nuclear-encoded structural subunit COX8A were used as a study model.

COX8A is the smallest nuclear-encoded protein subunit of COX. In the human cells, it substitutes the subunit COX8B (COXVIIIH) commonly expressed in the most primate clades, and the ubiquitous expression of COX8A is considered an adaptive evolutionary change in the anthropoid RC machinery for optimized aerobic energy metabolism [168]. However, the molecular role of COX8A in the function of COX is still unknown. The model in the focus of this study is the single reported case of COX8A deficiency in a patient with Leigh syndrome [152].

6.4.1. Characterization of the respiratory chain in COX8A-deficient fibroblasts

Since there was no available information of how the impairment of COX8A affects the COX assembly and how the remaining COX was stabilized, in the first part of this work, the functional effects of the loss in COX8A on the COX and its complexes with the other respiratory chain enzymes were investigated.

6.4.1.1. Organization of the respiratory chain protein complexes upon COX8A deficiency in fibroblasts

To identify the impact of the isolated COX deficiency on the ETC enzymes, the protein complexes in the mitochondrial preparations of fibroblasts were resolved using BN-PAGE, and

subsequently immunoprobed with the antibodies for the subunits NDUFA9, SDHA, CORE2, COX4 of the respiratory chain complexes I, II, III and IV.

In the control fibroblast cells, the subunit COX4 was contained in four distinct fully assembled COX complexes (Figure 26). COX was distributed between the COX monomer form and the respirasomes, while a smaller amount was also present in the SC containing $CIII_2$ + CIV. In the patient fibroblasts, the residual COX was largely stabilized in the respirasomes, and no monomer or supercomplex ($CIII_2$ + CIV) forms of COX were detectable. Interestingly, in the COX8A-deficient fibroblasts, an increase in the abundance of the remaining RC complexes was observed.

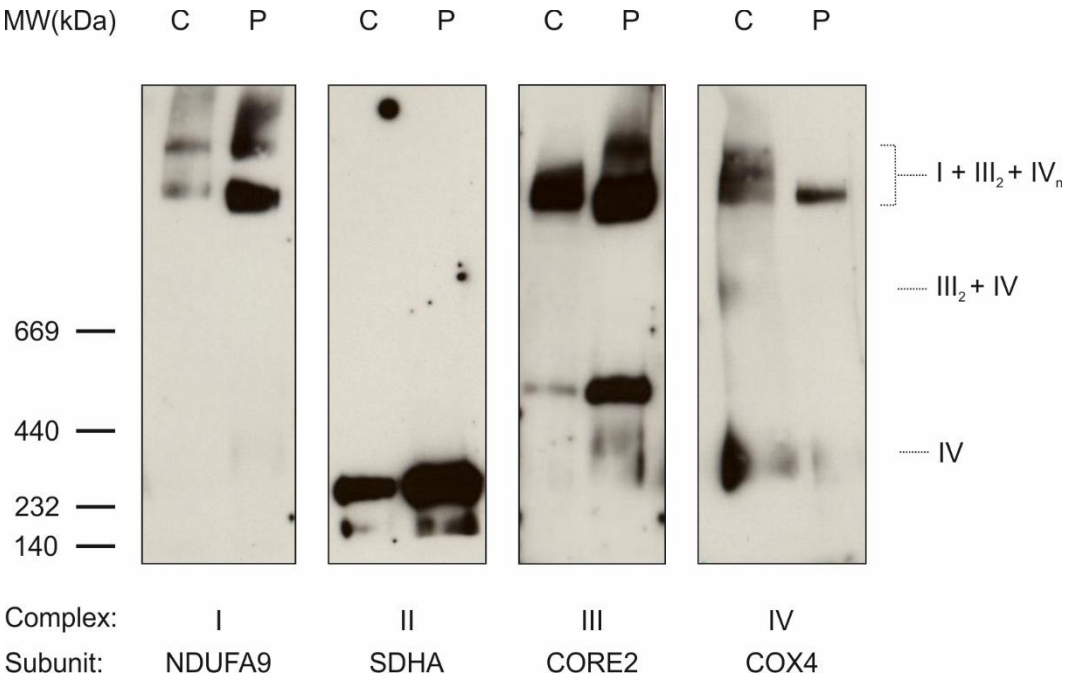

Figure 26. COX is stabilized in the supercomplexes in the COX8A-deficient fibroblasts. BN-PAGE with subsequent immunostaining, digitonin 1%. Mitochondrial preparation of control (C) and COX8A patient (P) fibroblasts, 100 µg protein/lane. On the right, COX-containing protein complexes: IV – COX monomer, III_2 + IV – supercomplex containing COX and dimer of complex III, I + III_2 + IV_n – respirasomes.

6.4.1.2. Evaluation of the protein content of the residual complex IV subunits in COX8A-deficient fibroblasts

Steady-state protein levels of the selected RC subunits were evaluated using SDS-PAGE with subsequent immunoblotting. Consistent with the observed decrease in the COX protein complexes in the COX8A-deficient patient fibroblasts, the protein amount of subunits COX1, COX2, COX4, and COX5A was decreased to various degrees (Figure 27). Specifically, the COX1 and COX5A protein signals were virtually not detectable, while the subunit COX4 was the least downregulated one. The subunits of other respiratory chain complexes were not compromised, and an increase in the amount of CORE2 was observed, in the line with the increased amount of complex III protein shown with BN-PAGE.

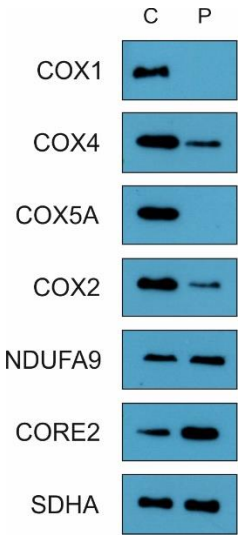

Figure 27. Steady-state levels of the selected subunits of respiratory chain complexes in the COX8A-deficient cells. SDS-PAGE with subsequent immunostaining: a) mitochondrial preparation of control (C) and COX8A-deficient patient (P) fibroblasts, 50 µg protein/lane.

6.4.1.3. Analysis of the expression of protein subunits of complex IV and other respiratory chain complexes in COX8A-deficient fibroblasts

To identify whether the changes in the RC protein levels can be explained by transcriptional regulation, the effects of COX8A deficiency on the expression of the genes encoding OXPHOS proteins were investigated with RNA sequencing. The analysis of the transcriptome of fibroblasts with COX8A deficiency identified a few differentially expressed RC protein-encoding genes (Figure 28). Namely, a small decrease in the transcription levels of mtDNA-

encoded COX3 subunit and ATP synthase subunits A6L and A was observed (log_2(FC): -0.91, -0.87; *p*-value: 0.03, 0.01, correspondingly), while the expression of nuclear-encoded subunits COX7A1 and COX7B of COX, and the amount of transcripts encoding complex III subunit 6, and subunits C3 and DAPIT of complex V was slightly increased (log_2(FC): 1.16, 0.86, 0.73, 0.68, 0.74; *p*-value: 6*10-5, 0.02, 0.04, 0.03, 0.04, correspondingly).

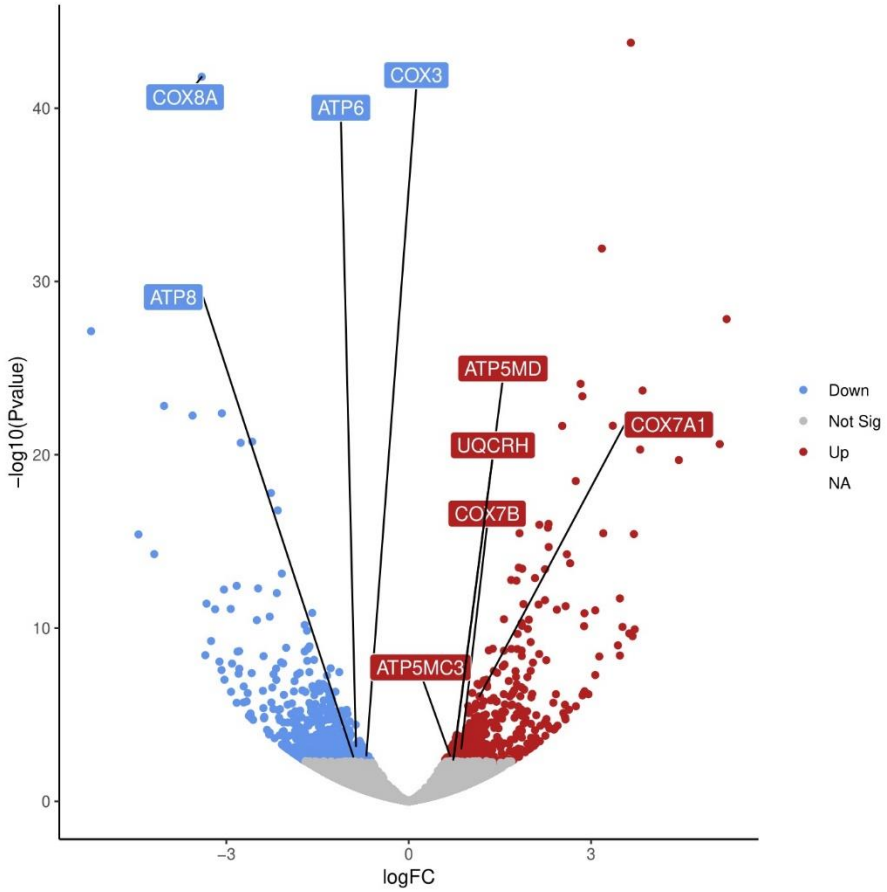

Figure 28. Differentially expressed genes encoding OXPHOS complexes in the COX8A-deficient fibroblasts. Volcano plot of gene expression in the COX8A patient fibroblasts compared to the control fibroblasts. Each identified gene sequence is represented by one point on the graph. The identified differentially expressed genes encoding subunits of RC complexes are shown in boxes. The horizontal axis is log_2(fold change) between the sample means, the vertical axis is -log_{10}(P-value). Grey points are not statistically significant ($p > 0.05$), red points show the upregulated genes ($p < 0.05$), blue points show the downregulated genes ($p < 0.05$).

6.4.2. The effects of the induced COX8A deficiency on the respiratory chain in HEK293T cells

To further characterize the effects of the loss of COX8A on COX and ETC, a cellular model was developed using the CRISPR/Cas9 genome editing system on HEK293T cells with the aim of obtain a stable cell line containing mutations in *COX8A*.

6.4.2.1. CRISPR/Cas9 induction of COX8A deficiency in HEK293T cells

CRISPR/Cas9 is a modern gene-editing method that has gained wide use due to its well-characterized mode of action and efficiency. This technique allows introducing a mutation into the target gene of interest, as the single guide RNA (sgRNA) directs the Cas9 enzyme with an endonuclease activity to introduce a double-stand break to the bound DNA region. The break is then repaired by non-homologous end joining, which tends to be imprecise and can lead to deletions or insertions. In principle, any nuclear gene can be targeted by CRISPR/Cas9 system in the immediate proximity to a region containing protospacer adjacent motifs, which are recognized by the sgRNA. For the purpose of this study, the dsDNA oligonucleotides encoding sgRNA targeting exon 1 of *COX8A* were designed and cloned into the commercially available plasmid as described in chapter 5.4.

HEK293T cells were transfected with the plasmid for CRISPR/Cas9, seeded as single-cell colonies, and allowed to grow, as described in chapter 5.4. Following the establishment of stable clonal colonies, screening for the mutants with a sought-after mutation in COX8A was performed taking advantage of Sanger sequencing as described in chapter 5.6.

While no viable mutant cell line was characterized as a full *COX8A* knockout, two clonal HEK293T cell lines were identified that harbored mutations in COX8A, and were marked as clone #13 and clone #14 (Figure 29).

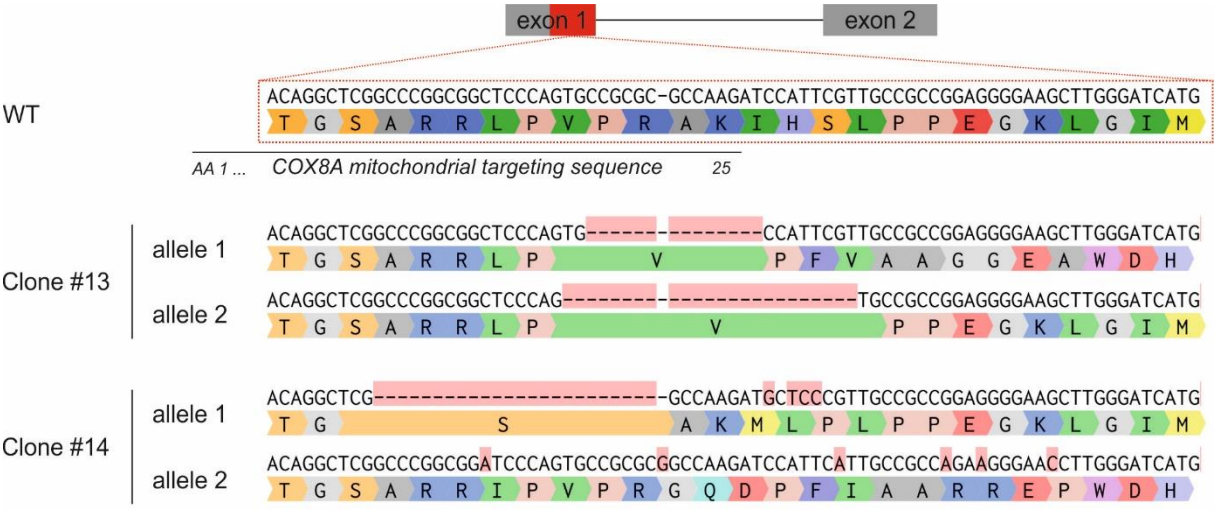

Figure 29. Characterization of the CRISPR/Cas9-induced mutations in *COX8A* in the HEK293T cells. Top panel, a fragment of the genomic DNA sequence of the WT *COX8A* exon 1 and translated peptide. The amino acids (AA) 1-25 form the mitochondrial targeting sequence of COX8A, and are marked with a line. Bottom panel, corresponding *COX8A* genomic sequences and translated peptide in the genetically modified HEK293T clones #13 and #14. The mutated nucleotide positions are highlighted in red.

In clone #13, allele 1 contained a frameshift mutation by a 14-nt deletion, producing an aberrant peptide from the amino acid position 22. In the second allele of clone #13 a 24-nt deletion has caused an in-frame deletion of the residues Pro22, Arg23, Ala24, Lys25, Ile26, His27, Ser28, and Leu29. The amino acids at the positions 22-25 are a structural part of the COX8A N-terminal mitochondrial targeting sequence (MTS).

In clone #14, a 24-nt in-frame deletion in allele 1 affects the MTS of COX8A, due to the deletion of the residues Ala16, Arg17, Arg18, Leu19, Pro20, Val21, Pro22, Arg23. Notably, by elimination of three out of four Arg residues in the COX8A MTS, this mutation disrupts a positively charged amphipathic helix that is required for mitochondrial import of the COX8A peptide. Moreover, four single-base substitutions in allele 1 result in a replacement of three amino acids: Ile26Met, His27Leu, Ser28Pro. In allele 2 of clone #14 a 1-nt insertion has occurred, leading to the frameshift mutation in *COX8A* generating an aberrant peptide from amino acid position 24.

6.4.2.2. The impact of COX8A deficiency on the organization of the respiratory chain complexes in HEK293T cells

The COX activity was assessed in the mitochondrial preparations of the fibroblasts and HEK293T cells with COX8A deficiency and the respective controls (Table 8). COX activity was evaluated relative to the citrate synthase (CS) activity [158]. In all COX8A-deficient cell lines, enzymatic activity of complex IV was decreased, however, residual COX activity was still detectable. The COX/CS activity ratio in the fibroblasts with the COX8A deficiency was decreased 5-fold. In each of the HEK293T clones (#13 and #14) with different deletions of COX8A mitochondrial targeting sequence the COX/CS activity ratio was decreased about 3-fold.

Table 8. Enzymatic activities of COX8A-deficient cell lines

Enzymatic activities (mU/mg protein)	Control fibroblasts	*COX8A*-mutant fibroblasts	HEK293T WT	HEK293T *COX8A*-KD clone 13	HEK293T *COX8A*-KD clone 14
Citrate synthase	61,5	79,8	158,6	189,3	172,6
NADH:ubiquinone oxidoreductase	11	3	5,2	4,1	1,6
Complex I/citrate synthase	0,17	0,04	0,03	0,02	0,01
Cytochrome *c* oxidase	81,4	20,6	81,3	32,5	27,3
Complex IV/citrate synthase	1,32	0,27	0,51	0,17	0,16

To identify how the mutations in COX8A in the gene-edited HEK293T cells affected the organization of the respiratory chain, the protein complexes in the mitochondrial preparations of HEK293T cells were resolved using BN-PAGE, and subsequently immunoprobed with the antibodies for the subunits NDUFA9, CORE2, COX4 of the respiratory chain complexes I, III and IV. In the WT HEK293T cells, the COX4 signal was distributed between four fully assembled protein complexes as well: COX monomers, dimers, $CIII_2$ + CIV, and respirasomes (Figure 30). The largest amount of COX was incorporated into the respirasomes, and the COX monomer was the least abundant form. In the COX8A-deficient HEK293T clone #13 with a shorter deletion in the COX8A MTS, the largest amount of COX was incorporated into respirasomes. However, a significant fraction of COX was also contained within the SC of $CIII_2$

+ CIV, and to a smaller extent, in COX dimers. The monomer form of COX was practically undetectable. The abundance of protein complexes containing COX in the COX8A-deficient clone #14 of HEK293T cells was significantly smaller than in both WT and clone #13 cells. Most of the residual COX proteins were largely contained within the respirasomes, while only trace amounts could be detectable within the supercomplex of $CIII_2$ + CIV or the COX monomer and dimer forms.

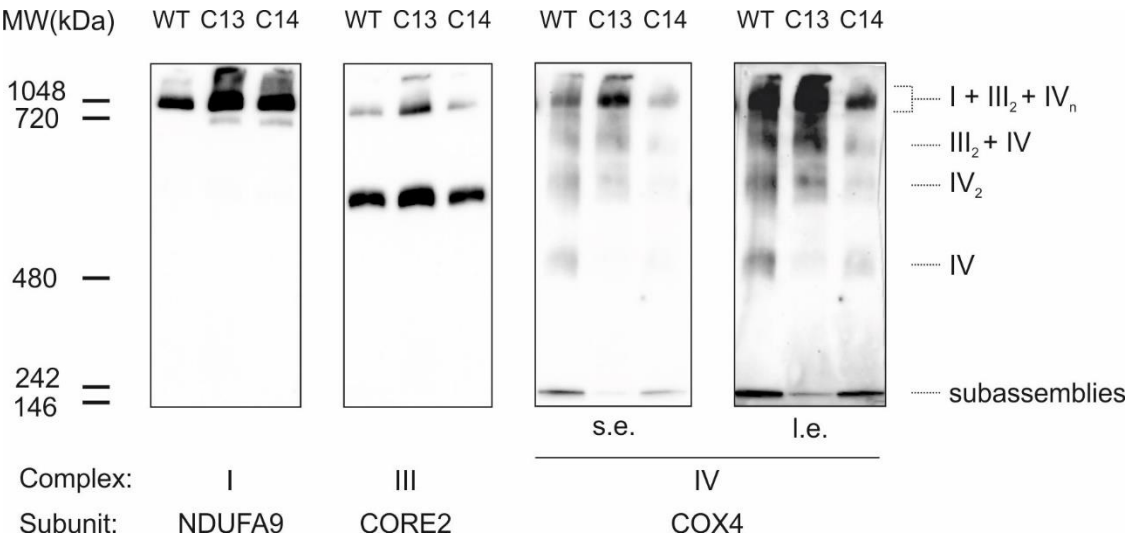

Figure 30. Organization of the respiratory chain in the CRISPR/Cas9 induced COX8A-deficient HEK293T cells. BN-PAGE with subsequent immunostaining, digitonin 1%. Mitochondrial preparation of the WT and COX8A-deficient HEK293T cells – clone #13 (C13) and clone #14 (C14), 100 µg protein/lane. S.e. and l.e. – short exposure and long exposure. On the right, COX-containing protein complexes: IV – COX monomer, IV_2 – COX dimer, III_2 + IV – supercomplex containing COX and dimer of complex III, I + III_2 + IV – respirasomes.

6.4.2.3. Evaluation of the protein amount of the residual complex IV subunits upon COX8A deficiency in HEK293T cells

Steady-state protein levels of selected RC subunits were evaluated with SDS-PAGE with subsequent immunoblotting.

In the HEK293T cell lines with a smaller (clone #13) and larger (clone #14) deletions in COX8A MTS, the COX protein levels were considerably reduced (Figure 31). Similar to the fibroblasts, the strongest decrease was observed for the subunits COX1 and COX5A, while the subunit COX4 was the least affected. Notably, the decrease in the COX subunits amount was

more pronounced in the clone #14 with the larger deletion in the COX8A MTS. However, no upregulation in the protein levels of the subunits of other OXPHOS complexes was observed.

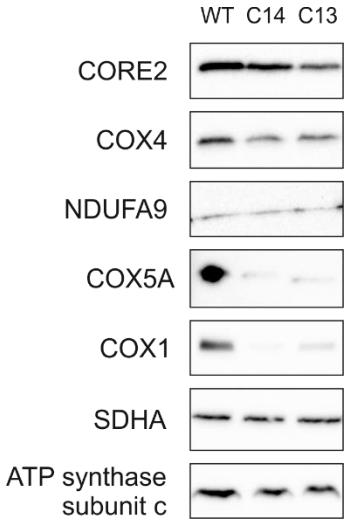

Figure 31. Steady-state levels of selected subunits of respiratory chain complexes in COX8A-deficient cells HEK293T cells. SDS-PAGE with subsequent immunostaining, mitochondrial preparation of the WT and COX8A-deficient HEK293T cells – clone #14 (C14) and clone #13 (C13), 50 µg protein/lane.

6.4.2.4. Analysis of the expression of protein subunits of complex IV and other respiratory chain complexes in COX8A-deficient HEK293T cells

To identify whether the changes in the RC protein levels can be explained by transcriptional regulation, the effects of COX8A deficiency on the expression of the genes encoding OXPHOS proteins were investigated with RNA sequencing. The analysis of transcriptome of the COX8A-deficient clone #14 HEK293T cells identified multiple genes encoding subunits of RC complexes that were differentially expressed (Figure 32). Specifically, the expression of all but one mtDNA genes encoding RC proteins was increased: subunits ND1, ND2, ND3, ND4, ND4L of complex I (log_2(FC): 0.45, 0.47, 0.63, 0.42, 0.61; p-value: $2*10^{-3}$, $1*10^{-3}$, $4*10^{-6}$, 0.01, $4*10^{-5}$, correspondingly), cytochrome *b* of complex III (log_2(FC): 1.4; p-value: $1*10^{-21}$, correspondingly), subunits A and A6L of complex V (log_2(FC): 0.8, 0.65; p-value: $3*10^{-8}$, $2*10^{-6}$, correspondingly), and COX2 and COX3 of complex IV (log_2(FC): 0.34, 0.61; p-value: 0.03, $9*10^{-5}$, correspondingly). The expression of the nuclear-encoded subunits A, B1 and γ of complex V was upregulated as well (log_2(FC): 0.72, 0.66, 0.79; p-value: $4*10^{-4}$, $7*10^{-3}$, $2*10^{-4}$, correspondingly). However, the transcript amounts of the nuclear-encoded COX subunits

COX4I1, COX6A1, COX6C, COX7A2, COX7A2L, COX7C (log_2(FC): -0.48, -0.52, -0.41, -0.6, -0.6, -0.4; p-value: $6*10^{-3}$, $6*10^{-3}$, 0.03, $6*10^{-4}$, $4*10^{-3}$, 0.03, correspondingly), and complex I subunits NDUFA1, NDUFS8, NDUFB10 were decreased (log_2(FC): -0.67, -0.7, -0.51; p-value: $2*10^{-3}$, $1*10^{-3}$, 0.04, correspondingly).

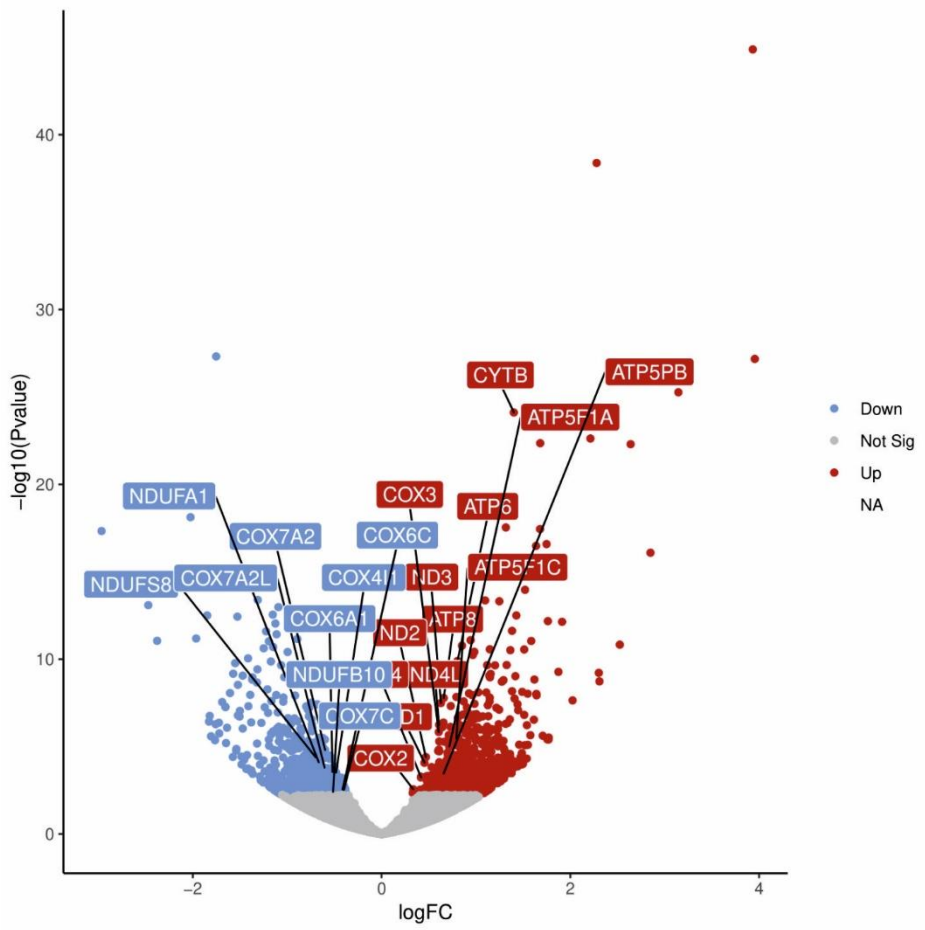

Figure 32. Differentially expressed genes encoding OXPHOS complexes in the COX8A-deficient fibroblasts. Volcano plot of gene expression in the COX8A patient fibroblasts compared to the control fibroblasts. Each identified gene sequence is represented by one point on the graph. The identified differentially expressed genes encoding subunits of RC complexes are shown in boxes. The horizontal axis is log_2(fold change) between the sample means, the vertical axis is $-log_{10}$(P-value). Grey points are not statistically significant ($p > 0.05$), red points show the upregulated genes ($p < 0.05$), blue points show the downregulated genes ($p < 0.05$).

6.4.3. Estimation of the impact of the COX8A deficiency on mitoBK channels in human fibroblasts

The COX8A-deficient cells provided an intriguing model of the isolated COX deficiency, where the residual COX was still present and was largely restricted to respirasomes, while other

ETC complexes remained largely structurally intact. Thus, the interaction of mitoBK channels with the defect COX in this system was the next question addressed in this work. The study model was limited only to fibroblasts with COX8A deficiency, since HEK293T cells are recognized for not expressing any functional K^+ channels in the IMM [77].

6.4.3.1. Assessment of the protein complexes of mitoBK with complex IV

To identify an impact of the COX8A deficiency on the protein complexes formed by mitoBK-α subunit and the ETC in the mitochondria of fibroblasts, multiprotein complexes in mitochondria of COX8A-deficient patient's fibroblasts and matched control cells were resolved and identified using BN-PAGE followed by Western blotting.

In the mitochondrial preparation of both cell types, the mitoBK-α signal was detected only in the same type of protein complexes, likely formed by a tetramer of mitoBK-α subunits and the associated mitoBK-β subunits. Notably, the amount of the complexes formed by the mitoBK-α was lower in the COX8A-deficient cells. The presence of mitoBK-α subunit in a band co-migrating with the respirasome, as observed in the astrocytoma WT cells, could not be detected. However, it should be noted that the gene expression and protein amount of mitoBK-α is noticeably lower in fibroblasts than in astrocytoma cells. Thus, it cannot be ruled out that a subpopulation of mitoBK channels exists in a respirasome-associated state, but is not discernible by this method due to their low abundance.

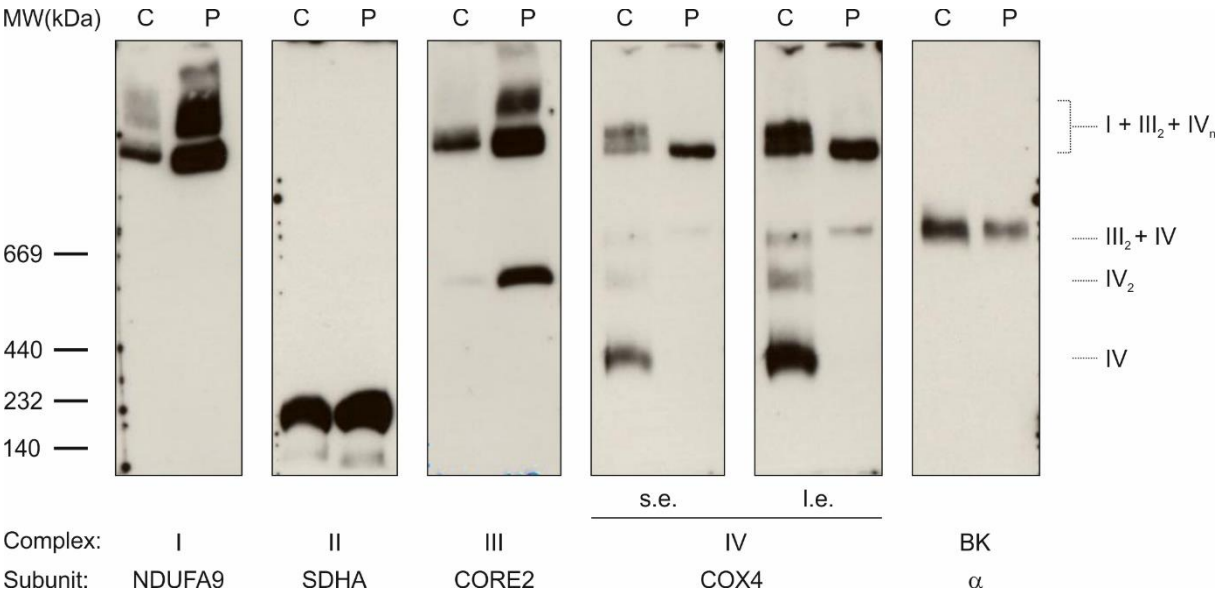

Figure 33. The amount of protein complexes formed by the mitoBK-α subunit is decreased in COX8A-deficient cells. BN-PAGE with subsequent immunostaining, digitonin 1%. Mitochondrial preparation of control (C) and COX8A patient (P) fibroblasts, 100 µg protein/lane. S.e. and l.e. – short exposure and long exposure. On the right, COX-containing protein complexes: IV – COX monomer, IV_2 – COX dimer, III_2 + IV – supercomplex containing COX and dimer of complex III, I + III_2 + IV – respirasomes.

6.4.3.2. Evaluation of mitoBK protein amount in fibroblasts with COX8A deficiency

To verify the decrease in the protein amount of the mitoBK-α subunit observed with BN-PAGE/Western blotting, the comparative analysis of the total protein levels of mitoBK-α subunit in mitochondria isolated from the control and COX8A-deficient fibroblasts was performed by SDS-PAGE/Western blotting.

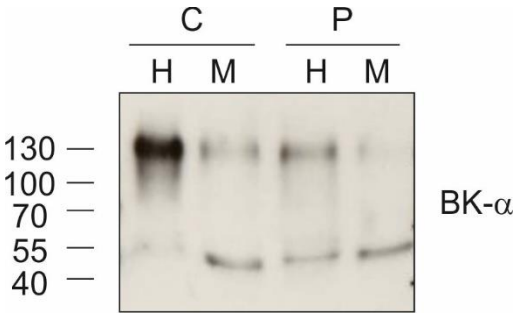

Figure 34. The amount of mitoBK-α channel is downregulated in the mitochondria of COX8A-deficient fibroblasts. SDS-PAGE with subsequent immunostaining of total cell homogenate (H) and mitochondrial preparations (M) of control (C) and COX8A patient (P) fibroblasts, 100 µg protein/lane.

The results of the study confirmed the decrease in the total amount of the total full-sized BK-α protein in cell lysate, and in particular mitoBK-α protein in the mitochondria of COX8A-deficient fibroblasts (Figure 34).

6.4.3.3. Analysis of the expression of mitoBK subunits in fibroblasts with COX8A deficiency

As a conclusion of the analyses on the protein level, the decrease in the mitoBK-α subunit was observed in both COX-deficient models: with the large-scale impairment of ETC caused by the mtDNA depletion, and in a model with isolated COX deficiency due to the mutation in COX8A subunit. In addition, it was shown that the amount of mitoBK-α is downregulated on the level of gene expression in the mtDNA-depleted cells. These observations raise the question of whether the observed decrease in the mitoBK-α amount is transcriptionally regulated in the COX8A-deficient fibroblasts as well. To address it, differential gene expression analysis was performed using the RNA sequencing data.

RNA sequencing detected the expression of three genes encoding BK channel subunits in both control and patient fibroblasts: *KCNMA1*, *KCNMB3*, and *KCNMB4*. However, no statistically significant change in the expression of these genes was observed (Figure 35).

To confirm a lack of the change in the expression of *KCNMA1* observed with RNA sequencing, real-time reverse-transcription polymerase chain reaction (qRT-PCR) was performed. No statistically significant decrease in the expression of *KCNMA1* was detected in a qRT-PCR assay with *GAPDH* as a reference gene (Figure 36).

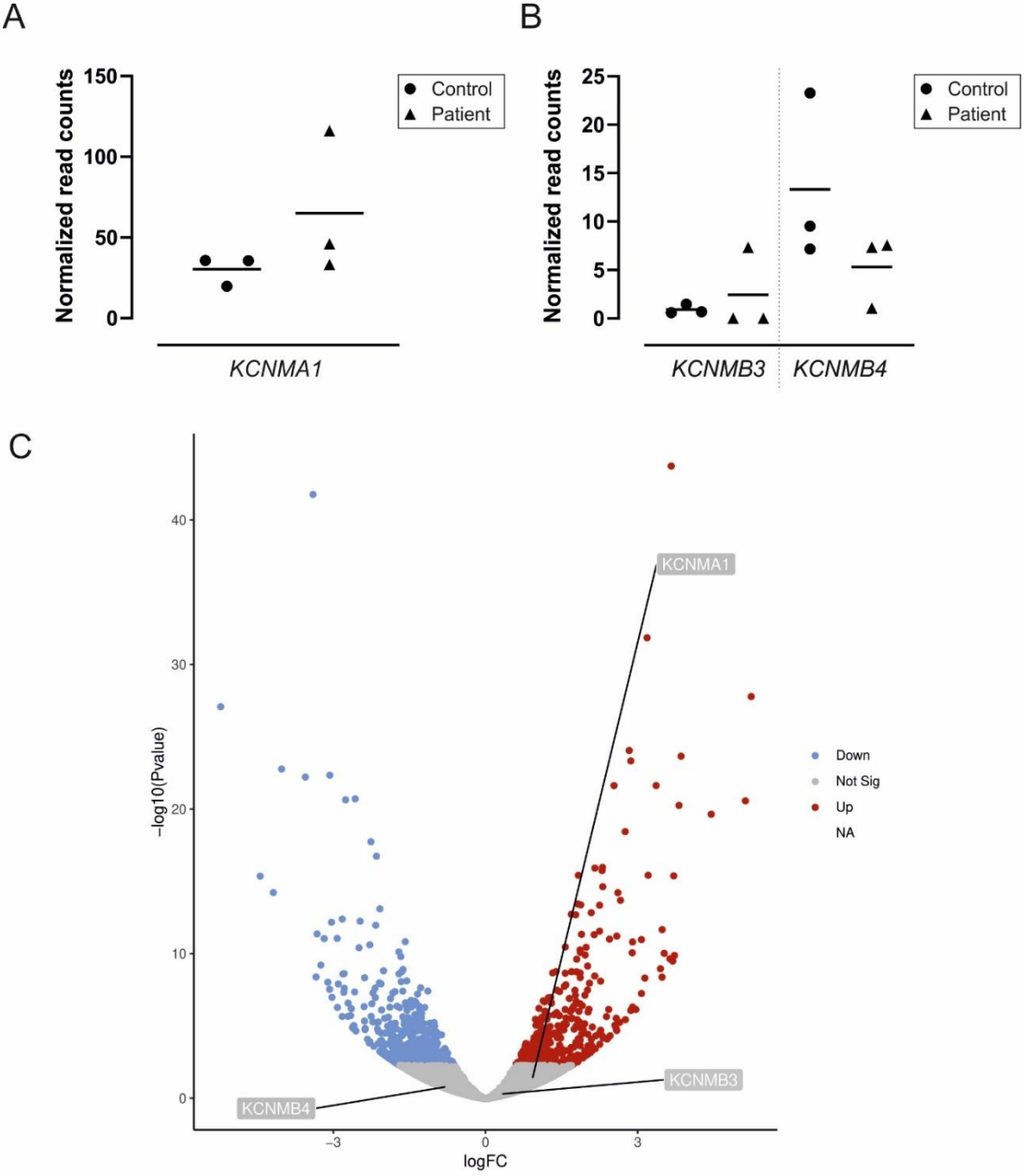

Figure 35. No statistically significant change in the expression of genes encoding mitoBK subunits is observed in COX8A-deficient fibroblasts. The volcano plot graphically identifies differential expression of genes: the value of $-\log_{10}$(p-value) is plotted on the y-axis against the $\log_2$(fold change) on the x-axis. The change in value for each assigned gene sequence is depicted by one point. The upregulated transcripts are labeled in red, downregulated – in blue, and the transcripts without a statistically significant change in expression ($p > 0.05$) – in grey.

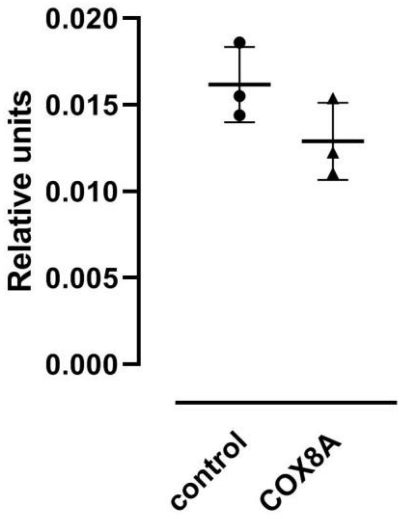

Figure 36. No significant change in *KCNMA1* expression in fibroblasts with a mutation in COX8A is detected by qRT-PCR. Expression level of *KCNMA1* gene is shown in relation to GAPDH (n = 3).

6.4.3.4. Transcriptome profiling of the COX8A-deficient fibroblasts with high-throughput RNA sequencing

To analyze whether a deficiency in COX8A in the patient fibroblasts led to a change in the gene expression of other OXPHOS proteins, the differential gene analysis was performed with a focus on this group of genes.

The analysis of the transcriptome of fibroblasts with COX8A deficiency identified a few differentially expressed RC protein-encoding genes (Figure 37). Namely, a small decrease in the transcription levels of mtDNA-encoded COX3 subunit and ATP synthase subunits A6L and A was observed (log_2(FC): -0.91, -0.87; p-value: 0.03, 0.01, correspondingly), while the expression of nuclear-encoded subunits COX7A1 and COX7B of COX, and the amount of transcripts encoding cytochrome b-c1 complex subunit 6, and subunits C3 and DAPIT of complex V was slightly increased (log_2(FC): 1.16, 0.86, 0.73, 0.68, 0.74; p-value: 6*10-5, 0.02, 0.04, 0.03, 0.04, correspondingly).

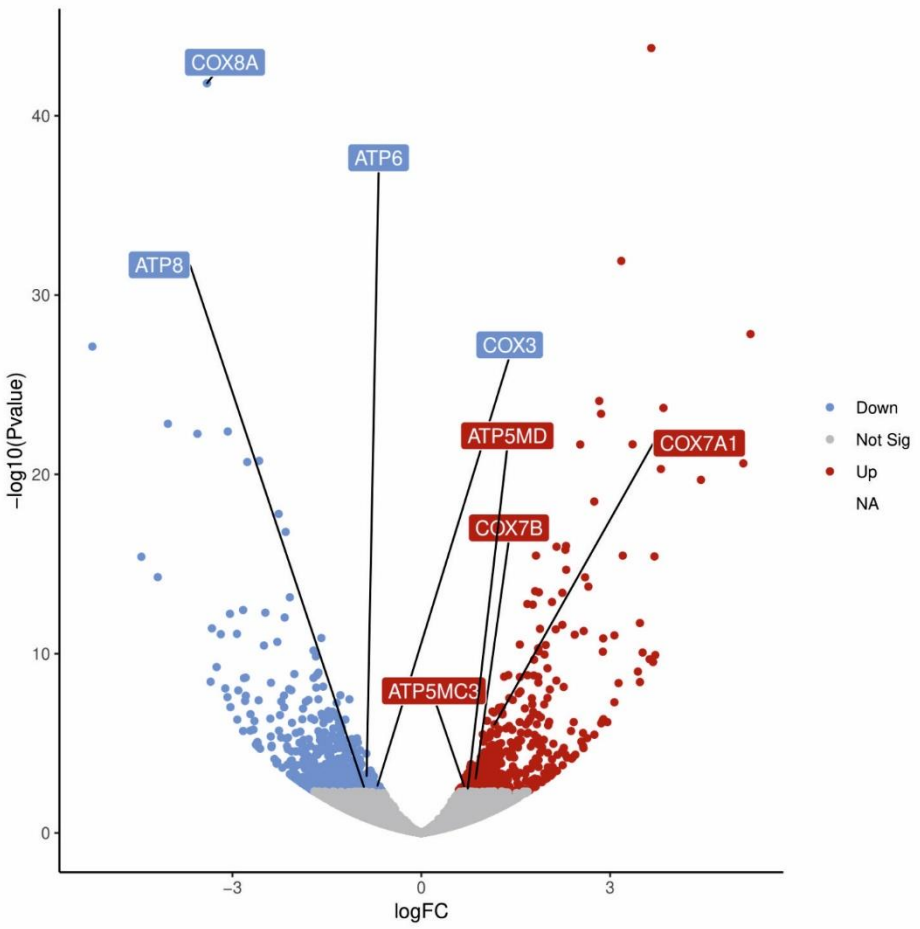

Figure 37. Differentially expressed genes encoding OXPHOS complexes in the COX8A-deficient fibroblasts. Volcano plot of gene expression in the COX8A patient fibroblasts compared to the control fibroblasts. Each identified gene sequence is represented by one point on the graph. The identified differentially expressed genes encoding subunits of RC complexes are shown in boxes. The horizontal axis is $\log_2$(fold change) between the sample means, the vertical axis is $-\log_{10}$(P-value). Grey points are not statistically significant ($p > 0.05$), red points show the upregulated genes ($p < 0.05$), blue points show the downregulated genes ($p < 0.05$).

According to the modular COX biogenesis paradigm, the subunit COX8A is joining the assembly process in the COX2-containing second module. The identified decrease in the amount of the COX monomers in the COX8A-deficient cells can indicate that this protein complex is not stable and that orphaned subunits of the first or second COX assembly module may exist and potentially accumulate in mitochondria. To determine whether a COX8A deficiency triggers mitochondrial retrograde signaling, expression of the key transcriptional regulators and their downstream targets of the mitochondrial unfolded protein response (mtUPR) and the integrated stress response (ISR) pathways were evaluated with RNA sequencing.

In the transcriptome profile of fibroblasts with the COX8A deficiency, no upregulation of the genes encoding the mitochondrial proteases ClpP, ClpX, Lonp1, paraplegin, and YME1L (*CLPP*, *CLPX*, *LONP1*, *SPG7* and *YME1L*, correspondingly) has been observed (Figure 38). The expression of the genes *HSPA9* and *HSPD1* encoding mitochondrial chaperones was unaltered in the COX8A patient fibroblasts as well. In the ISR, the phosphorylated eIF2α induces the expression of the central transcriptional regulators of ISR - ATF4 and its canonical target CHOP**.** However, no increase in the expression of ATF4 and CHOP was observed in the COX8A-deficient fibroblasts (Figure 38).

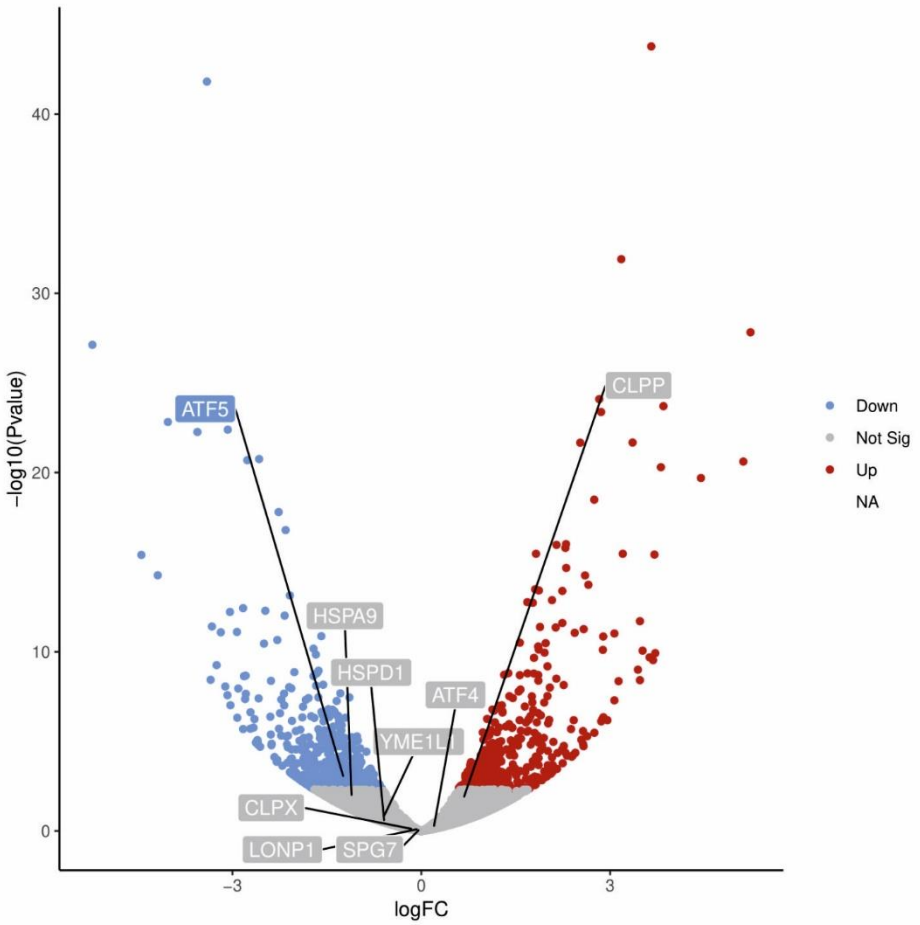

Figure 38. mtUPR and ISR are not activated in the COX8A-deficient fibroblasts. Volcano plot of gene expression in the COX8A patient fibroblasts compared to the control fibroblasts. Each identified gene sequence is represented by one point on the graph. The selected gene names are shown in boxes. The horizontal axis is $\log_2$(fold change) between the sample means, the vertical axis is -$\log_{10}$(P-value). Grey points are not statistically significant ($p > 0.05$), red points show the upregulated genes ($p < 0.05$), blue points show the downregulated genes ($p < 0.05$).

6.5. Patch-clamp study of the molecular mechanisms of carbon monoxide modulation of mitoBK channel activity

6.5.1. The effects of structurally different CO-releasing molecules on mitoBK channel activity

Mitochondria isolated from astrocytoma cells with established characteristics of mitoBK channel activity were used in the patch-clamp study of the mitoBK channel as a signaling effector of carbon monoxide (CO). In the first part of this study, three structurally distinct CORMs were applied to the mitoBK channels to study the effects of CO donors.

First, the effects of CORM-401 were investigated, as this CO donor had been previously reported as a mitoBK channel opener in a patch-clamp study on mitochondria of endothelial cells [137]. The single-channel mitoBK channel activity recordings following the application of 10 μM CORM-401 are shown in Figure 39A and Figure 39B at -40 mV and +40 mV, respectively. As previously stated, the inside-out configuration of the patch requires that the perfusion solution be administered to the mitochondrial matrix side of the IMM with an exposed C-terminal part of the channel. Interestingly, perfusion with 10 μM CORM-401 in 1 μM Ca^{2+} solution did not exhibit an apparent modulatory effect on the mitoBK channel activity (Figure 39).

Since the findings of this study diverged from those previously reported, a structurally different class of CORMs was selected to validate the results. The mitoBK channel-containing patches were perfused with a ruthenium carbonyl CORM-2 (Figure 40). During the first minute of patch perfusion with 30 μM CORM-2 in 1 μM Ca^{2+} solution, two different types of initial responses of the mitoBK channels were observed (Figure 40, insert). One set of responses (group 1) indicated transient activation of channels upon CORM-2 application (n = 4): the channel $P_{(o)}$ at -40 mV increased from 0% to 12% ± 7%, and from 7% ± 3% to 46% ± 17%, at +40 mV. However, continuous perfusion showed a biphasic characteristic of the CORM-2 action, in which the initial activation was followed by the channel inhibition in all recordings taken ~5 min after the 30 μM CORM-2 application. The other set of responses (group 2) was characterized by no significant change in channel activity in the presence of CORM-2 during the 1st and 5th minutes of continuous perfusion (n = 6). At +40 mV, the relative $P_{(o)}$ of the channels was 2% ± 2% under high-calcium conditions, and it changed to 1% ± 1% that of the control $P_{(o)}$, after perfusion with CORM-2.

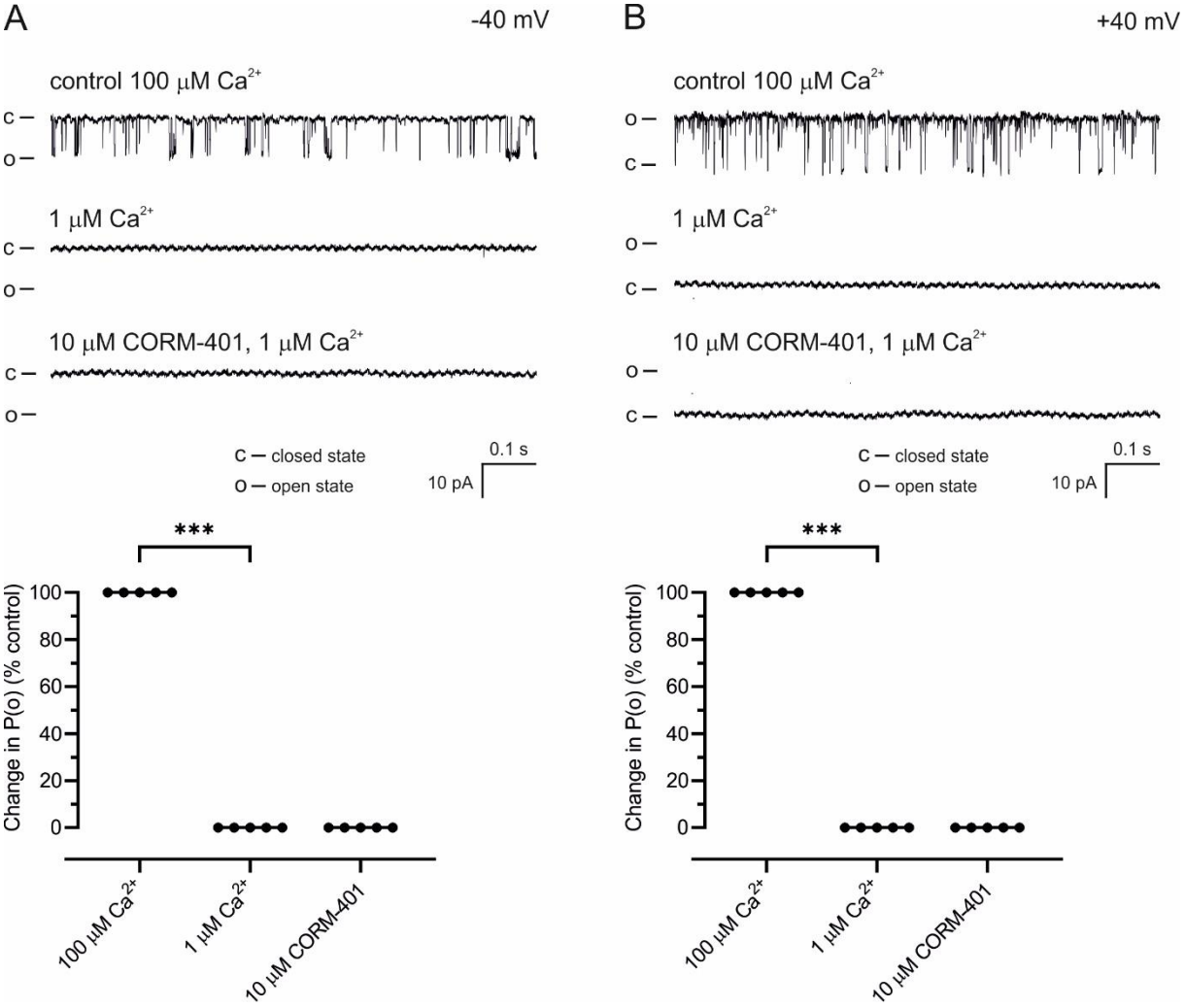

Figure 39. Lack of apparent effect of CORM-401 on the mitoBK channels. Representative traces of mitoBK single-channel recordings at -40 mV (A) and +40 mV (B) after perfusion with symmetric 150/150 mM KCl solutions: the high calcium control solution (100 μM Ca^{2+}), the low calcium solution (1 μM Ca^{2+}), and the low-calcium solution containing 10 μM CORM-401. Changes in the mean $P_{(o)}$ values upon perfusion with the low calcium solution and that with CORM-401 at -40 mV (A) and +40 mV (B) were evaluated for individual experiments.

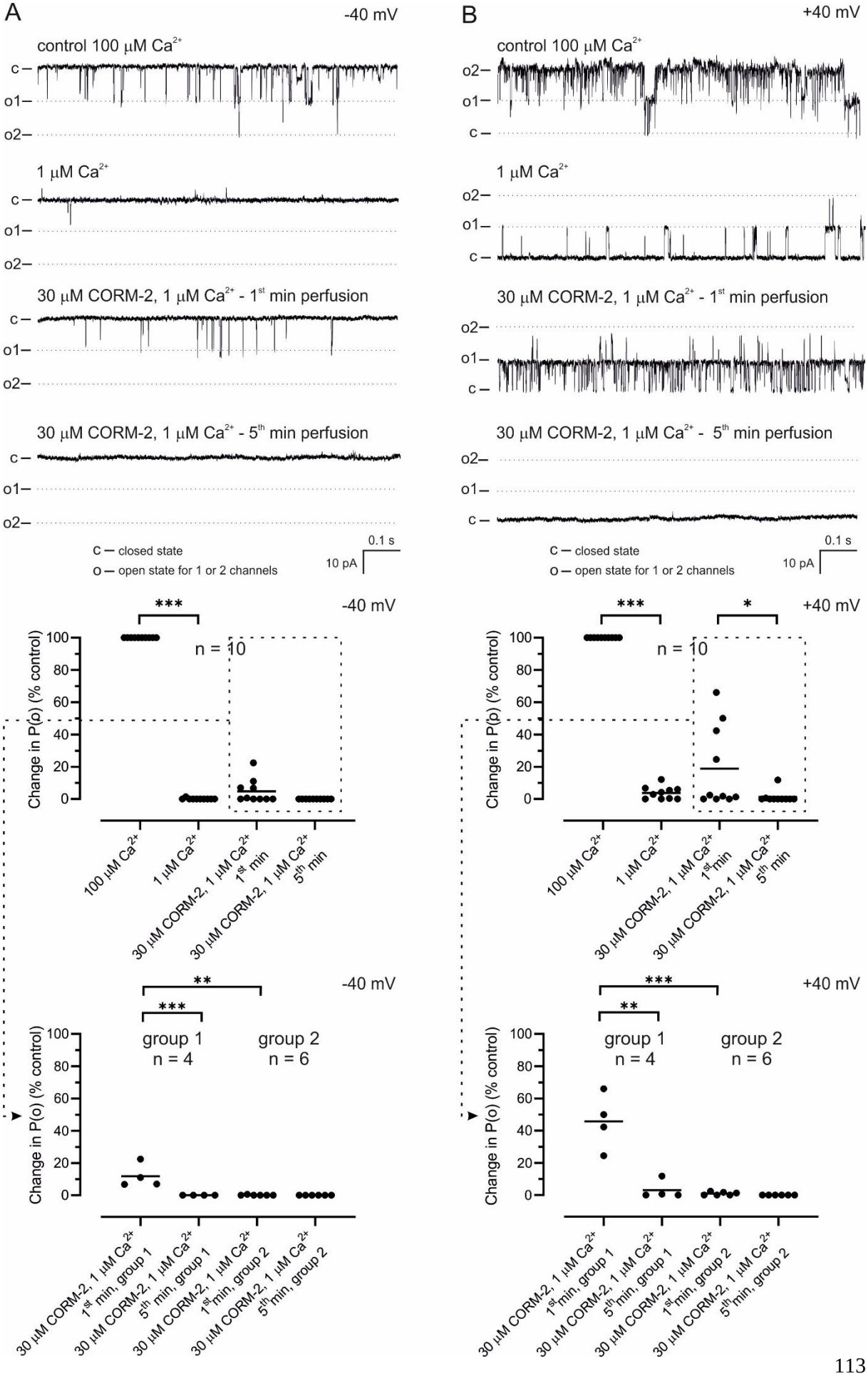
A
-40 mV
control 100 μM Ca2+
1 μM Ca2+
30 μM CORM-2, 1 μM Ca2+ - 1st min perfusion
30 μM CORM-2, 1 μM Ca2+ - 5th min perfusion
c
o1
o2
c — closed state
o — open state for 1 or 2 channels
0.1 s
10 pA
B
+40 mV
control 100 μM Ca2+
1 μM Ca2+
30 μM CORM-2, 1 μM Ca2+ - 1st min perfusion
30 μM CORM-2, 1 μM Ca2+ - 5th min perfusion
c — closed state
o — open state for 1 or 2 channels
0.1 s
10 pA
-40 mV
+40 mV
***
*
n = 10
Change in P(o) (% control)
100 μM Ca2+
1 μM Ca2+
30 μM CORM-2, 1 μM Ca2+ 1st min
30 μM CORM-2, 1 μM Ca2+ 5th min
**
group 1
n = 4
group 2
n = 6
30 μM CORM-2, 1 μM Ca2+ 1st min, group 1
30 μM CORM-2, 1 μM Ca2+ 5th min, group 1
30 μM CORM-2, 1 μM Ca2+ 1st min, group 2
30 μM CORM-2, 1 μM Ca2+ 5th min, group 2

Figure 40. Complex CORM-2 modulation of the mitoBK channels. Representative traces of the mitoBK single-channel recordings at -40 mV (A) and +40 mV (B) after perfusion with symmetric 150/150 mM KCl solutions: the high-calcium control solution (100 μM Ca^{2+}), the low-calcium solution (1 μM Ca^{2+}), and the low-calcium solution containing 30 μM CORM-2. Changes in the mean $P_{(o)}$ values upon perfusion with the low-calcium solution with CORM-2 at -40 mV (A) and +40 mV (B) were evaluated for individual experiments. The biphasic effect of the application of CORM-2 can be observed in the course of the experiment, as illustrated by the changes in mean $P_{(o)}$ values at the start (1^{st} minute) and the end (5^{th} minute) of the perfusion.

Due to the discrepancies between the observed effects of CORM-401 and CORM-2, the modulation of the mitoBK channels was assessed with yet another CO-donor of different chemistry, sodium boranocarbonate CORM-A1 (Figure 41). In this case, perfusion with 30 μM CORM-A1 in the 1 μM Ca^{2+} solution resulted in a slight decrease in the channel $P_{(o)}$ from 8% to 2%, compared to the $P_{(o)}$ of the control, at +40 mV (n = 4) (Figure 41A). The activity of the channel recorded at -40 mV with the 1 μM Ca^{2+} solution was unchanged after perfusion with CORM-A1 (Figure 41B).

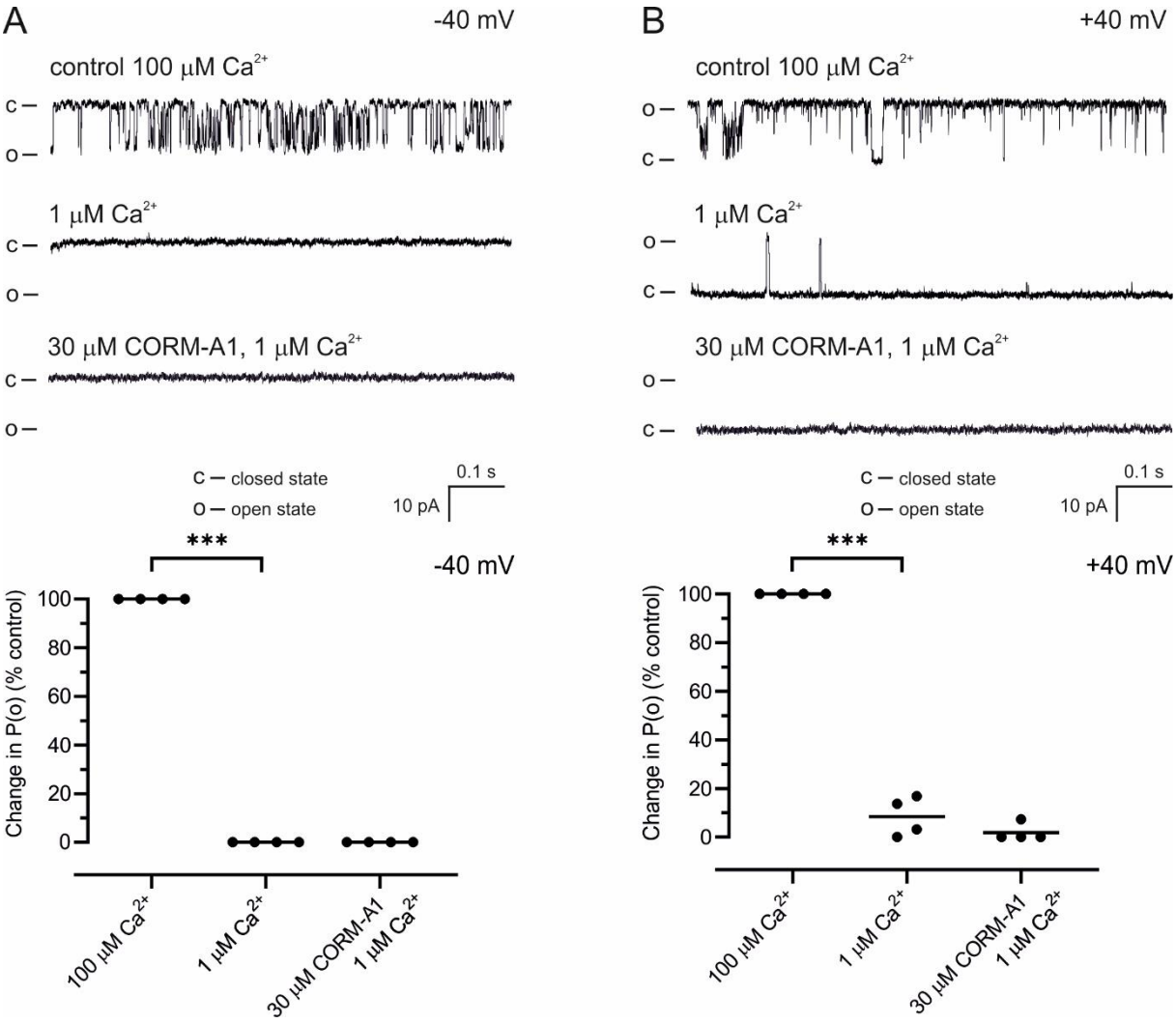

Figure 41. Lack of stimulation of the mitoBK channels by CORM-A1. Representative traces of mitoBK single-channel recordings at -40 mV (A) and +40 mV (B) after perfusion with symmetric 150/150 mM KCl solutions: the high-calcium control solution (100 μM Ca^{2+}), the low-calcium solution (1 μM Ca^{2+}), the low-calcium solution containing 30 μM CORM-A1. Changes in the mean $P_{(o)}$ values upon perfusion with the low-calcium solution with CORM-A1 at -40 mV (A) and +40 mV (B) were evaluated for the individual experiments.

6.5.2. Evaluation of the CO gas modulation of mitoBK activity

To ultimately clarify the contribution of CO to the effects observed after CORMs application, IMM patches with mitoBK channels were perfused with solutions saturated with the CO gas. The concentration of the CO gas in the CO-bubbled solutions was estimated to be ~1 mM. The presence of the CO in the CO-bubbled solution was confirmed by the change in the myoglobin absorption spectrum in the CO-containing solution as described in chapter 5.13. Specifically,

two peaks were observed in the proximity of the wavelengths characteristic for carboxymyoglobin - λ_1 = 540 nm and λ_2 = 577 nm (Figure 42).

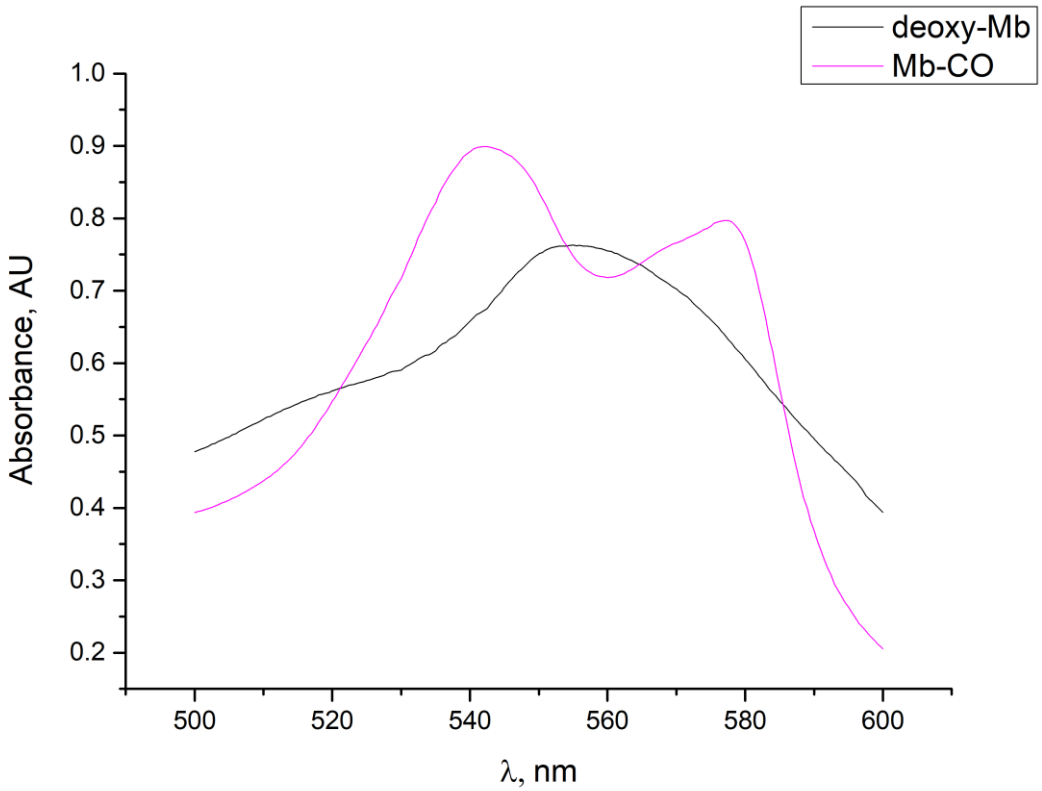

Figure 42. The change in the absorption spectrum of myoglobin in a solution perfused with CO indicates the formation of carboxymyoglobin. DeoxyMb (in black) – myoglobin in a control solution; Mb-CO (in pink) – myoglobin in a CO-saturated solution.

The first set of experiments showed that the low activity of the channel in 1μM Ca^{2+} solution was not increased after perfusion with the 1 μM Ca^{2+} solution saturated with CO (Figure 43). Upon the subsequent change to a CO-saturated solution with 100 μM Ca^{2+}, the channel $P_{(o)}$ was increased to the levels, which were not significantly different from those observed for the control conditions with 100 μM Ca^{2+}, which were 99% ± 2% and 92% ± 4% at +40 mV and -40 mV, respectively (n = 4). These observations suggest a lack of CO effect when carbon monoxide was applied alone in all tested conditions.

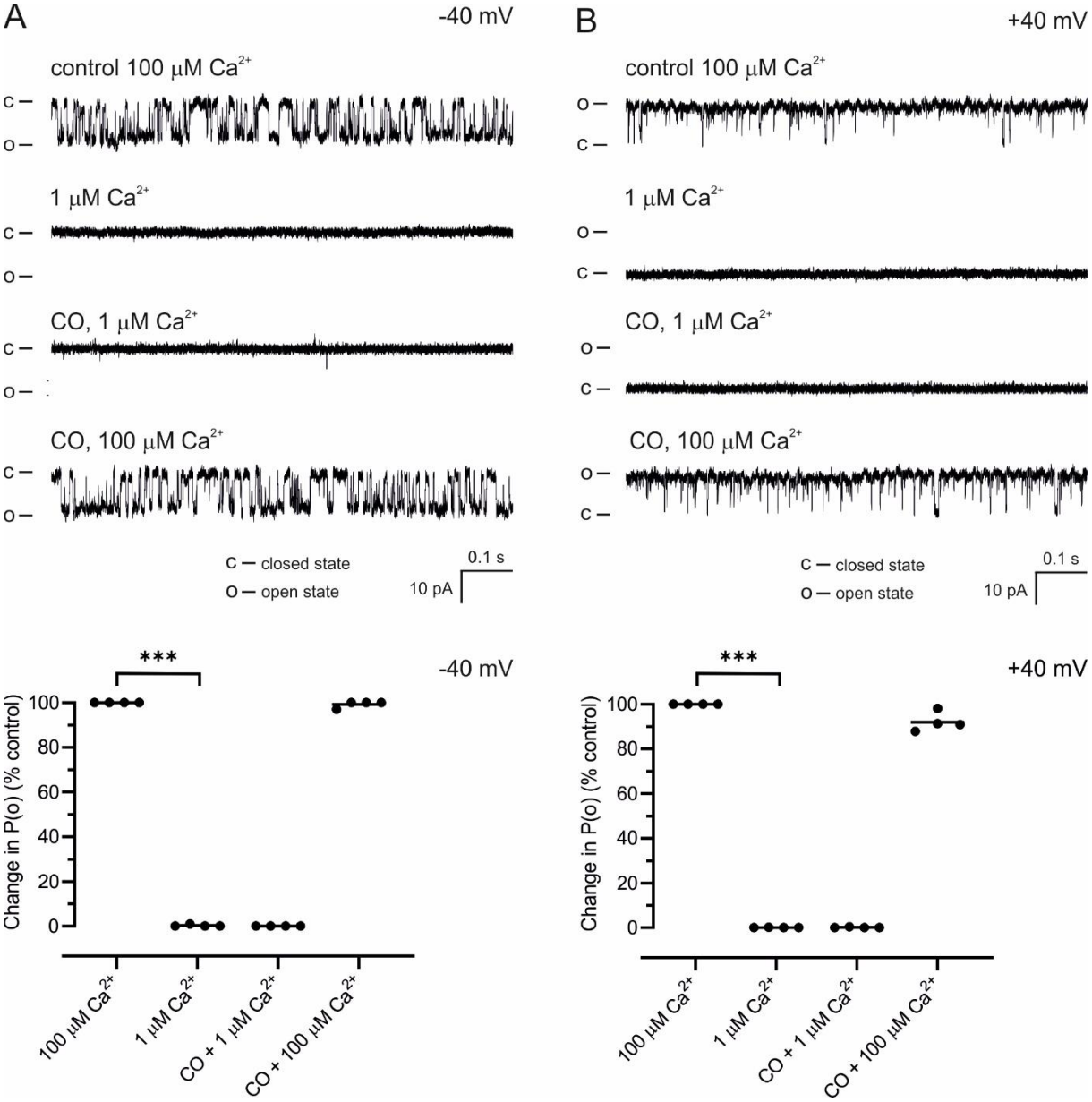

Figure 43. Absence of modulation of the mitoBK channels by CO gas alone. Representative traces of mitoBK single-channel recordings at -40 mV (A) and +40 mV (B) after perfusion with the symmetric 150/150 mM KCl solutions: the high-calcium control solution (100 μM Ca^{2+}), the low-calcium solution (1 μM Ca^{2+}), the low-calcium solution bubbled with CO, and the high-calcium solution bubbled with CO. Changes in the mean $P_{(o)}$ values upon perfusion with the low-calcium solution and the CO-containing solutions at -40 mV (A) and +40 mV (B) were evaluated for individual experiments.

6.5.3. Analysis of complex regulation of mitoBK channels by heme and CO gas

According to the existing data, heme is a primary CO-sensing element in proteins targeted by carbon monoxide [169], including BK channels. Although mitoBK channels have the heme-binding structural domain (HBD), heme and its oxidized form hemin appear to be only transiently bound to the channel. It is currently unknown what fraction of the mitoBK channel population comprises hemoproteins under physiological conditions. Thus, channel modulation by heme was modeled by the exogenous application of heme to the mitoBK channels in patches (Figure 44). Since heme was expected to inhibit the channel activity, the effects of heme application were studied in high-calcium solutions. Perfusion with 300 nM heme resulted in a decrease in the open channel probability to 52% ± 9%, compared to that of the control, at -40 mV (Figure 44A) and to 39% ± 6%, compared to that of the control, at +40 mV (Figure 44B) (n = 4).

To study whether the addition of CO could modify the inhibitory effect of heme on the mitoBK channels, the channels were perfused with a high-calcium solution containing both heme and carbon monoxide (Figure 44). The addition of CO resulted in the significant ($p < 0.05$) release of the channel inhibition by 300 nM heme - as indicated by the increase in the open channel probability from 40 % ± 13% to 77% ± 8% compared to that of the control at -40 mV, and from 25 % ± 11% to 83% ± 23% at +40 mV (n = 3).

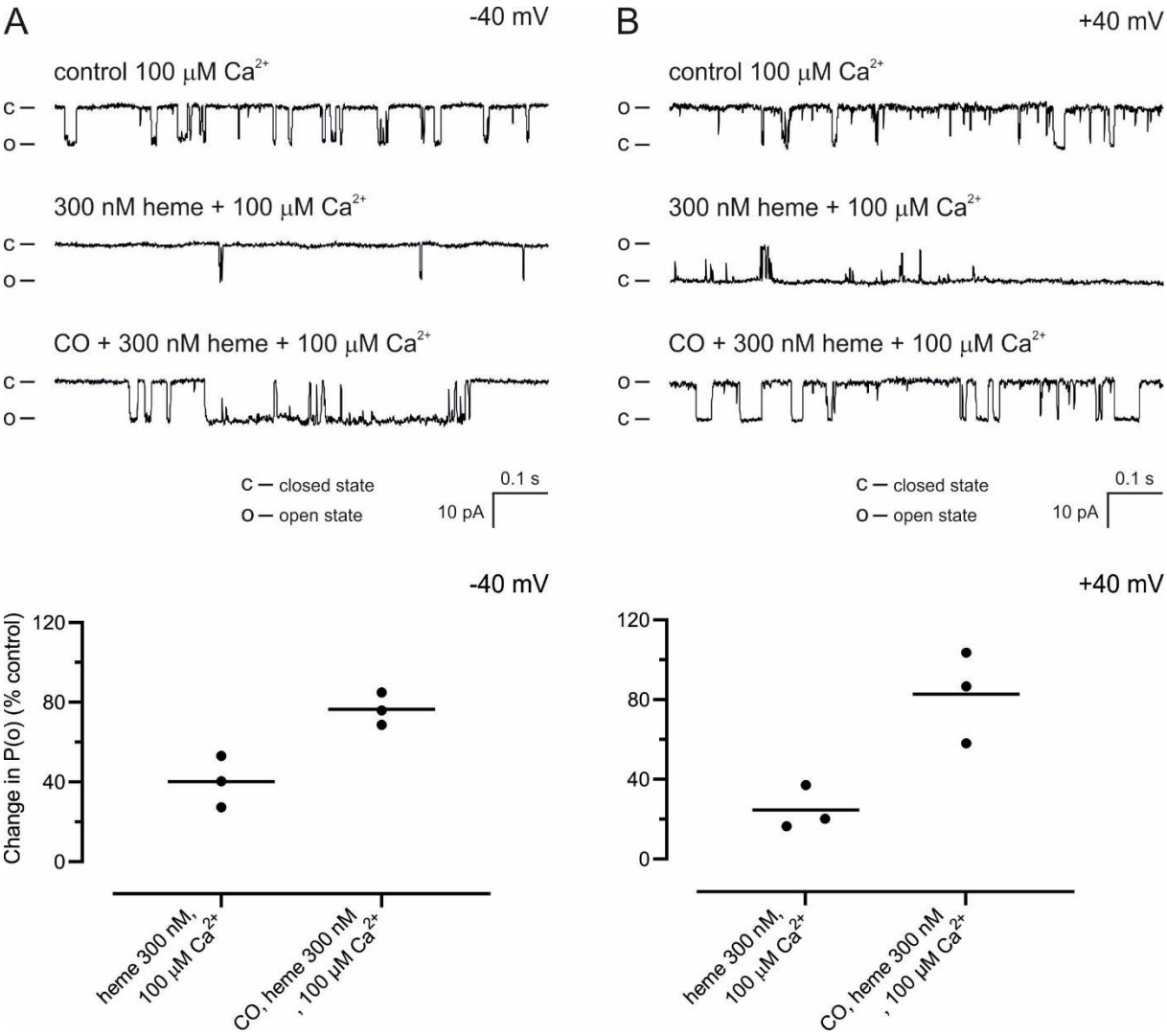

Figure 44. Reactivation of heme-inhibited mitoBK channels by CO gas. Representative traces of mitoBK single-channel recordings at -40 mV (A) and +40 mV (B) after perfusion with the symmetric 150/150 mM KCl solutions: the high-calcium control solution (100 μM Ca^{2+}), the high-calcium solution containing 300 nM heme, the CO-containing high-calcium solution containing 300 nM heme. Changes in the mean $P_{(o)}$ values upon perfusion with the heme, CO and heme, at -40 mV (A) and +40 mV (B) were evaluated for individual experiments.

It is well-established that CO binds only to the ferrous (Fe^{2+}) heme. In order to confirm the heme-mediated molecular mechanism of CO reactivation of the channels, mitoBK-containing patches were inhibited with the ferric (Fe^{3+}) form of heme – hemin. The subsequent perfusion of the channels with CO did not release the channel inhibition by hemin (Figure 45).

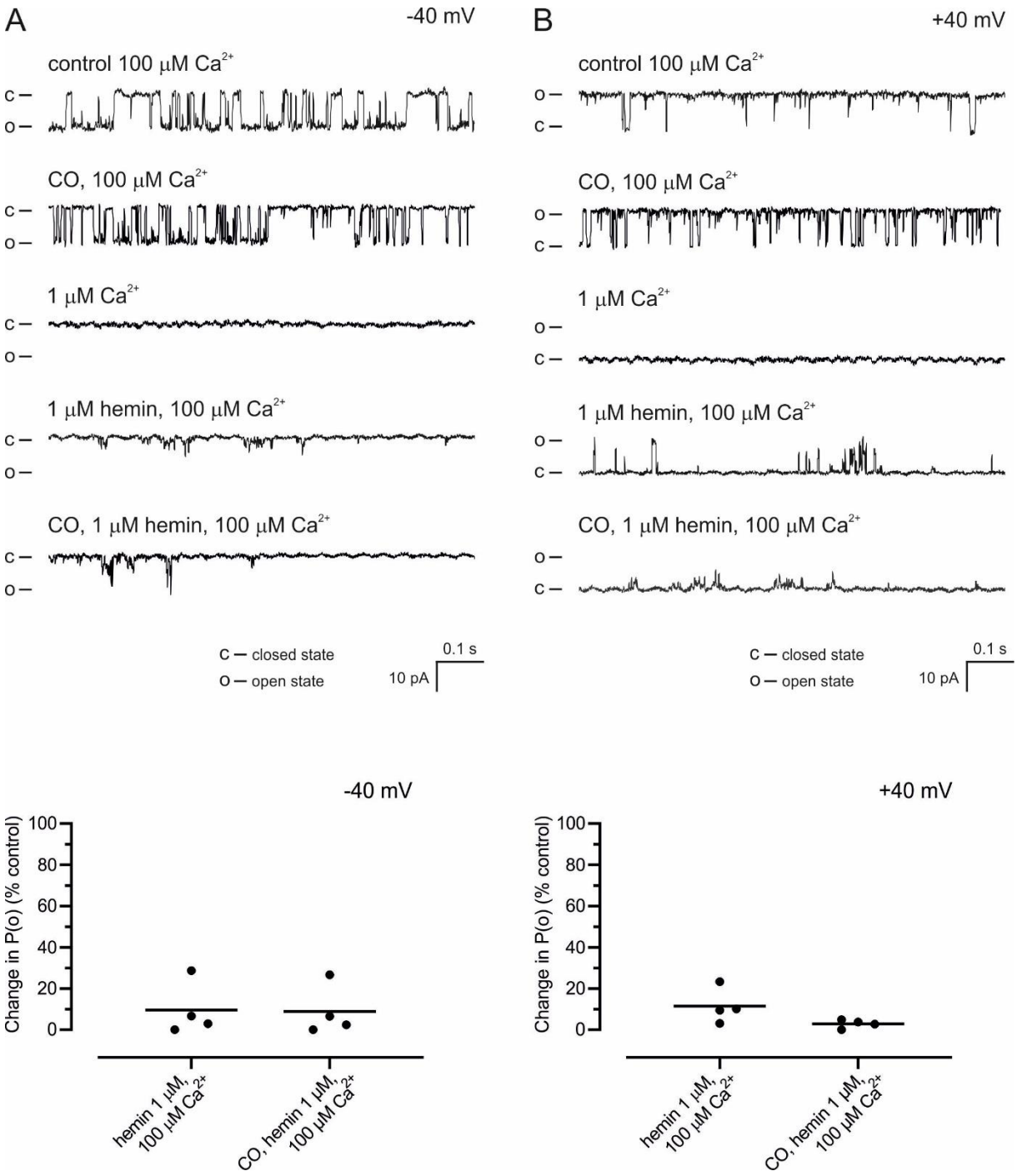

Figure 45. Lack of reactivation of hemin-inhibited mitoBK channels by CO gas. Representative traces of mitoBK single-channel recordings at -40 mV (A) and +40 mV (B) after perfusion with the symmetric 150/150 mM KCl solutions: the high-calcium control solution (100 μM Ca^{2+}), the high-calcium solution containing 100 μM CO, the low-calcium solution (1 μM Ca^{2+}), high-calcium solution containing 1 μM hemin, the CO-containing high-calcium solution containing 1 μM hemin. Changes in the mean $P_{(o)}$ values upon perfusion with the hemin, and CO with hemin, at -40 mV (A) and +40 mV (B) were evaluated for individual experiments.

7. DISCUSSION

The results presented in this work can be divided into four distinctive parts.

The first part investigates the effects caused by the depletion of mtDNA in astrocytoma cells on mitochondrial signaling. The retrograde signaling networks initiated by this mitochondrial dysfunction are evaluated. The particular focus of the study is dedicated to the transcriptional regulation of mitoBK channels.

The second part addresses the molecular functional effects of the deficiency of the smallest nuclear-encoded subunit of COX – COX8A – on the electron transport chain and cytochrome *c* oxidase in particular. The results are evaluated in the patient cells with a characterized mutation in COX8A and the HEK293T cells with functional COX8A deficiency introduced by CRISPR/Cas9 gene-editing technique.

The third part of this study is dedicated to the issue of the structural interaction of mitoBK channels with COX. In particular, the complexes between the mitoBK-α subunit and the COX are analyzed in the cell models with COX deficiency qualitatively and quantitatively.

The fourth part of this work is performed to elucidate the role of mitoBK channels in carbon monoxide (CO) signaling. The effects of various CO donors on the channel activity are compared to the modulation of the channels by a pure CO gas. The role of hemin binding in CO regulation of mitoBK channels is addressed in particular.

7.1. Signaling pathways activated upon mtDNA depletion in astrocytoma cells

Over the years, a large number of studies have explored the implication of mtDNA mutations in aging, neurodegenerative diseases [170], endocrine dysfunction [171], and cancer [172]. The accumulated oxidative damage to mtDNA has been suggested as one of the drivers of cellular aging [173]. Yet, high heterogeneity of mitochondrial diseases and various genetic backgrounds confound the application of the cells derived from patients as a study model to investigate the molecular role of mtDNA. Cell lines devoid of mtDNA with available maternal controls can be employed instead in different studies of the pathogenesis of mitochondrial diseases or

investigation of the fundamental mitochondrial physiology. Hence, several different approaches to obtain cell lines devoid of mtDNA or mtDNA-encoded proteins have been developed.

Treatment with ethidium bromide (EtBr) was one of the earliest characterized techniques for producing mtDNA-void cells. While it is still commonly used for this purpose, induction of mtDNA depletion with EtBr is either associated with a mutagenic effect on the nuclear DNA or has a very long duration that hampers its practicality. A different approach for the depletion of mtDNA involves overexpression of the products of fusion of EcoRI or ExoIII restriction endonucleases with the mitochondrial targeting sequence, such as the one of COX8A [174,175]. However, their overexpression is associated with concerns over occasional mistargeting to the nucleus and the ensued unintended endonuclease activity on the nuclear-encoded genes. In addition, targeting of these proteins to mitochondria can negatively affect the capacity of mitochondrial protein import systems for trafficking nuclear-encoded proteins, thus disrupting mitochondrial proteostasis. While another strategy is not inducing a deficiency in mtDNA sensu stricto, a commonly used approach in the proteomic studies investigating the effects of the lack of mitochondrial-encoded proteins relies on the inhibition of the mitochondrial protein synthesis with certain compounds. In particular, the bacteriostatic action of a number of antibiotics, e.g., chloramphenicol or tetracycline, is exerted by their binding to the bacterial ribosomes and blocking the binding of aminoacyl tRNA. Due to the structural similarity of mitochondrial ribosomes to the prokaryotic ones, these drugs were also shown to downregulate protein synthesis in mitochondria.

With the development of high-throughput sequencing technologies, a growing number of studies suggest a major role of functional impairments of the mitochondrial DNA polymerase γ (POLG) in mutagenesis of mtDNA. In particular, the mice mutator model that lacks the proofreading exonuclease activity of POLG, thus containing a higher number of mutations in their mtDNA, has a phenotype characterized by premature aging. Mutations in POLG are associated with disorders such as myoclonic epilepsy, ataxia neuropathy spectrum, autosomal recessive and autosomal dominant progressive external ophthalmoplegia, childhood myocerebrohepatopathy spectrum, and Alpers–Huttenlocher syndrome [176]. In this work, treatment of the cells with a non-hydrolyzable nucleoside analog 2′,3′-dideoxycytidine (ddC) as an inhibitor of POLG was selected to achieve depletion of mtDNA.

DdC has been extensively researched as a reverse transcriptase inhibitor, which was initially approved as antiretroviral treatment for HIV-infected patients. The therapeutic use of this compound was later suspended due to the reports of significant adverse effects including

peripheral neuropathy and myopathy, which were associated with the mitochondrial toxicity of ddC [177]. DdC is imported into the cells by nucleoside transporters hCNT1 and hENT2 and sequentially phosphorylated in the cytoplasm by nucleotide salvage route enzymes to form 2′,3′-dideoxycytidine triphosphate (ddCTP) [178]. Following the import of ddCTP into the mitochondria, it inhibits the mitochondrial DNA polymerase-γ (POLG). Importantly, the POLG is inhibited by ddCTP with a much higher affinity than the nuclear DNA polymerases α, β, and ε, with K_i of a 100 – 1000-fold higher value [153].

Induction of the mtDNA depletion can be fatal to the cells due to the lack of ATP synthesis by OXPHOS, yet the lack of precursors for pyrimidine salvage synthesis can further aggravate the damage to cell viability. The activity of an enzyme in the de novo pyrimidine biosynthesis pathway - dihydroorotate dehydrogenase - is inhibited due to the loss of ETC, with which it is linked through coenzyme Q. To compensate for it, the cell culture medium was supplemented with uridine, what is a commonly used approach to increase the viability of cultivated cells with various ETC deficiencies. Thus, while the growth of ddC-treated astrocytoma cells was stunted, due to their proclivity to glycolysis (as described above) they withstood this intervention in their metabolism.

In this study, the achievement of the depletion in mtDNA by the ddC treatment of astrocytoma cells was confirmed on different levels. Functionally, the abolished respiration of ddC-treated cells indicated a major loss of OXPHOS. On the protein level, a loss of the ETC complexes - in particular, complex IV, caused by the unavailability of the essential mtDNA-encoded subunits was confirmed. On the level of gene expression, the abundance of transcripts of all protein-coding mtDNA genes was significantly decreased. While this study did not address mitophagy in ddC-treated cells, the mitochondrial network was observed in mtDNA-depleted astrocytoma cells and appeared more disrupted than in the WT cells.

To investigate mtDNA depletion-initiated transcriptional regulation, the transcriptome of these cells was analyzed with a focus on mitochondrial retrograde signaling pathways. In particular, it was found that the expression of the genes under transcriptional control of integrated stress response (ISR) was upregulated. At the same time, no indications of activation of the mitochondrial unfolded protein response (mtUPR) were observed, what indicated that no proteotoxic stress signaling was elicited in a response to a disruption in proteostasis.

This observation is in agreement with the previous findings reporting initiation of ISR by deletions in mtDNA in different tissues. Thus, an increase in the transcription of the ISR master transcriptional regulator ATF4 was observed in the skeletal muscle of the mice harboring a

mutation in mtDNA helicase [179]. In the mice model of mtDNA-associated mitochondrial myopathy, induction of ISR was shown in myoblasts with particular involvement of fibroblast growth factor 21 (Fgf21) [180]. In another study of mitochondrial myopathy, Fgf21-mediated ISR was initiated only in response to mtDNA deletions or dysfunction in mitochondrial translation, and not in the myoblasts of patients with mitochondrial myopathy caused by the deficiencies in the nuclear-encoded structural ETC subunits or assembly factors [181]. However, Fgf-21-mediated signaling is likely specific to a tissue type since expression of Fgf21 was virtually undetectable in the RNA sequencing transcriptome profile of astrocytoma cells. Various triggers of ISR activation were described in a study where the ISR was induced by inhibiting ETC or ATP synthase activity in myoblasts and myotubes [182]. Following ETC inhibition, a disruption in aspartate synthesis activated kinase GCN2, whereas inhibition of the ATP synthase resulted in hyperpolarization of the IMM, which was implicated in the ISR signal relay.

Few studies have attempted to characterize the impact of mitochondrial retrograde signaling on the ion channels in the cell membrane and the IMM. Thus, another objective of this work was to investigate how the mitoBK channel is affected by the mitochondrial retrograde signaling in mtDNA-depleted astrocytoma cells. Analysis of expression of mitoBK-encoding genes has revealed that the amount of the *KCNMA1* transcripts was significantly downregulated in this cell model. The decrease in the transcript amount was also reflected in the decrease of the mitoBK-α protein complexes. To date, there has been no research demonstrating the decrease in the mitoBK-α on the transcriptional or protein level upon mitochondrial deficiencies. However, different studies demonstrated changes in the amount of BK channels under transcriptional regulations under various pathological conditions.

The disruption of transcription of genes involved in calcium homeostasis was identified in a transcriptome investigation of spinocerebellar ataxia type 7 (SCA7) mice suffering from cerebellar and retinal degeneration. In particular, downregulation of *Kcnma1* expression was observed, which was manifested in altered spiking patterns of Purkinje neurons. Furthermore, mitochondrial dysfunction was a major factor in SCA7 pathogenesis, as both mitochondrial morphology and oxidative metabolism were disrupted in the SCA7 mice model [166].

A decrease in the NAD^+ levels is a hallmark of mitochondrial disorders, and treatment with the precursors or stimulators of de novo NAD^+ synthesis has been a subject of extensive research towards therapy for mitochondrial dysfunctions [183,184]. Sirt-1 is a NAD^+ dependent deacetylase, and the low availability of its cofactor NAD^+ impairs the regulation of PGC-1α by Sirt1.

Kcnma1 contains PPAR response elements in the promotor region and is positively regulated by PGC-1α. Interestingly, Sirt1 overexpression, as well as NAD^+ supplementation, proved to have a neuroprotective effect in SCA7 mice [166,167]. Thus, the NAD^+-dependent deficiency in the *Kcnma1* could contribute to the mitochondrial pathology in SCA7. In the mtDNA-depleted astrocytoma cells, however, no change in the gene expression of PGC-1α and its downstream effectors was identified, suggesting that another mechanism is involved in the regulation of *KCNMA1* expression. It is likely that under the experimental conditions of this study, the NAD^+ pool was restored by the reduction of pyruvate to lactate in a reaction catalyzed by lactate dehydrogenase, the former being available due to its presence in the composition of DMEM in the cell culture medium.

One of the branches of the homeostatic responses in the mitochondrial retrograde signaling involves a cross-talk of the mitochondrial ISR with the nuclear factor erythroid-2–related factor 2 (Nrf2) signaling pathway, which is a master regulator of the oxidative stress response. Activation of Nrf2 leads to an upregulation of genes encoding proteins that confer antioxidant protection, including heme oxygenase-1 (HO-1), superoxide dismutase, thioredoxin, thioredoxin reductase 1, glutathione-disulfide reductase, glutathione translocase, and glutathione peroxidase. The results of this study suggest that Nrf2 was activated in the mtDNA-depleted cells and upregulated the expression of its target network of the antioxidant enzymes. Expression of *KCNMA1* was reported to be positively regulated by Nrf2 in the coronary smooth muscle cells [185]. However, the decrease in *KCNMA1* transcripts with a general upregulation of primary Nrf2 targets in ddC-treated cells suggests that a different regulatory mechanism is involved in mtDNA-depleted astrocytoma cells.

Besides regulation by transcription factors, other molecular mechanisms may be implicated in the control of *KCNMA1* expression in the mtDNA-depleted astrocytoma cells, but their study requires different methodological approaches from those used in this work. Thus, they will be only briefly outlined below:

- Different availability of the methyl group donor pool due to the alterations in the mitochondrial metabolic activity can affect the methylation of DNA. As a result, changes in the mtDNA levels can impact nuclear DNA methylation patterns across the genome [186]. In rat and human colorectal cancer cells, epigenetic control of BK channel expression, namely by hypermethylation of the *KCNMA1* promoter, was described [7].

- Histone remodeling by methylation or acetylation can be involved in epigenetic regulation. During mitochondrial stress, certain metabolic enzymes can be translocated from mitochondria to the nucleus - such as the pyruvate dehydrogenase complex, which then affects acetyl-CoA availability for histone acetylation [187]. A disruption in the methyl donor group supply can affect chromatin remodeling as well.

- Posttranscriptional RNA silencing by microRNA was implicated in the control of *KCNMA1* transcript amount in tumor cells: in particular, by mir-17-5p in colorectal cancer and pleural mesothelioma [188,189], mir-31 – in ovarian cancer [190], mir-211 – in melanoma cells [191].

- Regulation of splicing can be impaired by a decreased availability of ATP following disruption of its mitochondrial supply [192].

- Genomic instability is linked to mitochondrial depolarization, which impairs the synthesis of iron-sulfur clusters that are required as cofactors for the enzymes involved maintenance of genome integrity [193].

The amount of the functional BK channels regulated on the transcriptional level can be important in the pathophysiological context. While the role of mutations of BK channels in epilepsy is well-recognized, an acquired BK channelopathy caused by a decrease of the functional BK channels is emerging as a novel molecular mechanism that aggravates the disease. Thus, in a pilocarpine model of epilepsy, the amount of BK-α transcripts and proteins were decreased in the cortex and hippocampus of rats experiencing chronic seizures [194] . A decrease in vascular BK-β1 expression is observed in diabetes and at high-glucose culture conditions [195,196]. mRNA amount of BK-α subunits, as well as their protein amount, were decreased in the rat artery calcification models, and pharmacological activation of the channels diminished the severity of calcification [197]. In a study of the molecular mechanisms of neuropathic pain, the constriction of the spinal nerve led to a persistent transcriptional downregulation of the expression of BK channels, and a corresponding decrease in the protein amount of the BK channels in the dorsal root ganglion neurons of rats [198,199]. A release of brain-derived neurotrophic factor BDNF following nerve injury in rats was implicated in the transcriptional downregulation of BK-α in the primary sensory neurons, leading to aberrant cellular excitability and nociception [200].

One of the limitations of this study is that it is performed on a tumor cell line with its metabolic and signaling profile. Since not many cell types can sustain such a drastic change in their

metabolic pathways, a tumor cell line with typical metabolic lability and adaption to survival in hypoxic environments has been chosen. Distinct cancer types are characterized by different metabolic profiles, such as aerobic glycolysis phenotype, a phenotype with prevailing OXPHOS, or a combination of both, and they can be further altered throughout carcinogenesis and metastasis. However, metabolic lability of the cancer cells is pleiotropic, arising not only due to tumorigenic gene mutations but also from metabolic reprogramming to accommodate the unique metabolic requirements during tumor development. The modeled system is physiologically relevant since a change in the mtDNA copy number is implicated in malignant transformation and tumorigenesis. Thus, a decrease in the mtDNA copy number in colorectal and prostate cancer cells was associated with their metabolic reprogramming and increased cell invasiveness. MtDNA depletion that initiates metabolic reprogramming has been attributed to the start of epithelial-mesenchymal transition. The ensued activation of retrograde signaling pathways in epithelial cells led, in particular, to Ca^{2+}/calcineurin-dependent re-profiling with a decrease in epithelial markers and overexpression of mesenchymal markers [201].

In carcinogenesis, changes in the *KCNMA1* transcript and protein abundance are associated with tumor growth through different mechanisms. Downregulation of *KCNMA1* by siRNA gene silencing was observed in colorectal cancer, pleural mesothelioma, ovarian cancer, and melanoma [188–191]. However, in prostate cancer, amplification of chromosomal region 10q22 containing *KCNMA1* drew BK-α overexpression and increased current density, promoting the proliferation of PC-3 cells [202]. Similarly, amplification of *KCNMA1* and increase in protein expression were related to a poor prognosis and a high tumor stage and grade in breast cancer [203]. Expression of *KCNMA1* was shown as an early marker of cervical cancer [204].

In conclusion, treatment of astrocytoma cells with a POLG inhibitor ddC led to the depletion of mtDNA. This disruption in mitochondrial function initiated ISR signaling, and an associated branch of the transcriptional antioxidant response by Nrf2 was activated. The downregulation in the *KCNMA1* expression was identified as well. The observed link between the retrograde signaling in mtDNA-depleted astrocytoma cells and a change in *KCNMA1* expression leading to a decreased amount of mitoBK-α can be particularly interesting in the context of astrocytoma tumorigenesis. Further research can address open questions, such as whether the downregulation of the mitoBK-α is observed in the normal mtDNA-depleted cells, what molecular mechanisms are implicated in the regulation of this phenomenon, and how it is functionally relevant in the normal and pathophysiology.

7.2. Molecular and functional effects of the loss of cytochrome *c* oxidase subunit 8A

In the second part of the study, the consequences of the COX8A deficiency on the assembly of COX as a discrete respiratory chain constituent and a part of the ETC protein supercomplexes were evaluated.

The effects observed in the human dermal fibroblasts with an identified COX8A deficiency leading to a virtual loss of COX8A were evaluated alongside observations in the cellular systems of HEK293T cells with the CRISPR/Cas9-induced mutations in COX8A. A deficiency in COX8A was modeled with CRISPR/Cas9-mediated gene editing in HEK293T cells. *COX8A* exon 1 encoding a 25 amino acids-containing mitochondrial targeting sequence was targeted by the CRISPR/Cas9 system. Thus, two HEK293T cell lines containing deletions in the COX8A targeting sequence were generated. The protein amounts of selected COX subunits were compared with SDS-PAGE and BN-PAGE with subsequent Western blotting, followed by the measurement of enzymatic activities of COX. To identify whether the deficiency in COX8A affects the expression of OXPHOS complex subunits, or initiates mitochondrial retrograde signaling pathways, the transcriptome profiles were analyzed in the COX8A deficient cells.

To protect the mitochondria from exposure to the highly reactive intermediates, assembly of a COX holoenzyme proceeds in a strictly controlled manner involving numerous nuclear-encoded assembly factors [29]. The current modular model of COX assembly stipulates that COX8A is incorporated at the intermediate stage of COX assembly in the COX2-containing module [31]. Interestingly, recent data indicate that the biogenesis of COX as a component of respirasome occurs in a divergent pathway proceeding through non-canonical subassembly complexes [205].

In accordance with the previously reported data [152], the mutation in *COX8A* in the patient fibroblasts led to the nonsense-mediated mRNA decay resulting in a sharp decrease in *COX8A* transcript abundance. The functional evaluation has shown that the COX enzymatic activity levels in the patient fibroblasts were about 20% of the levels in the control cells. Correspondingly, the levels of COX activity in the HEK293 cell lines containing mutations in COX8A MTS were approaching 30% of the levels in the WT cells. These results suggest that the loss of COX8A is detrimental to the enzymatic activity of COX.

Analysis of protein complexes formed by COX has shown a significant decrease in the total amount of COX in the COX8A-deficient fibroblasts and HEK293T cells, which was corresponding to the observed decrease in the COX enzymatic activity. Notably, the BN-PAGE followed by immunodetection has shown a sharp decrease of the monomeric form of COX in the COX8A-deficient cells, while the residual COX was largely contained in the respirasomes. The downregulation of observable monomeric form of COX suggests that COX8A is involved in the stabilization of COX monomers. Interestingly, the residual COX as a constituent of respirasomes was not affected, suggesting that being contained within a SC could be shield a deficient COX protein complex from degradation. Considering the dramatic difference between the abundance of monomeric and respirasome-bound COX forms, and the recently reported data on alternative assembly pathways for COX incorporated into the respirasomes [205], this observation could indicate that COX8A is not strictly required for the biogenesis of COX as a part of respirasomes.

Stabilization of COX in the ETC supercomplexes and respirasomes has been reported for the cells harboring mutations in the nuclear-encoded COX assembly factors, such as COA6 and SURF1, while the stability and abundance of the monomeric form of COX were significantly affected in these cells [206,207]. In a similar manner, the stability of COX monomers was decreased in cells harboring a missense mutation of the nuclear-encoded structural subunit COX5A, while the levels of COX within the respirasomes were more robust [208]. Taken together, these observations support the hypothesis that the protein environment of respirasome provides additional stabilization and protection from protein degradation to the COX with an impaired assembly and diminished stability, which could constitute one of the main physiological roles of respirasomes [209].

Interestingly, the ETC complexes I and III were not imperiled in the COX8A-deficient cells, and on the contrary, their abundance appeared rather elevated. Similarly, a distinguishable increase in the amounts of ETC complexes I and III have been reported for the fibroblasts harboring mutations in COA6 and SURF1 [206,207]. Therefore, this phenomenon may occur as an adaptive event to provide higher compensatory availability of the protein partner complexes to stabilize the residual COX in the respirasomes.

The analysis of total protein levels of selected COX subunits by SDS-PAGE/immunoblotting has confirmed the decrease of the levels of all evaluated COX subunits – COX1, COX2, COX5A, COX4 – in the patient fibroblasts. In a similar manner, the amount of proteins of complex I and complex III was increased, corresponding to the observed increase in the amount

of corresponding complexes. To identify if the observed changes in the protein amount levels occur due to transcriptional upregulation, differential gene expression analysis by RNA sequencing was conducted.

No discernable pattern of changes in expression of genes encoding the OXPHOS proteins was observed in the fibroblasts containing the mutation in *COX8A*. The expression of certain mitochondrially-encoded genes such as ATP6, ATP8 and COX3 was downregulated. The statistically significant change in the gene expression affected subunits of COX contained in the 2nd (COX7B) and 3rd (COX3 and COX7A1) assembly module to a different extent. No systemic upregulation of the genes encoding proteins of complex I and III was detectable. Therefore, these observations suggest that the molecular events controlling the abundance of ETC proteins in the COX8A-deficient fibroblasts occur at the post-transcriptional level. Interestingly, in the COX8A-deficient HEK293 cells different regulatory events have occurred: the increase of expression of almost all mitochondrially-encoded proteins was prominent, combined with the decrease of multiple nuclear-encoded COX subunits contained in each COX assembly module.

To identify whether the mutation in *COX8A* led to proteotoxic stress in mitochondria due to the buildup of the misassembled COX intermediates, the transcriptome was analyzed for the hallmarks of mtUPR activation. The mechanisms of restoring protein homeostasis by mtUPR signaling involve an increase in the expression of mitochondrial quality control proteases, such as YME1L, ClpP, ClpX, and Lonp1 [120]. Analysis of gene expression has shown a lack of upregulation of mitochondrial proteases in COX8A-deficient fibroblasts and HEK293T cells. On the other hand, mtUPR signaling pathways increase the availability of the mitochondrial chaperone pool to aid in folding the mitochondrial peptides [109]. Upregulation of mitochondrial chaperone expression observed in the COX8A-deficient HEK293T cells could, however, be ascribed to the increased transcription of mitochondrial genes requiring a higher abundance of mitochondrial chaperones to assist in the folding of a larger peptide pool. No increase in the expression of genes encoding mitochondrial chaperones was observed in COX8A-deficient fibroblasts.

To investigate whether the COX deficiency induced by the mutations in COX8A triggers the mitochondrial dysfunction-associated retrograde signaling pathways such as ISR, the expression of the downstream targets of the master transcriptional regulator of ISR – ATF4 - was analyzed [210,211]. Combined, the observed absence of activation of ISR and mtUPR in COX8A-deficient fibroblasts and HEK293T cells indicates that there is likely no underlying

deleterious accumulation of orphaned misassembled COX intermediates, suggesting that an efficient turnover of COX subassemblies takes places. Considering the occurrence of the alternative COX assembly pathways as a part of the respirasomes, the COX intermediates lacking COX8A could alternatively be incorporated into the respirasomes and stabilized in the multiprotein complexes.

Therefore, the role of COX8A suggested in the observations on the COX8A-deficient cells is to stabilize the COX monomers. The deficiency in COX8A is detrimental to COX resulting in the loss of the protein stability, and therefore its abundance and enzymatic activity. However, the remaining COX can be salvaged as a part of respirasome complexes, thus avoiding the potential proteotoxic accumulation of the misassembled intermediates. Additionally, a compensative increase of availability of the ETC protein partners occurs likely to promote stabilization of the residual COX in COX8A-deficient cells.

7.3. Interaction of the mitoBK channel with the cytochrome *c* oxidase

In the third part of the study, the structural interaction of mitoBK channels with COX was evaluated with BN-PAGE using mitochondrial isolations of the WT and mtDNA-depleted astrocytoma cells, as well as fibroblasts from a patient harboring a genetic deficiency in *COX8A* and a matching control.

The results of this study suggest that in astrocytoma mitochondria mitoBK channel forms a structural complex with the ETC through an interaction of the mitoBK-α subunits with COX. In the mtDNA-depleted cells, the higher-order complexes between mitoBK-α and COX within respirasomes are not observed, and the abundance of the mitoBK channel complexes corresponding to a fully assembled tetramer of mitoBK-α subunits associated with mitoBK-β subunits is significantly decreased. A similar downregulation of the mitoBK channel complex amount is observed in the fibroblasts with a COX deficiency due to the mutation in COX8A.

These results are in alignment with the previously reported structural and functional coupling of mitoBK channels with COX through the mitoBK-β4 subunits. In a previous patch-clamp study of the functional interaction between mitoBK channels and protein complexes of the respiratory chain of astrocytoma mitochondria, it was shown that mitoBK channel activity was inhibited after the addition of the respiratory substrates [104]. Notably, this effect persisted after the removal of the respiratory substrates and was abolished by the addition of the specific inhibitors of the respiratory complexes. Therefore, it was suggested that the activity of the mitoBK complexes is regulated by the redox status of the respiratory chain. Structural interaction between cytochrome *c* oxidase and the auxiliary mitoBK-β4 subunit has been suggested to mediate the functional coupling. An interaction of another mitoBK-β subunit – mitoBK-β1 – with COX1 has been shown in a yeast two-hybrid screening in cardiac myocytes [105]. In the current study, however, the role of mitoBK-α in the mitoBK-COX interaction is confirmed directly with the BN-PAGE technique. In particular, the results presented here indicate that mitoBK channels are associated with COX in the respirasomes, thus forming a multiprotein complex of a higher order. At the same time, the results presented in this work are in agreement with the identification of mitoBK-β4 as the most commonly expressed auxiliary mitoBK-β subunit in astrocytoma cells [104].

A proteomic study of the protein interactome of mitoBK channels expressed in the HEK293T cell line has identified 151 mitochondrial protein partners [82]. Among them, 28 OXPHOS proteins of complexes I, III, IV, and V were found, which would agree with the finding of a

mitoBK channel population in a respirasome-associated state. The subunits of COX reported in the interaction of mitoBK channels – COX1, COX4, COX7A2, COX6A2, COX6C – comprise the subunits of all COX assembly models. Notably, one of these subunits, COX7A2, has a high degree of structural similarity in the C-terminal region with COX7A2L, which is directly involved in the stabilization of respirasomes.

Some of the key physiological functions of the mitoBK channels are mediated through their influence on the activity of ETC. The respiratory chain complexes and mitoBK channels execute opposite regulation of the mitochondrial membrane potential: the activity of the RC generates it, while mitoBK opening dissipates it. Thus, an open question is the localization of the complexes of mitoBK channels with the respirasomes within the IMM. From a biophysical perspective, the curvature of IMM affects charge density and local pH. The strength of the electrostatic field is the highest in the membrane segments with the highest curvature: in a simulation of the electric field on the surface of IMM, the surface charge density in the curved segments of cristae was evaluated to be 3.5 times higher compared to the straight segments [212]. Thus, the local biophysical regulation of ETC by a mitoBK channel opening within immediate proximity would have a different impact in this environment.

Evidence of functional networks linking bioenergetics and various mitochondrial processes through a physical interaction with the respiratory chain complexes has been shown in the previous studies. Thus, interaction between the protein import system and the respiratory chain was shown by the physical contact between an ETC supercomplex $CIII_2$ + CIV with the TIM23 protein translocase complex [213,214]. A formation of supramolecular complexes has been reported for OXPHOS complexes and IMM transport proteins, such as between COX and adenine nucleotide transporter (ANT) in yeast mitochondria, and LDH and monocarboxylate transporters MCT1 and MCT2 in rat neurons [215]. Another interesting question is whether a functional protein module of a higher order can be formed. In particular, the interaction of mitoBK with ANT through VEDEC terminal motif was shown [82]. Exploring whether mitoBK can interact with both respirasomes and ANT would be an interesting challenge.

In a study of the molecular mechanisms of ataxia in cells harboring a mutation in the *KCNMA1* BK_{G354S} that impaired channel gating, the amount of the subunits CORE2 of complex III, COX2 of complex V, NDUFB8 of complex I was negatively affected [216]. On the other side, no link between the observed decreased amount of mitoBK-α and the structural impairment of COX has been reported to date. A phenomenon of the decrease in the amount of mitoBK-α-formed complexes could be explained on several levels. Firstly, *KCNMA1* was transcriptionally

downregulated in mtDNA-depleted cells. However, no significant decrease in the *KCNMA1* transcript amount was observed in COX8A-deficient fibroblasts. Secondly, a lack of functional ETC in the mtDNA-depleted cells, as well as the impairment in COX activity in COX8A-deficient cells, can lead to the loss of the mitochondrial potential. Therefore, the electrogenic mitochondrial protein import into the IMM through the TOM/TIM complexes can be hindered. However, the BN-PAGE results in the mtDNA-depleted cell indicated that while various IMM protein complexes were affected, the extent of their downregulation was different. In particular, the import of another IMM ion channel – the MCU complex – appeared to be affected to a lesser degree. Thirdly, protein turnover can be higher in mitochondria with functional impairments. Yet, no indication of transcriptional upregulation of mitochondrial proteases in both mtDNA-depleted cells and COX8A-deficient fibroblasts was observed. Fourthly, a molecular mechanism targeting mitoBK channel subunits to mitochondria could be affected by the deficiencies in ETC or COX in particular.

7.4. Mechanisms of modulation of mitoBK channels by the CO and heme signaling

Due to the abundance of the heme proteins, as well as the presence of the enzymes indispensable in the heme biosynthesis, mitochondria are one of the major key targets of the CO signaling pathways [141]. Similar to plasma membrane BK channels, mitoBK channels possess the heme-binding domain and have been shown to be inhibited by hemin [129]. However, the modulation of mitoBK channels by CO has not been extensively studied. The CORMs are widely used as a CO delivery tool to study its biological effects. Considering the growing number of the data reporting discrepant molecular mechanisms of plasma membrane BK channel modulation by CO that were obtained with the use of CORMS [138,217,218], as well as recent reports highlighting pleiotropic effects of CORMs in different biological systems [140,156,219], the effects of three structurally different CORMs on the mitoBK channel activity were compared to the application of the CO gas in the present study.

A fast CO releaser CORM-2 containing a ruthenium moiety has been one of the most widely used tools for studying the CO effects in vitro [220,221]. Notably, a recent report has identified that CORM-2 is prone to form an adduct in a reaction with histidine [156]. Moreover, activation of the plasma BK channels by CORM-2 was substantially diminished by the external addition of histidine. In a study of the modulation of Kv2.1 channels by CORM-2, the inhibitory action of this compound was similar to the effect on the channels observed after the CO application [222]. However, the effects of CORM-2 on the mitoBK channels could not be reproduced by the application of the CO and therefore cannot be further attributed to the activity of the CO gas released by this delivery vehicle. Specifically, CORM-2 exerted two types of effects on mitoBK channels: transient activation followed by inhibition, or direct inhibition of the channel activity. Such a phenomenon could be explained by heterogeneity of mitoBK channels: due to the various alternatively spliced mitoBK-α subunits that can localize in mitochondria, or protein complexes of mitoBK with other proteins in IMM, including the respiratory chain [104,106]. Different interactions of CORM-2 with the histidine residues of mitoBK subunits or its protein partners in the IMM with high protein density could be responsible for pleiotropic mechanisms of mitoBK modulation by CORM-2.

A structurally different slow releaser CORM studied in the context of mitoBK modulation is a manganese–containing CORM-401 [223]. Previously, direct activation of mitoBK channels in EA.hy926 cells after application of CORM-401 was reported [137]. CORM-401 exerted

multimodal modulation of mitochondrial function, affecting respiration, generation of ATP, and proton uncoupling. Interestingly, in the current study application of CORM-401 in a similar experimental setting has not induced an observable modulation in the mitoBK channel activity in astrocytoma cells. In a similar manner, while CORM-401 has increased the respiration of microglial cells, mitoBK channels were not involved in this effect [224]. However, it should be noted that the mitoBK channels in these cell types are comprised of different auxiliary beta-subunits: BK-β2 subunit in the endothelial cells [67], BK-β3 subunit in the microglial cells [225], and mostly BK-β4 in the astrocytoma mitochondria. Thus, the different structural compositions of mitoBK channels could underlie the variations in its pharmacological modulation by CORM-401. Notably, CORM-401 has displayed CO-independent effects in a study on *E. coli*, having an uncoupling effect and stimulating bacterial respiration [219].

Next, the effects of a slow CO-releaser CORM-A1 containing sodium boranocarbonate on the mitoBK channels were analyzed. While CORM-A1 does not contain a transition metal ion in its structure, and therefore, could be less likely to have a CO-independent biological activity, it hasn't been widely studied in the context of modulation of potassium ion channels. In this work, perfusion of a patch with a CORM-A1-containing solution did not affect mitoBK channel activity. In a study where structurally different CORMs were administered in the endothelial cellular model of oxidative stress, CORM-2 and CORM-A1 had different molecular mechanisms of the antioxidative effects - in particular, CORM-A1 did not modulate the generation of ROS in mitochondria [226,227]. While these compounds have different water solubility, the released CO molecules easily traverse mitochondrial membranes by diffusion. Thus, the differences in the biological effects between CORM-A1 and CORM-2 are at least in part caused by the activity of their metal complex-containing cores.

Therefore, caution should be exercised when CORMs are used a tool for the study of the biological properties of CO. The process of the release of CO by CORMs involves a stepwise degradation with a formation of intermediate or final degradation products with a variable number of carbonyls substituted with water or DMSO, which could possess different biological activities. However, since the aim of the current study was to identify whether endogenous CO modulates the activity of the mitoBK channel, the molecular mechanisms of the diverse effects (or lack thereof) of structurally different CORMs is outside the scope of this work.

To identify the direct effects of the CO application to mitoBK channels, the patches containing these channels were perfused with a solution saturated in the CO gas. No change in the channel activity was observed after direct application of CO, endorsing the previously reported concept

that BK channels require prior binding of heme for the CO modulation [157]. Specifically, as most isoforms of pore-forming mitoBK-α subunits encoded by *KCNMA1* contain the C-terminal structural motif -CXXCH- between the two RCK domains, mitoBK channels can bind heme, similar to the plasma membrane BK channels.

Heme is distributed between two cellular pools: a fraction bound to the so-called "housekeeping" heme proteins (including cytochrome *c* oxidase, hemoglobin, peroxidases, etc.), and a smaller "labile" pool of heme acting as a signaling mediator [228]. Heme *c* is covalently bound to COX via thioether bonds between the heme and Cys residues within the HBD [229]. In contrast, plasma membrane BK channels interact with heme *b*, and the binding of CO to mitoBK channels would be an event of the transient and reversible nature [127]. Binding of heme modifies the gating ring confirmation, thus disrupting the Ca^{2+} and voltage gating, and inhibiting the channel activity. A functional proof of the inhibition of the mitoBK channels by the oxidized heme – hemin – has been previously obtained [155]. Inhibition of mitoBK channels by heme reported in the present work supports the notion that mitoBK channels possess HBD and are modulated by binding heme or hemin.

Hemin is a metalloporphyrin containing a ferric Fe^{3+} atom, which cannot bind CO. In this study, inhibition of the mitoBK channel activity with hemin could not be released with CO. However, application of CO after the perfusion of the channels with the ferrous Fe^{2+} heme has released the channel inhibition. This functional observation confirms that heme is a receptor for the CO action in the mitoBK channels, acting in a similar manner to the observations reported on the plasma membrane BK channels [157]. Notably, heme and CO signaling pathways target K_{ATP} ion channels by an equivalent molecular mechanism: the channel comprised of Kir6.2 and SUR2A is activated by CO exclusively following the binding of heme to the SUR2A subunit [230].

Several interesting other open questions arise from this observation. A presence of the Cys thiol-disulfide switch has been reported within the HBD of the plasma membrane BK channels, which regulates the affinity of the channels to heme in a redox-sensitive manner [231]. Whether this structural element is present in mitoBK remains to be identified, however, its presence could introduce another dimension to the heme/CO signaling in the context of mitochondrial redox signaling functions.

Heme turnover is a regulated process, as in the free form it is a highly reactive molecule. The iron bound to porphyrin is involved in pathophysiological processes due to its role in the generation of the reactive oxygen species – specifically, the synthesis of hydroxyl radicals in the Fenton reaction [232]. Heme oxygenase is a crucial enzyme in heme catabolism, acting as one

of the cytoprotective proteins in the events of ischemia-reperfusion injury. Following the elimination of heme by heme oxygenases, CO, Fe^{2+}, and bilirubin are produced. Interestingly, it was shown that plasma membrane BK channels and HO-2 co-localize in the plasma membrane, forming a multiprotein signaling unit [233]. Interaction of the mitoBK channels with CO can be regulated by the local synthesis of CO in mitochondria by the HO-1, which can translocate to this organelle [234]. The expression of heme oxygenase 1 is induced by the oxidative stress signaling, in particular, in the mtDNA-depleted astrocytoma cells, and can be linked to the ROS synthesis following the mitochondrial dysfunction. Therefore, degradation of heme by the mitochondrial HO-1 decreases the available pool of heme and produces CO. A resulting higher activation of the mitoBK channels thus provides feedback control of generation of ROS in mitochondria, what could be particularly relevant in the cytoprotective signaling conferred by the mitoBK channel activation.

An additional layer of regulation of the mitoBK channel by the CO is conferred by the downstream effects of activation of other molecular targets of this mediator, such as increased synthesis of cGMP following the activation of guanylyl cyclase by CO [235]. An observation of the increased activity of mitoBK channels after addition of cGMP together with a protein kinase G further supports an activatory role of CO on these channels [125].

8. CONCLUSIONS AND SUMMARY

I. In human astrocytoma cells and dermal fibroblasts, the expression of genes encoding mitoBK channel subunits – *KCNMA1, KCNMB3, KCNMB4* – as well as translated proteins localized to the mitochondria was confirmed. The mitoBK channel activity in mitoplasts of astrocytoma cells was characterized on the single-channel level.

II. The pore-forming mitoBK-α subunit interacts with the cytochrome *c* oxidase (COX) and can be a part of the respiratory chain supercomplexes in astrocytoma mitochondria. Depletion of mtDNA triggers the integrated stress response (ISR) signaling in the human astrocytoma cells.

1. A cell line devoid of mtDNA was developed by the treatment of human astrocytoma cells with 2′,3′-dideoxycytidine (ddC). A sharp decrease in the amount of transcripts encoded by the mtDNA was observed, alongside the absence of the properly formed multiprotein complexes of the electron transport chain. On the functional level, the depletion of mtDNA was confirmed by the abolishment of respiration of these cells.
2. The interaction of the pore-forming mitoBK-α subunit with the COX in mitochondria of the human astrocytoma cells occurs on the level of the respiratory chain supercomplexes.
3. The amount of the complexes formed by the mitoBK-α subunit, as well as its total protein amount was significantly downregulated in the mtDNA-depleted astrocytoma cells. A downregulation of the expression of *KCNMA1* was observed.
4. About 5% of genes were differentially expressed in the mtDNA-depleted cells. The depletion of mtDNA initiated the ISR. In addition, the transcriptional upregulation of the antioxidant enzymatic functional network under the common transcriptional control by Nrf2 occurred.

III. The nuclear-encoded COX subunit COX8A is required for the maintenance of the structural stability of COX. The loss of COX8A leads to COX deficiency, which is manifested by the reduced amount of COX protein complexes and a decrease in its enzymatic activity. The residual COX in the COX8A-deficient cells is stabilized within the respirasomes, and ISR or mtUPR caused by the misassembled intermediates of the COX monomer does not occur.

1. The protein amount of all evaluated COX subunits was decreased in the COX8A-deficient fibroblasts. The residual COX was stabilized in the respirasomes.

2. Induction of the COX8A deficiency in HEK293T cells by CRISPR/Cas9 generated two clonal cell lines with mutations in *COX8A*, each containing in-frame deletions affecting the mitochondrial targeting sequence in one allele, and frameshift mutations in another one. The protein amount of COX subunits amount was decreased in both cell lines. In the cell line with a larger deletion of the COX8A mitochondrial targeting sequence, the residual COX was stabilized largely in the respirasomes.
3. No evidence of the ISR or mitochondrial unfolded protein response signaling was observed in the transcriptome of both COX8A-deficient cell lines.
4. In the COX8A-deficient fibroblasts, the amount of the protein complexes formed by the mitoBK-α subunits was decreased, yet it was not regulated on the transcriptional level.

IV. CO activates mitoBK channels in astrocytoma cells, however, prior heme binding to mitoBK is required as a receptor for the CO action.

1. In a study of the regulation of mitoBK channel activity by CO, the effects of different CORMs did not necessarily replicate those of the CO gas applied to mitoBK channels in astrocytoma mitochondria.
2. Application of heme and hemin inhibited mitoBK channel activity.
3. No effect of the CO gas applied alone was observed on the mitoBK channel activity, despite a known interaction of CO with the COX.
4. Following the inhibition of the mitoBK channels with heme, the application of CO reactivated mitoBK channel activity.

9. LIST OF PUBLICATIONS

The results included in the thesis are presented in the following publications:

- **Rotko D**., Kudin A. P., Zsurka G., Kulawiak B., Szewczyk A., Kunz W. S. (2021). Molecular and functional effects of loss of cytochrome *c* oxidase subunit 8A. *Biochemistry (Moscow)*, 86(1), 33-43.
- **Rotko D**., Bednarczyk P., Koprowski P., Kunz W. S., Szewczyk A., Kulawiak B. (2020). Heme is required for carbon monoxide activation of mitochondrial BK_{Ca} channel. *European Journal of Pharmacology*, 173191.
- Augustynek B., Koprowski P., **Rotko D**., Kunz W. S., Szewczyk A., Kulawiak B. (2018). Mitochondrial BK channel openers CGS7181 and CGS7184 exhibit cytotoxic properties. *International journal of molecular sciences*, 19(2), 353.
- **Rotko D**., Kunz W. S., Szewczyk A., Kulawiak B. (2020). Signaling pathways targeting mitochondrial potassium channels. *The international journal of biochemistry & cell biology*, 105792. (Review paper)

The additional author's publications include:

- Szewczyk A., Bednarczyk P., Jędraszko J., Kampa R.P., Koprowski P., Krajewska M., Kucman S., Kulawiak B., Laskowski M., **Rotko D**., Sęk A., Walewska A., Żochowska M., Wrzosek A. (2018). Mitochondrial potassium channels - an overview. *Postępy biochemii*, 64(3): 196-212.

The results were disseminated at the scientific meetings as oral presentations:

- 9th Mitochondrion Conference, Poland, January 2021: RNA sequencing analysis of transcriptome changes upon mtDNA depletion with the focus on potassium ion channels.
- Rheinland Redox Research Meeting, Cologne, Germany, March 2019: Interaction of mitochondrial BK_{Ca} channel with cytochrome *c* oxidase.
- FEBS3+ Meeting – XI Parnas Conference, Kyiv, Ukraine, September 2018: Mitochondrial potassium channels and carbon monoxide signaling.
- 6th Mitochondrion Conference, Poznań, Poland, December 2017: Diverse pharmacological effects of carbon-monoxide releasing molecules on mitochondrial BK channel.

The poster presentations were made at the following international conferences:

- Rotko D., Kulawiak B., Kunz W. S., Szewczyk A. (2018). Role of subunit COX8A in biogenesis of cytochrome *c* oxidase in human fibroblasts. *Biochimica et Biophysica Acta (BBA) – Bioenergetics*, 1859: e71-e72. 20th European Bioenergetics Conference, Budapest, Hungary, 2018.
- Rotko D., Kulawiak B., Kunz W. S., Szewczyk A. (2018). Organization of respiratory chain in human fibroblasts with cytochrome *c* oxidase deficiency caused by loss of COX8A subunit. *FEBS Open Bio*, 8: P.09-037. 43rd FEBS Congress and FEBS Young Scientist Forum, Prague, Czech Republic, 2018.
- Rotko D., Bednarczyk P., Szewczyk A. (2018). Diverse pharmacological effects of carbon monoxide-releasing molecules on mitochondrial BK channel. *Biophysical Journal*, 114(3), 488a. 62nd Annual Meeting of Biophysical Society, San Francisco, USA, 2018.
- Rotko D., Bednarczyk P., Koprowski P., Szewczyk A. (2016). "New properties of the mitochondrial large-conductance Ca2+-activated K+ channel from astrocytoma mitochondria". *Biochimica et Biophysica Acta (BBA) – Bioenergetics*, 1857: e70-e71. 19th European Bioenergetics Conference, Riva del Garda, Italy, 2016.

10. REFERENCES

1. Roger AJ, Muñoz-Gómez SA, Kamikawa R. The Origin and Diversification of Mitochondria. *Curr Biol*. 2017;27(21):R1177-R1192. doi:10.1016/j.cub.2017.09.015

2. Gray MW. Mosaic nature of the mitochondrial proteome: Implications for the origin and evolution of mitochondria. *Proc Natl Acad Sci U S A*. 2015;112(33):10133-10138. doi:10.1073/pnas.1421379112

3. Wallace DC. Bioenergetics, the origins of complexity, and the ascent of man. *Proc Natl Acad Sci U S A*. 2010;107(SUPPL. 2):8947-8953. doi:10.1073/pnas.0914635107

4. Muñoz-Gómez SA, Wideman JG, Roger AJ, Slamovits CH, Agashe D. The origin of mitochondrial cristae from alphaproteobacteria. *Mol Biol Evol*. 2017;34(4):943-956. doi:10.1093/molbev/msw298

5. Martin W, Russell MJ. On the origin of biochemistry at an alkaline hydrothermal vent. *Philos Trans R Soc Lond B Biol Sci*. 2007;362(1486):1887-1925. doi:10.1098/RSTB.2006.1881

6. Mailloux RJ. An update on mitochondrial reactive oxygen species production. *Antioxidants*. 2020;9(6):472. doi:10.3390/antiox9060472

7. Embley TM, Martin W. Eukaryotic evolution, changes and challenges. *Nat 2006 4407084*. 2006;440(7084):623-630. doi:10.1038/nature04546

8. Calvo SE, Clauser KR, Mootha VK. MitoCarta2.0: An updated inventory of mammalian mitochondrial proteins. *Nucleic Acids Res*. 2016;44(D1):D1251-D1257. doi:10.1093/nar/gkv1003

9. Kulawiak B, Höpker J, Gebert M, Guiard B, Wiedemann N, Gebert N. The mitochondrial protein import machinery has multiple connections to the respiratory chain. *Biochim Biophys Acta - Bioenerg*. 2013;1827(5):612-626. doi:10.1016/j.bbabio.2012.12.004

10. Vögtle FN, Wortelkamp S, Zahedi RP, et al. Global Analysis of the Mitochondrial N-Proteome Identifies a Processing Peptidase Critical for Protein Stability. *Cell*. 2009;139(2):428-439. doi:10.1016/j.cell.2009.07.045

11. Letts JA, Fiedorczuk K, Sazanov LA. The architecture of respiratory supercomplexes. *Nature*. 2016;537(7622):644-648. doi:10.1038/nature19774

12. Barros MH, McStay GP. Modular biogenesis of mitochondrial respiratory complexes. *Mitochondrion*. 2020;50(October 2019):94-114. doi:10.1016/j.mito.2019.10.008

13. Hackenbrock CR, Chazotte B, Gupte SS. The random collision model and a critical assessment of diffusion and collision in mitochondrial electron transport. *J Bioenerg Biomembr*. 1986;18(5):331-368. doi:10.1007/BF00743010

14. Schägger H, Pfeiffer K. The Ratio of Oxidative Phosphorylation Complexes I-V in Bovine Heart Mitochondria and the Composition of Respiratory Chain Supercomplexes. *J Biol Chem*. 2001;276(41):37861-37867. doi:10.1074/jbc.M106474200

15. Greggio C, Jha P, Kulkarni SS, et al. Enhanced Respiratory Chain Supercomplex Formation in Response to Exercise in Human Skeletal Muscle. *Cell Metab*. 2017;25(2):301-311. doi:10.1016/j.cmet.2016.11.004

16. Gu J, Wu M, Guo R, et al. The architecture of the mammalian respirasome. *Nature*. 2016;537(7622):639-643. doi:10.1038/nature19359

17. Sousa JS, Mills DJ, Vonck J, Kühlbrandt W. Functional asymmetry and electron flow in the bovine respirasome. *Elife*. 2016;5(NOVEMBER2016). doi:10.7554/eLife.21290

18. Cogliati S, Frezza C, Soriano ME, et al. Mitochondrial cristae shape determines respiratory chain supercomplexes assembly and respiratory efficiency. *Cell*. 2013;155(1):160-171. doi:10.1016/J.CELL.2013.08.032

19. Hirst J. Open questions: Respiratory chain supercomplexes-why are they there and what do they do? *BMC Biol*. 2018;16(1):5-8. doi:10.1186/s12915-018-0577-5

20. Acin-Perez R, Enriquez JA. The function of the respiratory supercomplexes: The plasticity model. *Biochim Biophys Acta - Bioenerg*. 2014;1837(4):444-450. doi:10.1016/J.BBABIO.2013.12.009

21. Fedor JG, Hirst J. Mitochondrial Supercomplexes Do Not Enhance Catalysis by Quinone Channeling. *Cell Metab*. 2018;28(3):525-531.e4. doi:10.1016/j.cmet.2018.05.024

22. Maranzana E, Barbero G, Falasca AI, Lenaz G, Genova ML. Mitochondrial respiratory supercomplex association limits production of reactive oxygen species from complex i. *Antioxidants Redox Signal*. 2013;19(13):1469-1480. doi:10.1089/ars.2012.4845

23. Blaza JN, Serreli R, Jones AJY, Mohammed K, Hirst J. Kinetic evidence against partitioning of the ubiquinone pool and the catalytic relevance of respiratory-chain

supercomplexes. *Proc Natl Acad Sci U S A*. 2014;111(44):15735-15740. doi:10.1073/pnas.1413855111

24. Letts JA, Sazanov LA. Clarifying the supercomplex: the higher-order organization of the mitochondrial electron transport chain. *Nat Struct Mol Biol 2017 2410*. 2017;24(10):800-808. doi:10.1038/nsmb.3460

25. Calvaruso MA, Willems P, Van den brand M, et al. Mitochondrial complex III stabilizes complex I in the absence of NDUFS4 to provide partial activity. *Hum Mol Genet*. 2012;21(1):115-120. doi:10.1093/hmg/ddr446

26. Schägger H, De Coo R, Bauer MF, Hofmann S, Godino C, Brandt U. Significance of respirasomes for the assembly/stability of human respiratory chain complex I. *J Biol Chem*. 2004;279(35):36349-36353. doi:10.1074/jbc.M404033200

27. Tropeano C V., Aleo SJ, Zanna C, et al. Fine-tuning of the respiratory complexes stability and supercomplexes assembly in cells defective of complex III. *Biochim Biophys Acta - Bioenerg*. 2020;1861(2):148133. doi:10.1016/j.bbabio.2019.148133

28. Bindoli A, Rigobello MP. Electrons and Protons | Peroxidase Biochemistry and Redox Signaling. *Encycl Biol Chem Third Ed*. 2021;2:579-585. doi:10.1016/B978-0-12-809633-8.21402-7

29. Timón-Gómez A, Nývltová E, Abriata LA, Vila AJ, Hosler J, Barrientos A. Mitochondrial cytochrome c oxidase biogenesis: Recent developments. *Semin Cell Dev Biol*. 2018;76:163-178. doi:10.1016/j.semcdb.2017.08.055

30. Stiburek L, Vesela K, Hansikova H, et al. Tissue-specific cytochrome c oxidase assembly defects due to mutations in SCO2 and SURF1. *Biochem J*. 2005;392(3):625-632. doi:10.1042/BJ20050807

31. Bourens M, Boulet A, Leary SC, Barrientos A. Human COX20 cooperates with SCO1 and SCO2 to mature COX2 and promote the assembly of cytochrome c oxidase. *Hum Mol Genet*. 2014;23(11):2901-2913. doi:10.1093/hmg/ddu003

32. Vidoni S, Harbour ME, Guerrero-Castillo S, et al. MR-1S Interacts with PET100 and PET117 in Module-Based Assembly of Human Cytochrome c Oxidase. *Cell Rep*. 2017;18(7):1727-1738. doi:10.1016/j.celrep.2017.01.044

33. Zong S, Wu M, Gu J, Liu T, Guo R, Yang M. Structure of the intact 14-subunit human

cytochrome c oxidase. *Cell Res*. 2018;28(10):1026-1034. doi:10.1038/s41422-018-0071-1

34. Timón-Gómez A, Nývltová E, Abriata LA, Vila AJ, Hosler J, Barrientos A. Mitochondrial cytochrome c oxidase biogenesis: Recent developments. *Semin Cell Dev Biol*. 2018;76:163-178. doi:10.1016/j.semcdb.2017.08.055

35. Brischigliaro M, Zeviani M. Cytochrome c oxidase deficiency. *Biochim Biophys Acta - Bioenerg*. 2021;1862(1):148335. doi:10.1016/J.BBABIO.2020.148335

36. Cogliati S, Calvo E, Loureiro M, et al. Mechanism of super-assembly of respiratory complexes III and IV. *Nat 2016 5397630*. 2016;539(7630):579-582. doi:10.1038/nature20157

37. Kovářová N, Pecina P, Nůsková H, et al. Tissue- and species-specific differences in cytochrome c oxidase assembly induced by SURF1 defects. *Biochim Biophys Acta - Mol Basis Dis*. 2016;1862(4):705-715. doi:10.1016/j.bbadis.2016.01.007

38. Fukuda R, Zhang H, Kim J whan, Shimoda L, Dang C V., Semenza GLL. HIF-1 regulates cytochrome oxidase subunits to optimize efficiency of respiration in hypoxic cells. *Cell*. 2007;129(1):111-122. doi:10.1016/J.CELL.2007.01.047

39. Tello D, Balsa E, Acosta-Iborra B, et al. Induction of the Mitochondrial NDUFA4L2 Protein by HIF-1α Decreases Oxygen Consumption by Inhibiting Complex I Activity. *Cell Metab*. 2011;14(6):768-779. doi:10.1016/J.CMET.2011.10.008

40. Napiwotzki J, Shinzawa-Itoh K, Yoshikawa S, Kadenbach B. ATP and ADP bind to cytochrome c oxidase and regulate its activity. *Biol Chem*. 1997;378(9):1013-1021. doi:10.1515/bchm.1997.378.9.1013

41. Kalpage HA, Bazylianska V, Recanati MA, et al. Tissue-specific regulation of cytochrome c by post-translational modifications: respiration, the mitochondrial membrane potential, ROS, and apoptosis. *FASEB J*. 2019;33(2):1540. doi:10.1096/FJ.201801417R

42. Diaz F. Cytochrome c oxidase deficiency: Patients and animal models. *Biochim Biophys Acta - Mol Basis Dis*. 2010;1802(1):100-110. doi:10.1016/J.BBADIS.2009.07.013

43. Rak M, Bénit PP, Chrétien D, et al. Mitochondrial cytochrome c oxidase deficiency. *Clin Sci*. 2016;130(6):393-407. doi:10.1042/CS20150707

44. Dimauro S, Tanji K, Schon EA. The Many Clinical Faces of Cytochrome Oxidase Deficiency. *Adv Exp Med Biol*. 2012;748:341-357. doi:10.1007/978-1-4614-3573-0_14

45. Szabo I, Zoratti M. Mitochondrial channels: Ion fluxes and more. *Physiol Rev*. 2014;94(2):519-608. doi:10.1152/physrev.00021.2013

46. Jasielec JJ, Filipek R, Dołowy K, Lewenstam A. Precipitation of Inorganic Salts in Mitochondrial Matrix. *Membr 2020, Vol 10, Page 81*. 2020;10(5):81. doi:10.3390/MEMBRANES10050081

47. Killilea DW, Killilea AN. Mineral requirements for mitochondrial function: A connection to redox balance and cellular differentiation. *Free Radic Biol Med*. 2022;182:182-191. doi:10.1016/J.FREERADBIOMED.2022.02.022

48. Santo-Domingo J, Demaurex N. Calcium uptake mechanisms of mitochondria. *Biochim Biophys Acta - Bioenerg*. 2010;1797(6-7):907-912. doi:10.1016/J.BBABIO.2010.01.005

49. Colombini M. VDAC structure, selectivity, and dynamics. *Biochim Biophys Acta - Biomembr*. 2012;1818(6):1457-1465. doi:10.1016/J.BBAMEM.2011.12.026

50. Hill K, Model K, Ryan MT, et al. Tom40 forms the hydrophilic channel of the mitochondrial import pore for preproteins. *Nat 1998 3956701*. 1998;395(6701):516-521. doi:10.1038/26780

51. Inoue I, Nagase H, Kishi K, Higuti T. ATP-sensitive K+ channel in the mitochondrial inner membrane. *Nature*. 1991;352(6332):244-247. doi:10.1038/352244a0

52. Garlid KD. Cation transport in mitochondria - The potassium cycle. In: *Biochimica et Biophysica Acta - Bioenergetics*. Vol 1275. Elsevier B.V.; 1996:123-126. doi:10.1016/0005-2728(96)00061-8

53. Skalska J, Piwońska M, Wyroba E, et al. A novel potassium channel in skeletal muscle mitochondria. *Biochim Biophys Acta - Bioenerg*. 2008;1777(7-8):651-659. doi:10.1016/j.bbabio.2008.05.007

54. Heinen A, Camara AKS, Aldakkak M, Rhodes SS, Riess ML, Stowe DF. Mitochondrial Ca2+-induced K+ influx increases respiration and enhances ROS production while maintaining membrane potential. *Am J Physiol - Cell Physiol*. 2007;292(1):148-156. doi:10.1152/ajpcell.00215.2006

55. O'Rourke B. Mitochondrial ion channels. *Annu Rev Physiol*. 2007;69:19-49.

doi:10.1146/annurev.physiol.69.031905.163804

56. Anderson PAV, Greenberg RM. Phylogeny of ion channels: Clues to structure and function. *Comp Biochem Physiol - B Biochem Mol Biol*. 2001;129(1):17-28. doi:10.1016/S1096-4959(01)00376-1

57. Thiel G, Moroni A, Blanc G, Van Etten JL. Potassium Ion Channels: Could They Have Evolved from Viruses? *Plant Physiol*. 2013;162(3):1215. doi:10.1104/PP.113.219360

58. Ye S, Li Y, Jiang Y. Novel insights into K+ selectivity from high-resolution structures of an open K+ channel pore. *Nat Struct Mol Biol 2010 178*. 2010;17(8):1019-1023. doi:10.1038/nsmb.1865

59. Szewczyk A, Jędraszko J, Kampa RP, et al. Mitochondrial potassium channels - an overview. *Postepy Biochem*. 2018;64(3):196-212. doi:10.18388/pb.2018_132

60. Checchetto V, Prosdocimi E, Leanza L. Mitochondrial Kv1.3: a New Target in Cancer Biology? *Cell Physiol Biochem*. 2019;53(S1):52-62. doi:10.33594/000000195

61. Checchetto V, Azzolini M, Peruzzo R, Capitanio P, Leanza L. Mitochondrial potassium channels in cell death. *Biochem Biophys Res Commun*. 2018;500(1):51-58. doi:10.1016/j.bbrc.2017.06.095

62. Bonnet S, Archer SL, Allalunis-Turner J, et al. A Mitochondria-K+ Channel Axis Is Suppressed in Cancer and Its Normalization Promotes Apoptosis and Inhibits Cancer Growth. *Cancer Cell*. 2007;11(1):37-51. doi:10.1016/j.ccr.2006.10.020

63. Testai L, Barrese V, Soldovieri MV, et al. Expression and function of Kv7.4 channels in rat cardiac mitochondria: Possible targets for cardioprotection. *Cardiovasc Res*. 2016;110(1):40-50. doi:10.1093/cvr/cvv281

64. Paggio A, Checchetto V, Campo A, et al. Identification of an ATP-sensitive potassium channel in mitochondria. *Nat 2019 5727771*. 2019;572(7771):609-613. doi:10.1038/s41586-019-1498-3

65. Juhaszova M, Kobrinsky E, Zorov DB, et al. ATP Synthase K+- and H+-fluxes Drive ATP Synthesis and Enable Mitochondrial K+-"Uniporter" Function: II. Ion and ATP Synthase Flux Regulation. *Function*. 2022;3(2). doi:10.1093/function/zqac001

66. Smith CO, Wang YT, Nadtochiy SM, et al. Cardiac metabolic effects of KNa1.2 channel deletion and evidence for its mitochondrial localization. *FASEB J*. 2018;32(11):6135-

6149. doi:10.1096/fj.201800139R

67. Bednarczyk P, Koziel A, Jarmuszkiewicz W, Szewczyk A. Large-conductance Ca^{2+}-activated potassium channel in mitochondria of endothelial EA.hy926 cells. *Am J Physiol Heart Circ Physiol*. 2013;304(11). doi:10.1152/AJPHEART.00976.2012

68. Piwonska M, Wilczek E, Szewczyk A, Wilczynski GM. Differential distribution of Ca2+-activated potassium channel β4 subunit in rat brain: Immunolocalization in neuronal mitochondria. *Neuroscience*. 2008;153(2):446-460. doi:10.1016/j.neuroscience.2008.01.050

69. Xu W, Liu Y, Wang S, et al. Cytoprotective role of Ca2+-activated K+ channels in the cardiac inner mitochondrial membrane. *Science (80-).* 2002;298(5595):1029-1033. doi:10.1126/science.1074360

70. Skalska J, Piwońska M, Wyroba E, et al. A novel potassium channel in skeletal muscle mitochondria. *Biochim Biophys Acta*. 2008;1777(7-8):651-659. doi:10.1016/J.BBABIO.2008.05.007

71. Kicinska A, Augustynek B, Kulawiak B, Jarmuszkiewicz W, Szewczyk A, Bednarczyk P. A large-conductance calcium-regulated K + channel in human dermal fibroblast mitochondria. *Biochem J*. 2016;473(23):4457-4471. doi:10.1042/BCJ20160732

72. Koszela-Piotrowska I, Matkovic K, Szewczyk A, Jarmuszkiewicz W. A large-conductance calcium-activated potassium channel in potato (Solanum tuberosum) tuber mitochondria. *Biochem J*. 2009;424(2):307-316. doi:10.1042/BJ20090991

73. Laskowski M, Kicinska A, Szewczyk A, Jarmuszkiewicz W. Mitochondrial large-conductance potassium channel from Dictyostelium discoideum. *Int J Biochem Cell Biol*. 2015;60:167-175. doi:10.1016/J.BIOCEL.2015.01.006

74. Tress ML, Abascal F, Valencia A. Alternative Splicing May Not Be the Key to Proteome Complexity. *Trends Biochem Sci*. 2017;42(2):98-110. doi:10.1016/j.tibs.2016.08.008

75. Miller JP, Moldenhauer HJ, Keros S, Meredith AL. An emerging spectrum of variants and clinical features in KCNMA1-linked channelopathy. *https://doi.org/101080/19336950202211938852*. 2021;15(1):447-464. doi:10.1080/19336950.2021.1938852

76. Singh H, Lu R, Bopassa JC, Meredith AL, Stefani E, Toro L. MitoBKCa is encoded by

the Kcnma1 gene, and a splicing sequence defines its mitochondrial location. *Proc Natl Acad Sci U S A*. 2013;110(26):10836-10841. doi:10.1073/pnas.1302028110

77. Gałecka S, Kulawiak B, Bednarczyk P, Singh H, Szewczyk A. Single channel properties of mitochondrial large conductance potassium channel formed by BK-VEDEC splice variant. *Sci Reports 2021 111*. 2021;11(1):1-12. doi:10.1038/s41598-021-90465-3

78. Ma D, Nakata T, Zhang G, Hoshi T, Li M, Shikano S. Differential trafficking of carboxyl isoforms of Ca2+-gated (Slo1) potassium channels. *FEBS Lett*. 2007;581(5):1000-1008. doi:10.1016/J.FEBSLET.2007.01.077

79. Walewska A, Kulawiak B, Szewczyk A, Koprowski P. Mechanosensitivity of mitochondrial large-conductance calcium-activated potassium channels. *Biochim Biophys Acta - Bioenerg*. 2018;1859(9):797-805. doi:10.1016/j.bbabio.2018.05.006

80. Chen L, Bi D, Tian L, et al. Palmitoylation of the β4-subunit regulates surface expression of large conductance calcium-activated potassium channel splice variants. *J Biol Chem*. 2013;288(18):13136-13144. doi:10.1074/jbc.M113.461830

81. Engel AJ, Kithil M, Langhans M, et al. Codon Bias Can Determine Sorting of a Potassium Channel Protein. *Cells*. 2021;10(5):1128. doi:10.3390/cells10051128

82. Zhang J, Li M, Zhang Z, et al. The mitochondrial BKCa channel cardiac interactome reveals BKCa association with the mitochondrial import receptor subunit Tom22, and the adenine nucleotide translocator. *Mitochondrion*. 2017;33:84-101. doi:10.1016/j.mito.2016.08.017

83. Wang L, Sigworth FJ. Structure of the BK potassium channel in a lipid membrane from electron cryomicroscopy. *Nat 2009 4617261*. 2009;461(7261):292-295. doi:10.1038/nature08291

84. Tao X, Mackinnon R. Molecular structures of the human slo1 k+ channel in complex with b4. *Elife*. 2019;8. doi:10.7554/ELIFE.51409

85. Peng Yuan, Leonetti MD, Pico AR, Hsiung Y, MacKinnon R. Structure of the Human BK Channel Ca2+-Activation Apparatus at 3.0 Å Resolution. *Science (80-)*. 2010;329(5988):182-186. doi:10.1126/science.1190414

86. González-Cota AL, Santana-Calvo C, Servín-Vences R, Orta G, Balderas E. Regulatory mechanisms of mitochondrial BKCa channels. *Channels*. 2021;15(1):424-437.

doi:10.1080/19336950.2021.1919463

87. Lee US, Cui J. BK channel activation: Structural and functional insights. *Trends Neurosci*. 2010;33(9):415-423. doi:10.1016/j.tins.2010.06.004

88. Yang H, Zhang G, Cui J. BK channels: Multiple sensors, one activation gate. *Front Physiol*. 2015;6(FEB):29. doi:10.3389/fphys.2015.00029

89. Latorre R, Castillo K, Carrasquel-Ursulaez W, et al. Molecular determinants of BK channel functional diversity and functioning. *Physiol Rev*. 2017;97(1):39-87. doi:10.1152/physrev.00001.2016

90. Lee US, Cui J. BK channel activation: structural and functional insights. *Trends Neurosci*. 2010;33(9):415-423. doi:10.1016/J.TINS.2010.06.004

91. Hoshi T, Pantazis A, Olcese R. Transduction of voltage and Ca2+ signals by Slo1 BK channels. *Physiology*. 2013;28(3):172-189. doi:10.1152/physiol.00055.2012

92. Gonzalez-Perez V, Lingle CJ. Regulation of BK Channels by Beta and Gamma Subunits. *Annu Rev Physiol*. 2019;81:113. doi:10.1146/ANNUREV-PHYSIOL-022516-034038

93. Hu S, Han R, Chen L, et al. Upregulated LRRC55 promotes BK channel activation and aggravates cell injury in podocytes. *J Exp Med*. 2021;218(2). doi:10.1084/JEM.20192373/211626

94. Yan J, Aldrich RW. BK potassium channel modulation by leucine-rich repeat-containing proteins. *Proc Natl Acad Sci U S A*. 2012;109(20):7917-7922. doi:10.1073/pnas.1205435109

95. Szewczyk A, Kajma A, Malinska D, et al. Pharmacology of mitochondrial potassium channels: dark side of the field. *FEBS Lett*. 2010;584(10):2063-2069. doi:10.1016/J.FEBSLET.2010.02.048

96. Augustynek B, Kunz WS, Szewczyk A. Guide to the Pharmacology of Mitochondrial Potassium Channels. *Handb Exp Pharmacol*. 2016;240:103-127. doi:10.1007/164_2016_79

97. Aon MA, Cortassa S, Wei AC, Grunnet M, O'Rourke B. Energetic performance is improved by specific activation of K+ fluxes through K(Ca) channels in heart mitochondria. *Biochim Biophys Acta*. 2010;1797(1):71-80. doi:10.1016/J.BBABIO.2009.08.002

98. Hirusaki K, Yokoyama K, Cho K, Ohta Y. Temporal depolarization of mitochondria during M phase. *Sci Rep*. 2017;7(1). doi:10.1038/S41598-017-15907-3

99. Kulawiak B, Kudin AP, Szewczyk A, Kunz WS. BK channel openers inhibit ROS production of isolated rat brain mitochondria. *Exp Neurol*. 2008;212(2):543-547. doi:10.1016/j.expneurol.2008.05.004

100. Goswami S, Ponnalagu D, Hussain A, et al. Expression and activation of BKCa channels in mice protects against ischemia-reperfusion injury of isolated hearts by modulating mitochondrial function. *Front Cardiovasc Med*. 2019;5:194. doi:10.3389/fcvm.2018.00194

101. Balderas E, Torres NS, Rosa-Garrido M, et al. MitoBK Ca channel is functionally associated with its regulatory β1 subunit in cardiac mitochondria. *J Physiol*. 2019;597(15):3817-3832. doi:10.1113/JP277769

102. Vygodina T, Kirichenko A, Konstantinov AA. Direct Regulation of Cytochrome c Oxidase by Calcium Ions. *PLoS One*. 2013;8(9):e74436. doi:10.1371/JOURNAL.PONE.0074436

103. Brookes PS, Yoon Y, Robotham JL, Anders MW, Sheu SS. Calcium, ATP, and ROS: a mitochondrial love-hate triangle. *Am J Physiol Cell Physiol*. 2004;287(4). doi:10.1152/AJPCELL.00139.2004

104. Bednarczyk P, Wieckowski MR, Broszkiewicz M, Skowronek K, Siemen D, Szewczyk A. Putative Structural and Functional Coupling of the Mitochondrial BKCa Channel to the Respiratory Chain. *PLoS One*. 2013;8(6). doi:10.1371/journal.pone.0068125

105. Ohya S, Kuwata Y, Sakamoto K, Muraki K, Imaizumi Y. Cardioprotective effects of estradiol include the activation of large-conductance Ca2+-activated K+ channels in cardiac mitochondria. *Am J Physiol - Hear Circ Physiol*. 2005;289(4 58-4):1635-1642. doi:10.1152/ajpheart.00016.2005

106. Singh H, Li M, Hall L, et al. MaxiK channel interactome reveals its interaction with GABA transporter 3 and heat shock protein 60 in the mammalian brain. *Neuroscience*. 2016;317:76-107. doi:10.1016/j.neuroscience.2015.12.058

107. Da Cunha FM, Torelli NQ, Kowaltowski AJ. Mitochondrial Retrograde Signaling: Triggers, Pathways, and Outcomes. *Oxid Med Cell Longev*. 2015;2015. doi:10.1155/2015/482582

108. Pfannschmidt T, Terry MJ, Van Aken O, Quiros PM. Retrograde signals from endosymbiotic organelles: a common control principle in eukaryotic cells. *Philos Trans R Soc B*. 2020;375(1801). doi:10.1098/RSTB.2019.0396

109. Pellegrino MW, Nargund AM, Haynes CM. Signaling the mitochondrial unfolded protein response. *Biochim Biophys Acta - Mol Cell Res*. 2013;1833(2):410-416. doi:10.1016/j.bbamcr.2012.02.019

110. Vögtle FN. Open questions on the mitochondrial unfolded protein response. *FEBS J*. 2021;288(9):2856-2869. doi:10.1111/FEBS.15569

111. Anderson NS, Haynes CM. Folding the Mitochondrial UPR into the Integrated Stress Response. *Trends Cell Biol*. 2020;30(6):428-439. doi:10.1016/j.tcb.2020.03.001

112. Quirós PM, Mottis A, Auwerx J. Mitonuclear communication in homeostasis and stress. *Nat Rev Mol Cell Biol*. 2016;17(4):213-226. doi:10.1038/nrm.2016.23

113. Taniuchi S, Miyake M, Tsugawa K, Oyadomari M, Oyadomari S. Integrated stress response of vertebrates is regulated by four eIF2α kinases. *Sci Rep*. 2016;6. doi:10.1038/srep32886

114. Guo X, Aviles G, Liu Y, et al. Mitochondrial stress is relayed to the cytosol by an OMA1–DELE1–HRI pathway. *Nature*. 2020;579(7799):427-432. doi:10.1038/s41586-020-2078-2

115. Haynes CM, Ron D. The mitochondrial UPR - Protecting organelle protein homeostasis. *J Cell Sci*. 2010;123(22):3849-3855. doi:10.1242/jcs.075119

116. Michel S, Canonne M, Arnould T, Renard P. Inhibition of mitochondrial genome expression triggers the activation of CHOP-10 by a cell signaling dependent on the integrated stress response but not the mitochondrial unfolded protein response. *Mitochondrion*. 2015;21:58-68. doi:10.1016/j.mito.2015.01.005

117. Qureshi MA, Haynes CM, Pellegrino MW. The mitochondrial unfolded protein response: Signaling from the powerhouse. *J Biol Chem*. 2017;292(33):13500-13506. doi:10.1074/jbc.R117.791061

118. Wang G, Fan Y, Cao P, Tan K. Insight into the mitochondrial unfolded protein response and cancer: opportunities and challenges. *Cell Biosci*. 2022;12(1):1-23. doi:10.1186/s13578-022-00747-0

119. Fiorese CJ, Schulz AM, Lin YF, Rosin N, Pellegrino MW, Haynes CM. The Transcription Factor ATF5 Mediates a Mammalian Mitochondrial UPR. *Curr Biol*. 2016;26(15):2037-2043. doi:10.1016/j.cub.2016.06.002

120. Quirós PM, Langer T, López-Otín C. New roles for mitochondrial proteases in health, ageing and disease. *Nat Rev Mol Cell Biol*. 2015;16(6):345-359. doi:10.1038/nrm3984

121. Pellegrino MW, Nargund AM, Haynes CM. Signaling the mitochondrial unfolded protein response. *Biochim Biophys Acta - Mol Cell Res*. 2013;1833(2):410-416. doi:10.1016/j.bbamcr.2012.02.019

122. Wodrich APK, Scott AW, Shukla AK, Harris BT, Giniger E. The Unfolded Protein Responses in Health, Aging, and Neurodegeneration: Recent Advances and Future Considerations. *Front Mol Neurosci*. 2022;15:37. doi:10.3389/fnmol.2022.831116

123. Chen Y, Dorn GW. PINK1-phosphorylated mitofusin 2 is a parkin receptor for culling damaged mitochondria. *Science (80-).* 2013;340(6131):471-475. doi:10.1126/science.1231031

124. Walewska A, Szewczyk A, Krajewska M, Koprowski P. Targeting Mitochondrial Large-Conductance Calcium-Activated Potassium Channel by Hydrogen Sulfide via Heme-Binding Site. *J Pharmacol Exp Ther*. 2022;381(2):137-150. doi:10.1124/JPET.121.001017

125. Frankenreiter S, Bednarczyk P, Kniess A, et al. cGMP-Elevating Compounds and Ischemic Conditioning Provide Cardioprotection Against Ischemia and Reperfusion Injury via Cardiomyocyte-Specific BK Channels. *Circulation*. 2017;136(24):2337-2355. doi:10.1161/CIRCULATIONAHA.117.028723

126. Kampa RP, Kicinska A, Jarmuszkiewicz W, et al. Naringenin as an opener of mitochondrial potassium channels in dermal fibroblasts. *Exp Dermatol*. 2019;28(5):543-550. doi:10.1111/exd.13903

127. Tang XD, Xu R, Reynolds MF, Garcia ML, Heinemann SH, Hoshi T. Haem can bind to and inhibit mammalian calcium-dependent Slo1 BK channels. *Nature*. 2003;425(6957):531-535. doi:10.1038/nature02003

128. Horrigan FT, Heinemann SH, Hoshi T. Heme regulates allosteric activation of the Slo1 BK channel. *J Gen Physiol*. 2005;126(1):7-21. doi:10.1085/jgp.200509262

129. Augustynek B, Kudin AP, Bednarczyk P, Szewczyk A, Kunz WS. Hemin inhibits the large conductance potassium channel in brain mitochondria: a putative novel mechanism of neurodegeneration. *Exp Neurol*. 2014;257:70-75. doi:10.1016/J.EXPNEUROL.2014.04.022

130. Ryter SW, Alam J, Choi AMK. Heme oxygenase-1/carbon monoxide: From basic science to therapeutic applications. *Physiol Rev*. 2006;86(2):583-650. doi:10.1152/physrev.00011.2005

131. Piantadosi CA, Carraway MS, Babiker A, Suliman HB. Heme oxygenase-1 regulates cardiac mitochondrial biogenesis via Nrf2-mediated transcriptional control of nuclear respiratory factor-1. *Circ Res*. 2008;103(11):1232-1240. doi:10.1161/01.RES.0000338597.71702.AD

132. Motterlini R, Otterbein LE. The therapeutic potential of carbon monoxide. *Nat Rev Drug Discov*. 2010;9(9):728-743. doi:10.1038/NRD3228

133. Ryter SW, Otterbein LE. Carbon monoxide in biology and medicine. *BioEssays*. 2004;26(3):270-280. doi:10.1002/bies.20005

134. García-Gallego S, Bernardes GJL. Carbon-monoxide-releasing molecules for the delivery of therapeutic co in vivo. *Angew Chemie - Int Ed*. 2014;53(37):9712-9721. doi:10.1002/anie.201311225

135. Zobi F. CO and CO-releasing molecules in medicinal chemistry. *Future Med Chem*. 2013;5(2):175-188. doi:10.4155/fmc.12.196

136. Kautz AC, Kunz PC, Janiak C. CO-releasing molecule (CORM) conjugate systems. *Dalt Trans*. 2016;45(45):18045-18063. doi:10.1039/C6DT03515A

137. Kaczara P, Motterlini R, Rosen GM, et al. Biochimica et Biophysica Acta Carbon monoxide released by CORM-401 uncouples mitochondrial respiration and inhibits glycolysis in endothelial cells : A role for mitoBK Ca channels. *BBA - Bioenerg*. 2015;1847(10):1297-1309. doi:10.1016/j.bbabio.2015.07.004

138. Decaluwé K, Pauwels B, Verpoest S, Van De Voorde J. Divergent mechanisms involved in CO and CORM-2 induced vasorelaxation. *Eur J Pharmacol*. 2012;674(2-3):370-377. doi:10.1016/J.EJPHAR.2011.11.004

139. Gessner G, Sahoo N, Swain SM, et al. CO-independent modification of K+ channels by

tricarbonyldichlororuthenium(II) dimer (CORM-2). *Eur J Pharmacol*. 2017;815:33. doi:10.1016/J.EJPHAR.2017.10.006

140. Dong DL, Chen C, Huang W, et al. Tricarbonyldichlororuthenium (II) dimer (CORM2) activates non-selective cation current in human endothelial cells independently of carbon monoxide releasing. *Eur J Pharmacol*. 2008;590(1-3):99-104. doi:10.1016/J.EJPHAR.2008.05.042

141. Almeida AS, Figueiredo-Pereira C, Vieira HLA. Carbon monoxide and mitochondria-modulation of cell metabolism, redox response and cell death. *Front Physiol*. 2015;6(FEB):1-6. doi:10.3389/fphys.2015.00033

142. Calvo-Rodríguez M, García-Durillo M, Villalobos C, Núñez L. In vitro aging promotes endoplasmic reticulum (ER)-mitochondria Ca2 + cross talk and loss of store-operated Ca2 + entry (SOCE) in rat hippocampal neurons. *Biochim Biophys Acta - Mol Cell Res*. 2016;1863(11):2637-2649. doi:10.1016/j.bbamcr.2016.08.001

143. Bereiter-Hahn J. Mitochondrial dynamics in aging and disease. In: *Progress in Molecular Biology and Translational Science*. Vol 127. Elsevier B.V.; 2014:93-131. doi:10.1016/B978-0-12-394625-6.00004-0

144. Trombetta-Lima M, Krabbendam IE, Dolga AM. Calcium-activated potassium channels: implications for aging and age-related neurodegeneration. *Int J Biochem Cell Biol*. 2020;123:105748. doi:10.1016/j.biocel.2020.105748

145. Soltysinska E, Bentzen BH, Barthmes M, et al. KCNMA1 Encoded Cardiac BK Channels Afford Protection against Ischemia-Reperfusion Injury. *PLoS One*. 2014;9(7):e103402. doi:10.1371/JOURNAL.PONE.0103402

146. Kravenska Y, Nieznanska H, Nieznanski K, Lukyanetz E, Szewczyk A, Koprowski P. The monomers, oligomers, and fibrils of amyloid-β inhibit the activity of mitoBK Ca channels by a membrane-mediated mechanism. *Biochim Biophys acta Biomembr*. 2020;1862(9). doi:10.1016/J.BBAMEM.2020.183337

147. Cheng Y, Gu XQ, Bednarczyk P, Wiedemann FR, Haddad GG, Siemen D. Hypoxia increases activity of the BK-channel in the inner mitochondrial membrane and reduces activity of the permeability transition pore. *Cell Physiol Biochem*. 2008;22(1-4):127-136. doi:10.1159/000149790

148. Typlt M, Mirkowski M, Azzopardi E, Ruettiger L, Ruth P, Schmid S. Mice with

Deficient BK Channel Function Show Impaired Prepulse Inhibition and Spatial Learning, but Normal Working and Spatial Reference Memory. Ceña V, ed. *PLoS One*. 2013;8(11):e81270. doi:10.1371/journal.pone.0081270

149. Wang J, Yu S, Zhang Q, Chen Y, Bao X, Wu X. KCNMA1 mutation in children with paroxysmal dyskinesia and epilepsy: Case report and literature review. *Transl Sci Rare Dis*. 2017;2(3-4):165-173. doi:10.3233/trd-170018

150. Gururaja Rao S, Bednarczyk P, Towheed A, et al. BKCa (Slo) Channel Regulates Mitochondrial Function and Lifespan in Drosophila melanogaster. *Cells*. 2019;8(9):945. doi:10.3390/cells8090945

151. Frankenreiter S, Bednarczyk P, Kniess A, et al. cGMP-Elevating Compounds and Ischemic Conditioning Provide Cardioprotection Against Ischemia and Reperfusion Injury via Cardiomyocyte-Specific BK Channels. *Circulation*. 2017;136(24):2337-2355. doi:10.1161/CIRCULATIONAHA.117.028723

152. Hallmann K, Kudin AP, Zsurka G, et al. Loss of the smallest subunit of cytochrome c oxidase, COX8A, causes Leigh-like syndrome and epilepsy. *Brain*. 2016;139(2):338-345. doi:10.1093/brain/awv357

153. Martin JL, Brown CE, Matthews-Davis N, Reardon JE. Effects of antiviral nucleoside analogs on human DNA polymerases and mitochondrial DNA synthesis. *Antimicrob Agents Chemother*. 1994;38(12):2743-2749. doi:10.1128/AAC.38.12.2743

154. Ran FA, Hsu PD, Wright J, Agarwala V, Scott DA, Zhang F. Genome engineering using the CRISPR-Cas9 system. *Nat Protoc*. 2013;8(11):2281-2308. doi:10.1038/nprot.2013.143

155. Augustynek B, Kudin AP, Bednarczyk P, Szewczyk A, Kunz WS. Hemin inhibits the large conductance potassium channel in brain mitochondria: A putative novel mechanism of neurodegeneration. *Exp Neurol*. 2014;257:70-75. doi:10.1016/j.expneurol.2014.04.022

156. Gessner G, Sahoo N, Swain SM, et al. CO-independent modification of K + channels by tricarbonyldichlororuthenium(II) dimer (CORM-2). *Eur J Pharmacol*. 2017;815(September):33-41. doi:10.1016/j.ejphar.2017.10.006

157. Jaggar JH, Li A, Parfenova H, et al. Heme is a carbon monoxide receptor for large-conductance Ca2+-activated K+ channels. *Circ Res*. 2005;97(8):805-812.

doi:10.1161/01.RES.0000186180.47148.7B

158. Wiedemann FR, Vielhaber S, Schröder R, Elger CE, Kunz WS. Evaluation of methods for the determination of mitochondrial respiratory chain enzyme activities in human skeletal muscle samples. *Anal Biochem*. 2000;279(1):55-60. doi:10.1006/abio.1999.4434

159. Bednarczyk P, Kicinska A, Laskowski M, et al. Evidence for a mitochondrial ATP-regulated potassium channel in human dermal fibroblasts. *Biochim Biophys acta Bioenerg*. 2018;1859(5):309-318. doi:10.1016/J.BBABIO.2018.02.005

160. Kim J, Han J, Jang Y, et al. High-capacity glycolytic and mitochondrial oxidative metabolisms mediate the growth ability of glioblastoma. *Int J Oncol*. 2015;47(3):1009-1016. doi:10.3892/ijo.2015.3101

161. Martin JL, Brown CE, Matthews-Davis N, Reardon JE. Effects of antiviral nucleoside analogs on human DNA polymerases and mitochondrial DNA synthesis. *Antimicrob Agents Chemother*. 1994;38(12):2743-2749. doi:10.1128/AAC.38.12.2743

162. Dillies MA, Rau A, Aubert J, et al. A comprehensive evaluation of normalization methods for Illumina high-throughput RNA sequencing data analysis. *Brief Bioinform*. 2013;14(6):671-683. doi:10.1093/bib/bbs046

163. Lin Y, Golovnina K, Chen ZX, et al. Comparison of normalization and differential expression analyses using RNA-Seq data from 726 individual Drosophila melanogaster. *BMC Genomics*. 2016;17(1):28. doi:10.1186/s12864-015-2353-z

164. Jovaisaite V, Mouchiroud L, Auwerx J. The mitochondrial unfolded protein response, a conserved stress response pathway with implications in health and disease. *J Exp Biol*. 2014;217(1):137-143. doi:10.1242/jeb.090738

165. Tonelli C, Chio IIC, Tuveson DA. Transcriptional Regulation by Nrf2. *Antioxidants Redox Signal*. 2018;29(17):1727-1745. doi:10.1089/ars.2017.7342

166. Ward JM, Stoyas CA, Switonski PM, et al. Metabolic and Organelle Morphology Defects in Mice and Human Patients Define Spinocerebellar Ataxia Type 7 as a Mitochondrial Disease. *Cell Rep*. 2019;26(5):1189-1202.e6. doi:10.1016/j.celrep.2019.01.028

167. Stoyas CA, Bushart DD, Switonski PM, et al. Nicotinamide Pathway-Dependent Sirt1

Activation Restores Calcium Homeostasis to Achieve Neuroprotection in Spinocerebellar Ataxia Type 7. *Neuron*. 2020;105(4):630-644.e9. doi:10.1016/j.neuron.2019.11.019

168. Goldberg A, Wildman DE, Schmidt TR, et al. Adaptive evolution of cytochrome c oxidase subunit VIII in anthropoid primates. *Proc Natl Acad Sci U S A*. 2003;100(10):5873-5878. doi:10.1073/pnas.0931463100

169. Shimizu T, Huang D, Yan F, et al. Gaseous O2, NO, and CO in signal transduction: structure and function relationships of heme-based gas sensors and heme-redox sensors. *Chem Rev*. 2015;115(13):6491-6533. doi:10.1021/acs.chemrev.5b00018

170. Cha MY, Kim DK y., Mook-Jung I. The role of mitochondrial DNA mutation on neurodegenerative diseases. *Exp Mol Med 2015 473*. 2015;47(3):e150-e150. doi:10.1038/emm.2014.122

171. Chow J, Rahman J, Achermann JC, Dattani MT, Rahman S. Mitochondrial disease and endocrine dysfunction. *Nat Rev Endocrinol*. 2017;13(2):92-104. doi:10.1038/NRENDO.2016.151

172. Wallace DC. Mitochondria and cancer. *Nat Rev Cancer*. 2012;12(10):685-698. doi:10.1038/nrc3365

173. Kirkwood TBL, Korolchuk VI, Szczepanowska K, Trifunovic A. Origins of mtDNA mutations in ageing. *Essays Biochem*. 2017;61(3):325-337. doi:10.1042/EBC20160090

174. Spadafora D, Kozhukhar N, Chouljenko VN, Kousoulas KG, Alexeyev MF. Methods for Efficient Elimination of Mitochondrial DNA from Cultured Cells. *PLoS One*. 2016;11(5):e0154684. doi:10.1371/JOURNAL.PONE.0154684

175. Kukat A, Kukat C, Brocher J, et al. Generation of ρ 0 cells utilizing a mitochondrially targeted restriction endonuclease and comparative analyses. *Nucleic Acids Res*. 2008;36(7):e44-e44. doi:10.1093/NAR/GKN124

176. Rahman S, Copeland WC. POLG-related disorders and their neurological manifestations. *Nat Rev Neurol*. 2019;15(1):40. doi:10.1038/S41582-018-0101-0

177. Lewis W, Copeland WC, Day BJ. Mitochondrial DNA depletion, oxidative stress, and mutation: Mechanisms of dysfunction from nucleoside reverse transcriptase inhibitors. *Lab Investig*. 2001;81(6):777-790. doi:10.1038/labinvest.3780288

178. Chen CH, Cheng YC. The role of cytoplasmic deoxycytidine kinase in the mitochondrial effects of the antihuman immunodeficiency virus compound, 2',3'-dideoxycytidine. *J Biol Chem*. 1992;267(5):2856-2859. doi:10.1016/s0021-9258(19)50661-5

179. Khan NA, Nikkanen J, Yatsuga S, et al. mTORC1 Regulates Mitochondrial Integrated Stress Response and Mitochondrial Myopathy Progression. *Cell Metab*. 2017;26(2):419-428.e5. doi:10.1016/j.cmet.2017.07.007

180. Forsström S, Jackson CB, Carroll CJ, et al. Fibroblast Growth Factor 21 Drives Dynamics of Local and Systemic Stress Responses in Mitochondrial Myopathy with mtDNA Deletions. *Cell Metab*. 2019;30(6):1040-1054.e7. doi:10.1016/j.cmet.2019.08.019

181. Lehtonen JM, Forsström S, Bottani E, et al. FGF21 is a biomarker for mitochondrial translation and mtDNA maintenance disorders. *Neurology*. 2016;87(22):2290. doi:10.1212/WNL.0000000000003374

182. Mick E, Titov D V., Skinner OS, Sharma R, Jourdain AA, Mootha VK. Distinct mitochondrial defects trigger the integrated stress response depending on the metabolic state of the cell. *Elife*. 2020;9. doi:10.7554/ELIFE.49178

183. Wang P, Deng J, Dong J, et al. *TDP-43 Induces Mitochondrial Damage and Activates the Mitochondrial Unfolded Protein Response*. Vol 15.; 2019. doi:10.1371/journal.pgen.1007947

184. Srivastava S. Emerging therapeutic roles for NAD+ metabolism in mitochondrial and age-related disorders. *Clin Transl Med*. 2016;5(1). doi:10.1186/S40169-016-0104-7

185. Sun X, Qian LL, Li Y, et al. Regulation of KCNMA1 Transcription by Nrf2 in Coronary Arterial Smooth Muscle Cells. *J Mol Cell Cardiol*. 2020;140:68. doi:10.1016/J.YJMCC.2020.03.001

186. Vivian CJ, Brinker AE, Graw S, et al. Mitochondrial Genomic Backgrounds Affect Nuclear DNA Methylation and Gene Expression. *Cancer Res*. 2017;77(22):6202-6214. doi:10.1158/0008-5472.CAN-17-1473

187. Sutendra G, Kinnaird A, Dromparis P, et al. A nuclear pyruvate dehydrogenase complex is important for the generation of acetyl-CoA and histone acetylation. *Cell*. 2014;158(1):84-97. doi:10.1016/J.CELL.2014.04.046

188. Basile MS, Fagone P, Mangano K, et al. KCNMA1 Expression Is Downregulated in Colorectal Cancer via Epigenetic Mechanisms. *Cancers 2019, Vol 11, Page 245*. 2019;11(2):245. doi:10.3390/CANCERS11020245

189. Cheng YY, Wright CM, Kirschner MB, et al. KCa1.1, a calcium-activated potassium channel subunit alpha 1, is targeted by miR-17-5p and modulates cell migration in malignant pleural mesothelioma. *Mol Cancer*. 2016;15(1). doi:10.1186/S12943-016-0529-Z

190. Samuel P, Pink RC, Caley DP, Currie JMS, Brooks SA, Carter DRF. Over-expression of miR-31 or loss of KCNMA1 leads to increased cisplatin resistance in ovarian cancer cells. *Tumour Biol*. 2016;37(2):2565-2573. doi:10.1007/S13277-015-4081-Z

191. Mazar J, de Young K, Khaitan D, et al. The regulation of miRNA-211 expression and its role in melanoma cell invasiveness. *PLoS One*. 2010;5(11). doi:10.1371/JOURNAL.PONE.0013779

192. Muir R, Diot A, Poulton J. Mitochondrial content is central to nuclear gene expression: Profound implications for human health. *BioEssays*. 2016;38(2):150-156. doi:10.1002/BIES.201500105

193. Veatch JR, McMurray MA, Nelson ZW, Gottschling DE. Mitochondrial dysfunction leads to nuclear genome instability via an iron-sulfur cluster defect. *Cell*. 2009;137(7):1247-1258. doi:10.1016/J.CELL.2009.04.014

194. Pacheco Otalora LF, Hernandez EF, Arshadmansab MF, et al. Down-regulation of BK channel expression in the pilocarpine model of temporal lobe epilepsy. *Brain Res*. 2008;1200:116-131. doi:10.1016/J.BRAINRES.2008.01.017

195. Lu T, Zhang DM, Wang XL, et al. Regulation of coronary arterial bk channels by caveolae-mediated angiotensin II signaling in diabetes mellitus. *Circ Res*. 2010;106(6):1164-1173. doi:10.1161/CIRCRESAHA.109.209767

196. Zhang DM, He T, Katusic ZS, Lee HC, Lu T. Muscle-specific f-box only proteins facilitate bk channel β(1) subunit downregulation in vascular smooth muscle cells of diabetes mellitus. *Circ Res*. 2010;107(12):1454-1459. doi:10.1161/CIRCRESAHA.110.228361

197. Ning F ling, Tao J, Li D dan, et al. Activating BK channels ameliorates vascular smooth muscle calcification through Akt signaling. *Acta Pharmacol Sin*. 2022;43(3):624-633.

doi:10.1038/s41401-021-00704-6

198. Chen SR, Cai YQ, Pan HL. Plasticity and emerging role of BKCa channels in nociceptive control in neuropathic pain. *J Neurochem*. 2009;110(1):352-362. doi:10.1111/J.1471-4159.2009.06138.X

199. Cheng KI, Yang KT, Kung CL, et al. BKCa Channel Inhibition by Peripheral Nerve Injury Is Restored by the Xanthine Derivative KMUP-1 in Dorsal Root Ganglia. *Cells 2021, Vol 10, Page 949*. 2021;10(4):949. doi:10.3390/CELLS10040949

200. Cao XH, Chen SR, Li L, Pan HL. Nerve injury increases brain-derived neurotrophic factor levels to suppress BK channel activity in primary sensory neurons. *J Neurochem*. 2012;121(6):944-953. doi:10.1111/J.1471-4159.2012.07736.X

201. Yang D, Kim J. Mitochondrial Retrograde Signalling and Metabolic Alterations in the Tumour Microenvironment. *Cells*. 2019;8(3):275. doi:10.3390/CELLS8030275

202. Bloch M, Ousingsawat J, Simon R, et al. KCNMA1 gene amplification promotes tumor cell proliferation in human prostate cancer. *Oncogene*. 2007;26(17):2525-2534. doi:10.1038/SJ.ONC.1210036

203. Oeggerli M, Tian Y, Ruiz C, et al. Role of KCNMA1 in Breast Cancer. *PLoS One*. 2012;7(8):e41664. doi:10.1371/JOURNAL.PONE.0041664

204. Ramírez A, Vera E, Gamboa-Domínguez A, Lambert P, Gariglio P, Camacho J. Calcium-activated potassium channels as potential early markers of human cervical cancer. *Oncol Lett*. 2018;15(5):7249-7254. doi:10.3892/OL.2018.8187/HTML

205. Lobo-Jarne T, Pérez-Pérez R, Fontanesi F, et al. Multiple pathways coordinate assembly of human mitochondrial complex IV and stabilization of respiratory supercomplexes. *EMBO J*. 2020;39(14). doi:10.15252/embj.2019103912

206. Kovářová N, Čížková Vrbacká A, Pecina P, et al. Adaptation of respiratory chain biogenesis to cytochrome c oxidase deficiency caused by SURF1 gene mutations. *Biochim Biophys Acta - Mol Basis Dis*. 2012;1822(7):1114-1124. doi:10.1016/j.bbadis.2012.03.007

207. Baertling F, A.M. van den Brand M, Hertecant JL, et al. Mutations in COA6 cause cytochrome c oxidase deficiency and neonatal hypertrophic cardiomyopathy. *Hum Mutat*. 2015;36(1):34-38. doi:10.1002/humu.22715

208. Baertling F, Al-Murshedi F, Sánchez-Caballero L, et al. Mutation in mitochondrial complex IV subunit COX5A causes pulmonary arterial hypertension, lactic acidemia, and failure to thrive. *Hum Mutat*. 2017;38(6):692-703. doi:10.1002/humu.23210

209. Schäfer E, Seelert H, Reifschneider NH, Krause F, Dencher NA, Vonck J. Architecture of active mammalian respiratory chain supercomplexes. *J Biol Chem*. 2006;281(22):15370-15375. doi:10.1074/JBC.M513525200

210. Fessler E, Eckl EM, Schmitt S, et al. A pathway coordinated by DELE1 relays mitochondrial stress to the cytosol. *Nature*. 2020;579(7799):433-437. doi:10.1038/s41586-020-2076-4

211. Palam LR, Baird TD, Wek RC. Phosphorylation of eIF2 facilitates ribosomal bypass of an inhibitory upstream ORF to enhance CHOP translation. *J Biol Chem*. 2011;286(13):10939-10949. doi:10.1074/jbc.M110.216093

212. Strauss M, Hofhaus G, Schröder RR, Kühlbrandt W. Dimer ribbons of ATP synthase shape the inner mitochondrial membrane. *EMBO J*. 2008;27(7):1154-1160. doi:10.1038/EMBOJ.2008.35

213. Wiedemann N, Van Der Laan M, Hutu DP, Rehling P, Pfanner N. Sorting switch of mitochondrial presequence translocase involves coupling of motor module to respiratory chain. *J Cell Biol*. 2007;179(6):1115-1122. doi:10.1083/JCB.200709087

214. Pfanner N, Warscheid B, Wiedemann N. Mitochondrial proteins: from biogenesis to functional networks. *Nat Rev Mol Cell Biol*. 2019;20(5):267-284. doi:10.1038/s41580-018-0092-0

215. Hashimoto T, Hussien R, Cho HS, Kaufer D, Brooks GA. Evidence for the mitochondrial lactate oxidation complex in rat neurons: Demonstration of an essential component of brain lactate shuttles. *PLoS One*. 2008;3(8). doi:10.1371/journal.pone.0002915

216. Du X, Carvalho-De-Souza JL, Wei C, et al. Loss-of-function BK channel mutation causes impaired mitochondria and progressive cerebellar ataxia. *Proc Natl Acad Sci U S A*. 2020;117(11):6023-6034. doi:10.1073/pnas.1920008117

217. Hou S, Xu R, Heinemann SH, Hoshi T. The RCK1 high-affinity Ca2+ sensor confers carbon monoxide sensitivity to Slo1 BK channels. *Proc Natl Acad Sci U S A*. 2008;105(10):4039-4043. doi:10.1073/pnas.0800304105

218. Williams SE, Brazier SP, Baban N, et al. A structural motif in the C-terminal tail of slo1 confers carbon monoxide sensitivity to human BKCa channels. *Pflugers Arch Eur J Physiol*. 2008;456(3):561-572. doi:10.1007/s00424-007-0439-4

219. Wilson JL, Wareham LK, McLean S, et al. CO-Releasing Molecules Have Nonheme Targets in Bacteria: Transcriptomic, Mathematical Modeling and Biochemical Analyses of CORM-3 [Ru(CO)3Cl(glycinate)] Actions on a Heme-Deficient Mutant of Escherichia coli. *Antioxidants Redox Signal*. 2015;23(2):148-162. doi:10.1089/ars.2014.6151

220. Ling K, Men F, Wang WC, Zhou YQ, Zhang HW, Ye DW. Carbon Monoxide and Its Controlled Release: Therapeutic Application, Detection, and Development of Carbon Monoxide Releasing Molecules (CORMs). *J Med Chem*. 2018;61(7):2611-2635. doi:10.1021/ACS.JMEDCHEM.6B01153

221. Mann BE. CO-releasing molecules: A personal view. *Organometallics*. 2012;31(16):5728-5735. doi:10.1021/OM300364A/

222. Dallas ML, Boyle JP, Milligan CJ, et al. Carbon monoxide protects against oxidant-induced apoptosis via inhibition of Kv2.1. *FASEB J*. 2011;25(5):1519-1530. doi:10.1096/FJ.10-173450

223. Crook SH, Mann BE, Meijer AJHM, et al. [Mn(CO)4{S2CNMe(CH2CO2H)}], a new water-soluble CO-releasing molecule. *Dalt Trans*. 2011;40(16):4230-4235. doi:10.1039/c1dt10125k

224. Motterlini R, Foresti R. Biological signaling by carbon monoxide and carbon monoxide-releasing molecules. *Am J Physiol - Cell Physiol*. 2017;312(3):C302-C313. doi:10.1152/ajpcell.00360.2016

225. Hayashi Y, Morinaga S, Zhang J, et al. BK channels in microglia are required for morphine-induced hyperalgesia. *Nat Commun*. 2016;7. doi:10.1038/NCOMMS11697

226. Babu D, Leclercq G, Goossens V, et al. Antioxidant potential of CORM-A1 and resveratrol during TNF-α/cycloheximide-induced oxidative stress and apoptosis in murine intestinal epithelial MODE-K cells. *Toxicol Appl Pharmacol*. 2015;288(2):161-178. doi:10.1016/J.TAAP.2015.07.007

227. Babu D, Leclercq G, Motterlini R, Lefebvre RA. Differential effects of CORM-2 and CORM-401 in murine intestinal epithelial MODE-K cells under oxidative stress. *Front*

Pharmacol. 2017;8(FEB):1-17. doi:10.3389/fphar.2017.00031

228. Gallio AE, Fung SS-P, Cammack-Najera A, Hudson AJ, Raven EL. Understanding the Logistics for the Distribution of Heme in Cells. *JACS Au*. 2021;1(10):1541-1555. doi:10.1021/JACSAU.1C00288

229. Mavridou DAI, Ferguson SJ, Stevens JM. Cytochrome c assembly. *IUBMB Life*. 2013;65(3):209-216. doi:10.1002/IUB.1123

230. Kapetanaki SM, Burton MJ, Basran J, et al. A mechanism for CO regulation of ion channels. *Nat Commun*. 2018;9(1). doi:10.1038/s41467-018-03291-z

231. Yi L, Morgan JT, Ragsdale SW. Identification of a thiol/disulfide redox switch in the human BK channel that controls its affinity for heme and CO. *J Biol Chem*. 2010;285(26):20117-20127. doi:10.1074/jbc.M110.116483

232. Gozzelino R, Jeney V, Soares MP. Mechanisms of cell protection by heme oxygenase-1. *Annu Rev Pharmacol Toxicol*. 2010;50:323-354. doi:10.1146/ANNUREV.PHARMTOX.010909.105600

233. Williams SEJ, Wootton P, Mason HS, et al. Hemoxygenase-2 is an oxygen sensor for a calcium-sensitive potassium channel. *Science*. 2004;306(5704):2093-2097. doi:10.1126/SCIENCE.1105010

234. Bindu S, Pal C, Dey S, et al. Translocation of heme oxygenase-1 to mitochondria is a novel cytoprotective mechanism against non-steroidal anti-inflammatory drug-induced mitochondrial oxidative stress, apoptosis, and gastric mucosal injury. *J Biol Chem*. 2011;286(45):39387-39402. doi:10.1074/jbc.M111.279893

235. Ma X, Sayed N, Beuve A, Van Den Akker F. NO and CO differentially activate soluble guanylyl cyclase via a heme pivot-bend mechanism. *EMBO J*. 2007;26(2):578. doi:10.1038/SJ.EMBOJ.7601521